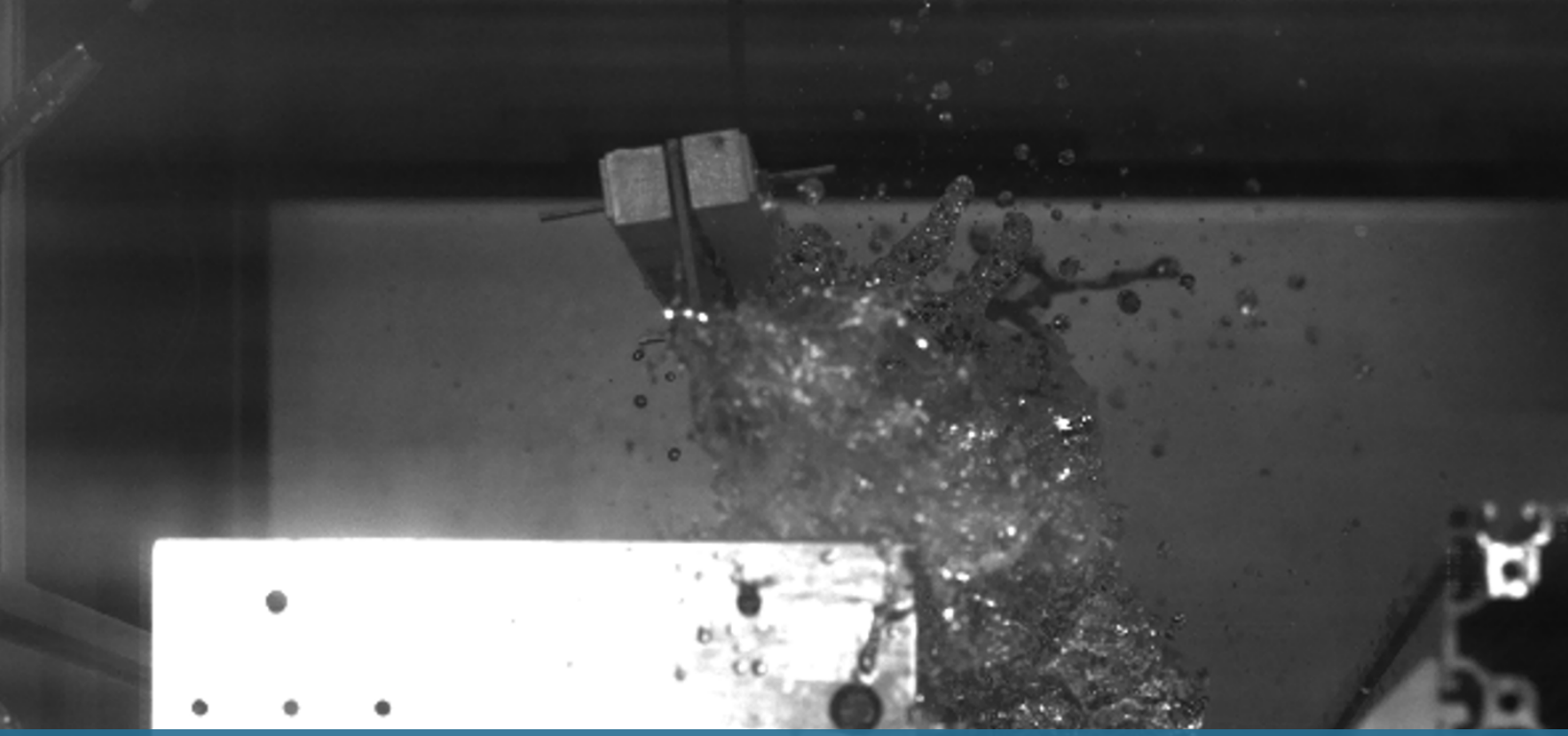

The effect of non-uniformity on the hydroelasticity of OWTs

Experimental study on the effect of added mass and end mass

Stefan Neele

TU Delft

mocean
ADVANCED OFFSHORE TECHNOLOGY

The effect of non-uniformity on the hydroelasticity of OWTs

Experimental study on the effect of added mass and end mass on hydroelasticity.

Stefan Neele

Master thesis to obtain MSc degree in Offshore & Dredging Engineering

Author
S.P. Neele - 5094720

Supervisors:
Dr. Ir. P.R. Wellens
Dr. Ir. E. Rongé

MSc Offshore and Dredging Engineering
Delft University of Technology
May 10, 2025

Abstract

Improved modeling of the response of offshore wind turbines (OWTs) is key to optimizing design and reducing maintenance costs and downtime. A major challenge is the modeling of hydroelasticity, which is not yet well understood for non-uniform structures such as OWTs. Previous research on hydroelasticity during impact events focused on uniform systems, and the effect of non-uniformities on hydroelasticity has not been properly studied yet. Two characteristic non-uniformities of OWTs are the end mass (from the rotor-nacelle assembly) and the added mass around the base of the structure resulting from its submersion depth. The main research question in this thesis was:
What is the effect of end mass and added mass on the hydroelasticity of non-uniform systems, such as offshore wind turbines, under breaking wave impact?

This question was answered through an experimental campaign. Experiments were conducted using a two-dimensional OWT model with varying end masses and submersion depths, which was impacted by a focused breaking wave in the wave tank at the Ship Hydromechanics lab of TU Delft. The force and structural response were measured and compared against a non-hydroelastic rigid model. Computational fluid dynamics simulations were performed using ComFlow, and a Finite Element Method model was created to get a quasi-static estimate of the model response used for comparison.

By increasing the end mass and added mass, the first natural period of the models approached the loading duration of the impact. This resulted in a peak force reduction of up to 30% compared to rigid models, indicating that the role of hydroelasticity increases as this ratio approaches 1.0. However, an effect on peak force reduction due to submersion depth for structures with similar period ratios was also seen, indicating the complexity of hydroelasticity for non-uniform structures. Comparing the structural response in the experiments against the quasi-static estimate showed larger errors for models with a period ratio close to 1.0, underestimating the response by up to 27% for the maximum deflection and 75% for the maximum acceleration. The results in this thesis show that the characteristic non-uniformities of offshore wind turbines significantly influence the hydroelastic behavior of such structures during breaking wave impacts.

Preface

This thesis report is written to obtain the degree Master of Science in Offshore and Dredging Engineering at Delft University of Technology. I have spent the past 9 months on the work produced in this report and there are a few people I'd like to thank for their help during this period. Firstly, I want to thank Peter Wellens for being my supervisor. Your enthusiasm for the subject of hydroelasticity is contagious and I have enjoyed our meetings a lot. You never refrained from giving your honest opinion but you also encouraged me to try to change your mind when I thought there was a good alternative. You have motivated me to be critical of my work and this has contributed a lot to the success of the project. Next, I want to thank Elie Rongé, who was my supervisor at Mocean Offshore. Thank you for always making time to answer my questions and providing me with really helpful insights. Your experience with CFD and experiments was extremely valuable for me. I'd also like the rest of the Mocean team for all the fun I've had during the past months, I think it was a unique graduation experience that I have enjoyed a lot! I also want to thank everyone at the Ship Hydromechanics lab for your assistance during my experimental campaign. I could not have done the experiment without your expertise and help. Finally, I'd like to thank my family and my girlfriend Evie for your never ending support and interest in what I was working on.

Stefan Neele,
Delft, May 10, 2025

Contents

List of Figures

List of Tables

1 Background

The most common foundation used for the installation of offshore wind turbines (OWT) is the monopile (MP), currently used for more than 60% of all OWTs. Even when accounting for the already announced future (floating) projects, the monopile remains the most common foundation in the foreseeable future [1]. Monopile foundations are usually installed in water depths up to 40 meters [2] although research is being done to extend this depth to 60 meters. Maintenance costs contribute to more than 20% of the Levelized Cost of Energy (LCoE) for a bottom-fixed OWT [3].

Without accurate modeling the forces on an OWT can be underestimated which can lead to unexpected failure due to maximum loads. Additionally, wrong computation of OWT response can lead to an wrong calculations on the lifetime of OWTs by underestimating the fatigue that will occur. These unexpected failures will lead to increased maintenance costs which will increase the LCoE for offshore wind. Therefore, accurate computation of loading and response is important to reduce the LCoE of offshore wind by reducing unforeseen failure and maintenance.

One of the challenges in the modeling of loading and response is hydroelasticity. In hydroelastic events, for example breaking wave impacts, the response of a structure influences the loading on the structure. The computation of the load and response is therefore a strongly coupled problem. For these situations, conventional quasi-static approaches are often not sufficient for accurate estimates [4]. This section will provide an overview of the state-of-the-art of hydroelastic modelling and introduce the knowledge gaps this thesis will contribute to.

1.1 Breaking wave impact

Monopile based OWTs are located in shallow water regions. As a wave enters shallow water it will start to transform until it reaches a critical height, starts to overturn and eventually breaks [5]. When a breaking wave meets an offshore structure this can lead to a breaking wave impact, also called slamming. The force exerted on a structure by a breaking wave depends on the breaking location relative to that structure. Wienke and Oumeraci concluded that the force is largest when the wave breaks just in front of the cylinder [6]. Bos and Wellens [7] concluded from pendulum tests that the force was largest for the wave breaking furthest away from the cylinder. The force also depends on the type of breaking wave that hits the structure. Hofland et al. [8] concluded that flip-through impact creates the largest force but noted that this event is rare in reality. According to Tu et al. [9] the plunging breaking wave is the most relevant for slamming as it features a small dissipating area, local high pressure and high impulsive load. According to Wienke and Oumeraci [6] plunging breakers can cause large impact forces on a slender structure.

Slamming on monopiles has been studied experimentally using scale models in wave tanks. Paulsen et al. [10] showed through large scale experiments on monopile foundations that the slamming forces from breaking waves represent a significant part of the extreme loading and is therefore relevant for the Ultimate Limit State of monopile based OWTs. With increasing diameters the slamming load will become even more important as the loading scales with the square of the diameter [10]. Wienke and Oumeraci [6] looked at the influence of impact angle (angle between wave crest and vertical front of monopile) and found that a negative angle yielded the largest force. de Ridder et al. [11] did wave impact studies with a flexible tower and reported large horizontal accelerations at RNA height as a result of breaking wave impacts.

Other studies have focused on Computational Fluid Dynamics (CFD) to study wave impacts on monopile structures. Wang et al. [12] computed slam loads on a truncated vertical cylinder while also studying run-up effects. It was concluded that the non-linearity of the problem increases with an increase in wave amplitude. Aggarwal et al. [13] validated a numerical model for wave impact using earlier experiments. The model was used to study the effect of wave breaking type on the loads of the structure. It was found that with an increase in spectral steepness there was an increase in the occurrence of plunging breaking waves, as well as an increase in wave force.

Some studies have focused on developing (semi-)analytical models to quantify the slamming loads on monopile OWTs, focusing on cylindrical structures. Studies on semi-analytical models have been performed by [6], [10], [14], [15] and [16]. These studies have not converged to an accurate analytical formulation. Lackner et al. [17] compared several of these models to CFD results and concluded that these models do not capture the time history well after impact, possibly due to neglecting run-up effects. For plates, two often used analytical methods to quantify wave impact pressures are the theories by Wagner [16] and Von Kármán [18].

1.2 Hydroelasticity in wave impact events

1.2.1 Hydroelasticity

A common approach to compute the response of offshore structures is a one-way coupled method. This method first computes a load based on the properties of an incoming wave under the assumption that the structure is rigid. This load is then used in a deformation model of the structure to compute the response. For certain situations this method is not accurate, such as cases in which hydroelasticity is relevant [4].

Hydroelasticity deals with the two-way coupling between fluid loading and structure response. This coupling happens in two ways. Firstly, the fluid exerts a pressure on the structure which can cause deformation on the structure. As a consequence of this deformation the loading from the fluid on the structure changes as this depends on the shape and orientation of the surface on which the fluid acts. Secondly, an excitation close to the natural frequency of a structure can cause vibrations in the structure which also affects the hydrodynamic loading of the structure [19]. Temarel [20] discusses the importance of accounting for hydroelasticity in slamming events.

Hydroelastic effects affect the magnitude of computed loads on structures. Bereznitski [4] did numerical impact tests with free falling beams and concluded that ignoring hydroelasticity increases computed deflections. Mai et al. [21] did experiments with free-falling plates (called slamming in this study) with varying flexibility as well as wave impacts on rigid and flexible walls (called wave impacts in this study). It was concluded that for slamming events with high impact velocity, the elasticity of the structure can lead to significant decrease in impact loads. The study reported that on flexible plates the total impact force decreased. Horn et al. [22] studied the contribution of hydroelastic effects on the fatigue life of structures. It was found that ringing responses increased fatigue damage.

1.2.2 Relevance for OWTs

Multiple studies have shown that hydroelastic effects are also relevant for monopile structures. Sagar et al. [23] combined a Reynolds-averaged Navier-Stokes (RANS) with a Finite Element Model (FEM). It was found that the second eigenfrequency of monopile foundations structures can increase dynamic loads. This effects get more pronounced for larger foundation designs as the eigenfrequency is getting

smaller. Thome et al. [24] concluded that in regular and irregular waves the loads computed when accounting for hydroelasticity were larger then when neglecting hydroelasticity. Ti et al. [25] used a BEM method together with an Euler-Bernoulli beam theory to study the wet dynamic characteristics of a bottom-mounted structure.

1.3 Structural response of (non-)uniform systems

1.3.1 Response of uniform systems

Each structure has its own natural frequencies. The natural frequencies represent the frequencies at which a structure will oscillate when released from a position other than its equilibrium position without any external forces acting on it [26]. For an undamped simple mass-spring system with stiffness k and mass m the first (fundamental) natural frequency f_1 in Hertz is given by:

$$f_1 = \frac{1}{2\pi}\sqrt{\frac{k}{m}} \tag{1.1}$$

Hydroelastic research often focuses on uniform two-dimensional (clamped) plates. When such a structure is loaded over the full width (two-dimensional loading) the system can be represented as a uniform clamped beam. A uniform beam that is clamped on one side and free at the other side is known as a cantilever beam. For a cantilever beam the first four natural frequencies can be computed using: [26].

$$f_i = \frac{\lambda_i^2}{2\pi L^2}\sqrt{\frac{EI}{\rho A}} \qquad \lambda_1, \lambda_2, \lambda_3, \lambda_4 = 1.875, 4.694, 7.855, 10.996 \tag{1.2}$$

This natural frequency thus depends on the E-modulus (E), second moment of area (I), length (L), density (ρ) and area (A). For a plate with thickness t, width W and length L, the second moment of area is:

$$I = \frac{W \cdot t^3}{12} \qquad A = W \cdot t$$

Equation 1.2 has a form similar to Equation 1.1. The terms in the numerator of the square root represent the stiffness (EI) and the terms in the denominator represent the mass per unit length (ρA).

The response of the structure at is natural frequencies is known as its mode shape or eigenmode. Each natural frequency has its own mode shape. The first four mode shapes of a simple uniform cantilever beam are shown in Figure 1.1. For a cantilever beam these mode shapes can be described by Equation 1.3 [26]. Here, $w(x)$ is the deflection along the length of the beam (x).

$$w_i(x) = cosh\Big(\frac{\lambda_i x}{L}\Big) - cos\Big(\frac{\lambda_i x}{L}\Big) - \sigma_i\Big(sinh\Big(\frac{\lambda_i x}{L}\Big) - sin\Big(\frac{\lambda_i x}{L}\Big)\Big) \qquad \sigma_i = 0.734, 1.018, 0.999, 1.000 \tag{1.3}$$

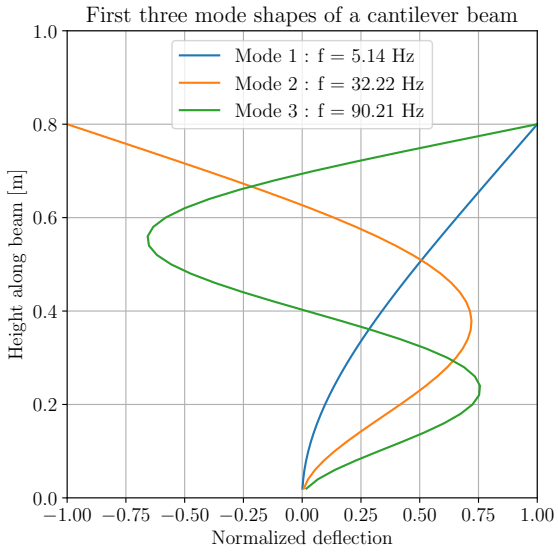

Fig. 1.1 *The first three mode shapes of a uniform cantilever beam.*

When deflections and curvatures are small, modal analysis can be applied. The idea behind modal analysis is that the response of a structure to an excitation can be computed by superposition of each mode shape multiplied with a factor indicating its contribution (modal amplitude, $q_i(x)$): [27]

$$w(x) = \sum_{i=1}^{\infty} q_i(x) \cdot w_i(x) \tag{1.4}$$

In practice, not all modes are necessary to get an accurate enough approximation of the response since the modes further away from the excitation frequency tend to have relatively small modal amplitudes.

The response of a structure to an excitation thus depends on which natural frequencies are excited and on which mode shapes correspond to these excited natural frequencies.

1.3.2 Response of non-uniform systems

To represent an offshore wind turbine two-dimensionally, two changes are made to the simple cantilever beam. First, a large end-mass is added. This represent the rotor-nacelle assembly (RNA), and is seen schematically in Figure 1.2a. The first natural frequency of such a system can be approximated using: [26]

$$f_1 = \frac{1}{2\pi}\sqrt{\frac{3EI}{L^3(M_{top} + 0.24M_{beam})}} \tag{1.5}$$

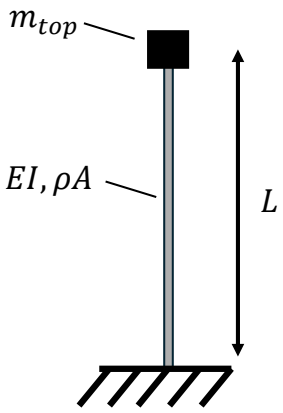

(a) *Cantilever plate with end mass.*

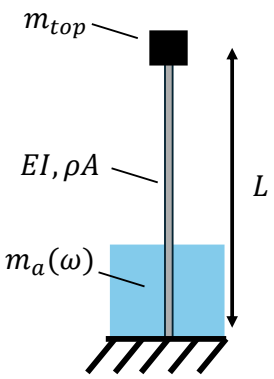

(b) *The OWT as modeled in this thesis: a uniform clamped plate with an end mass and added mass around the base.*

Fig. 1.2 *Changes made to uniform beam model to match OWT characteristics.*

The second addition is the added mass as a result of part of the structure being submerged. Taking the added mass as dependent on (rotational) frequency (ω), the system can be represented as in Figure 1.2b. Having structural properties that are dependent on the motion of the structure increases the complexity of solving for the natural frequencies and mode shapes. Computing the natural frequencies and mode shapes for a structure like this is best done numerically, for example using a Finite Element Model (FEM). How this is done will be explained in Section 5 in which the FEM used in this thesis is explained. In Figure 1.3 the first three mode shapes for two example configurations can be seen. In this figure d represents the submersion depth (added mass).

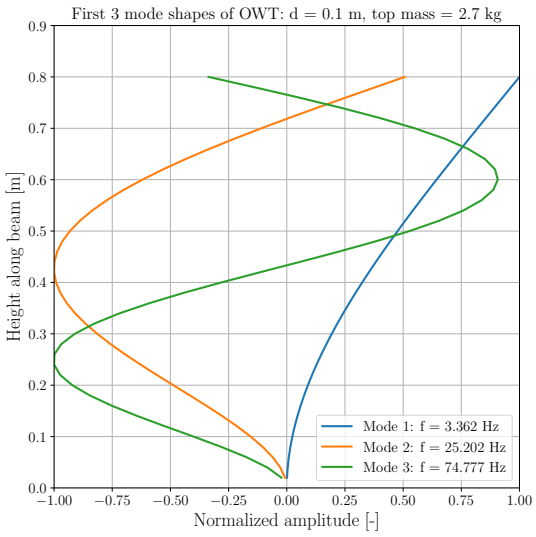

(a)

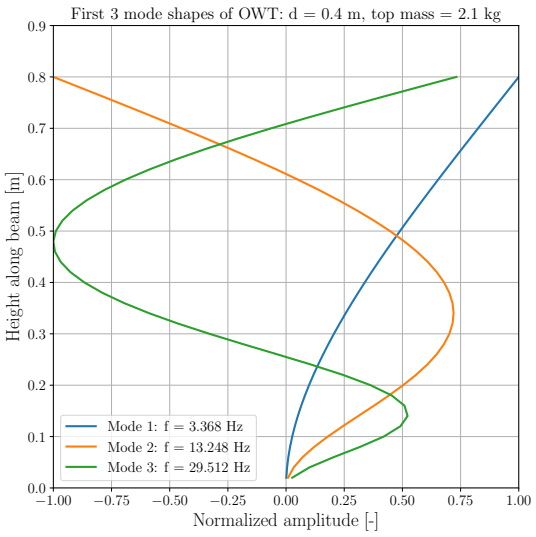

(b)

Fig. 1.3 *Two example configurations with different submersion depths and different end masses. All amplitudes are scaled to have the maximum amplitude at 1.0.*

As seen in Figure 1.3, both structures have the same first natural frequency, but different higher or-

der frequencies and different mode shapes (for example mode shape 2 (red line)). Since the structural response depends on the natural frequencies and mode shapes, these effects could be important for hydroelasticity in non-uniform systems. The next section will explain how the structural response affects hydroelasticity and what the main difference between uniform and non-uniform structures is in the context of hydroelasticity.

1.4 Effect of structural response on hydroelasticity

1.4.1 Hydroelasticity of uniform systems

Hydroelasticity has been studied extensively on a fundamental level. Most fundamental studies are focused on quantifying the importance of hydroelastic effects with respect to structural properties. These studies are often performed on uniform plates or beams. Faltinsen [28] studied the importance of hydroelasticity for a ship hull. The importance was expressed as a function of the ratio between the non-dimensional wetting time of the plate and the non-dimensional first natural period of the plate. It is concluded that when this ratio is small hydroelasticity is important. Bereznitski [4] did a numerical study on uniform beams and expressed the importance as a function of the ratio between the slamming duration and the first structural period of a beam. In this study it was concluded that when this ratio is larger than 2, hydroelasticity is no longer relevant. Stenius et al. [29], Kaminski et al. [30] and Bos et al. [31] all found a similar ratio and trend in their studies. Two of these ratios are shown in Figure 1.4. All studies show that a small ratio of loading time over first natural period leads to larger hydroelastic effects. Allen and Battley [32] points out the limited validation done on these ratios.

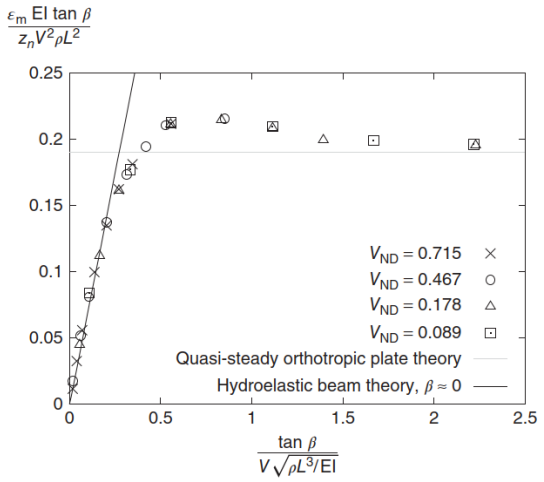

(a) *Faltinsen [28], figure from Faltinsen [33]. The x-axis shows the ratio between wetting time of of a rigid wedge and natural period of a stiffener beam. The y-axis is dimensionless strain.*

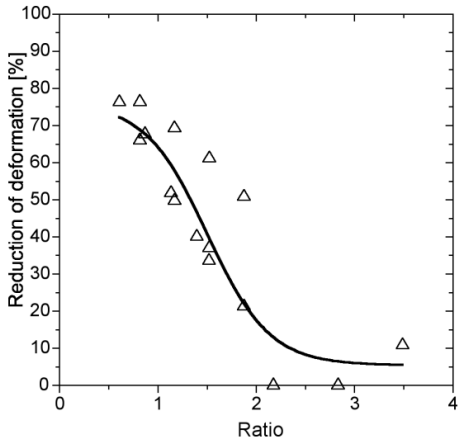

(b) *Bereznitski [4].The ratio on the x-axis is the duration of the impact over the first natural period of the structure.*

Fig. 1.4 *Results from studies using the first natural frequency or period as a way to quantify the importance of hydroelasticity of uniform plates.*

For uniform cantilever plates, the mode shapes corresponding to e.g. the first mode shape are always the same. This means that when comparing different structures like this, for example plates of varying thickness, the difference in response is caused just by the modal amplitude. In other words, only the relation between natural frequencies and the excitation frequency influences how the compared

structures respond. This means that using the (first) natural frequencies to determine the influence of hydroelasticity is sufficient. This does not apply to non-uniform structures however, as will be illustrated in the next section.

1.4.2 Hydroelasticity of non-uniform systems

As shown in Section 1.3.2, for the non-uniform model of an OWT the natural frequencies and the mode shapes depend on the submersion depth (added mass) and end mass. This means there can be multiple systems with the same first natural frequency but different mode shapes (as seen in Figure 1.3) at its respective natural frequencies. As a result, these structures will respond differently when excited at the same frequency. Since hydroelasticity is dependent on how a structure responds under loading, this means that the structures will have a different hydroelastic response.

This effect is reinforced by the fact that the higher order frequencies are also different, as also seen in Figure 1.3. Multiple studies have shown that the second structural mode also affects hydroelastic response. Bunnik et al. [34] made a one-way coupled model to analyze structural response to breaking waves. They found that first and second mode dominate the response. When the wave breaks closer to the monopile, the second mode dominates more. de Ridder et al. [35] concludes that the first and second mode dominate the dynamic response of a monopile OWT exposed to wave impacts. Suja-Thauvin et al. [36] concludes that the second mode is triggered and can contribute to up to 20% of total response.

To conclude, the research done on uniform systems so far does not capture all relevant physics that influence hydroelasticity on non-uniform structures such as OWTs. As a result, a knowledge gap exists on the influence of structural configuration of more complex system on hydroelasticity.

1.5 Modeling of hydroelasticity

As seen in the previous sections, for hydroelastic situations the structural response and loading are strongly coupled. This requires models that can compute the loading and response simultaneously, while including this coupling in the computation. Due to the highly non-linear physics involved in hydroelastic wave impact events, many studies have used high-fidelity models to study the physics of hydroelasticity. Korobkin et al. [37] worked on a numerical model for hydroelastic impact of a wedge using a coupled model. Two modelling methods are discussed in the paper. Xie et al. [38] constructed a fully-coupled CFD-FEM model for hydroelastic impacts. It was concluded that more than one mode shape dominates structural deformation. This phenomena was also found by [39] in a study on hydroelastic water-entry problems using a fully coupled Smoothed Particle Hydrodynamics (SPH) and FEM model.

Some Reduced-Order Models (ROM) for hydroelasticity on simple structures have been created. Faltinsen et al. [40] created a hydroelastic beam model to study wetdeck slamming. Bos and Wellens [7] created a ROM for a simple pendulum exposed to breaking waves. This model could predict the response of this simple 1DOF system quite well. Later, Bos et al. [31] constructed a ROM for hydroelastic behaviour of the wall of an LNG tank. This model was able to accurately predict the added mass and total impulse but underpredicts the force.

2 Research question

2.1 Knowledge gaps

As shown in Section 1.4.1, current research focuses on uniform plates and does not capture all relevant characteristics of structural response for non-uniform systems due to the differences in higher mode responses. As a result, only considering the first natural frequency could be an incomplete description of the importance of hydroelasticity. Currently, there is no clear indication in literature on how the importance of hydroelasticity for a non-uniform system (such as a 2D representation of an OWT as a cantilever plate with end-mass) can be quantified. This thesis will contribute to closing this knowledge gap by investigating the hydroelasticity of non-uniform OWT models by varying the added mass and end mass.

As shown in the studies in Section 1.2.2, accounting for hydroelasticity is important in monopile-based OWT design. Accounting for hydroelasticity will lead to more accurate methods to compute loads, responses and fatigue life. This can lead to improved designs which will help reduce the LCoE of offshore wind. Hydroelasticity is often expressed in terms of forces, but it is possible that the conclusions are different when expressing hydroelasticity in terms of response. This thesis will therefore also investigate the difference between the responses computed by a one-way coupled model and the actual hydroelastic response in the experiment. The insights from this comparison can contribute to solving the challenges related to modeling the hydroelastic response of non-uniform structures such as OWTs.

2.2 Research question

The main goal of this thesis is contributing to closing the knowledge gaps identified in Section 2.1. The main research question is as follows: ***What is the effect of added mass and end-mass on the hydroelastic behaviour of non-uniform systems, such as Offshore Wind Turbines, under breaking wave impact?*** In order to answer this question several subquestions have been identified:

RQ 1: What is the effect of the end-mass on hydroelasticity?

RQ 2: What is the effect of added mass on hydroelasticity?

RQ 3: How do the first and higher natural frequencies of non-uniform systems influence hydroelasticity?

RQ 4: How does the response in a hydroelastic impact event differ from the response computed using a one-way coupled model?

3 Analysed system and approach

3.1 Approach

To answer the research question an experiment was conducted on a simplified model of an offshore wind turbine (OWT). This experiment has been set up using estimates provided by Computational Fluid Dynamics (CFD) simulations performed using ComFlow (Section 4) in combination with estimates from a self-made Finite Element Method (FEM) model (Section 5). These estimates lead to an experiment that is explained in Section 6.

3.2 Analysed system

Normally, a bottom-fixed monopile-based offshore wind turbine stands on a steel foundation, the monopile (MP), which is embedded in the seafloor. A transition piece (TP) is placed on top of this monopile, which serves as a connection between the MP and the turbine tower. This means that vertically speaking the structure consists of three separate structures, all with different characteristics in terms of size and materials and therefore different stiffness and mass distributions. The structure in this thesis is greatly simplified by taking the monopile, transition piece and turbine tower as one structure. Additionally, this structure is assumed to be homogeneously shaped from top to bottom, instead of changing in size along the height (such as the tapered turbine tower or the complex shape of the TP in an actual OWT).

The next important assumption is that the system is modeled as being two-dimensional instead of three-dimensional. This means the structure is considered to be a beam instead of a 3D cylinder. Since zero width is impossible in an experiment, the model is taken as being wide instead. A structure with large width is less affected by the boundary conditions on the side edges, and therefore approaches the behavior of a 2D structure. By being much wider than thick and loading it symmetrically in this direction, a (close to) two-dimensional representation is achieved.

There are three main reasons for making the structure two-dimensional. The first and most important reason is that almost all studies previously done on hydroelastic wave impacts were performed on two-dimensional plates or beams (as shown in Section 1). To make relevant comparisons with these studies, it is useful to study a structure that is still comparable to the ones analyzed there. Secondly, any numerical computation (such as CFD or FEM) is much faster in two dimensions than in three since fewer degrees of freedom need to be solved. Lastly, three-dimensional effects are much harder to account for than two-dimensional effects. Keeping the structure 2D reduces complexity and therefore simplifies modeling. Combining all these simplifications results in a representation of the OWT as shown in Figure 3.1.

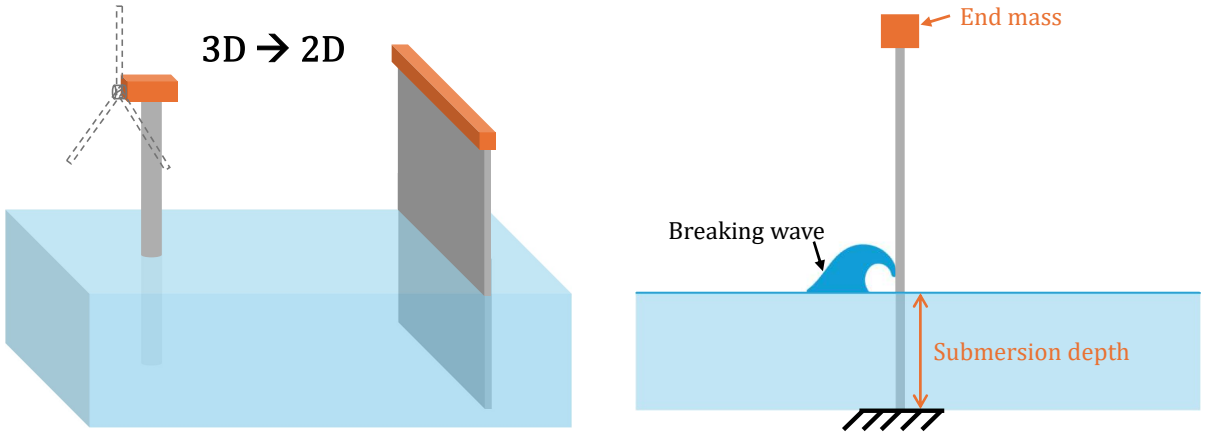

(a) *Visualization of transforming 3D reality to 2D representation in thesis.*

(b) *Schematic of experiment. Variations are done on orange parts.*

Fig. 3.1 *Two-dimensional representation OWTs during the experiment.*

During the experiment variations with the end-mass and with the submersion depth (added mass) will be performed. The end mass will be selected from a range of end mass to plate mass between 0 and 1.5 and the submersion depth will be varied between 0.125 and 0.5 of the plate length. This is discussed in more detail in the section on the experimental methodology (Section 6). This submersion depth might slightly affect the loading too, but it was assumed that this effect will be small compared to the slamming load.

4 Computational Fluid Dynamics Simulations

The planned experiment was numerically simulated using ComFlow, which is a type of computational fluid dynamics (CFD) software. The purpose of these simulations was to determine an appropriate breaking wave profile and obtain the corresponding loading condition for the experiment and to produce input signals in terms of distributed force for the finite element method (FEM) model (Section 5). This section will introduce the concept of CFD, explain how the numerical simulations were set up and discuss limitations of the performed simulations. Lastly, it will present the results that are used as input in the FEM model.

4.1 Computational Fluid Dynamics

CFD software is used to numerically solve the Navier-Stokes (NS) equations for a fluid problem. A program called ComFlow is used, which was developed by MARIN, TU Delft and Rijksuniversiteit Groningen. ComFlow is specifically designed to efficiently simulate violent free-surface flows, such as the expected flow in the breaking wave impacts [41]. ComFlow solves the Navier-Stokes equations using a solver with a Volume-of-Fluid (VOF) based free-surface displacement. This method is briefly explained below, this explanation is based on [42] and [43].

The Navier-Stokes equations describe fluid motion in a given domain. The situation in the experiment is a one-phase flow. The water is assumed to be a homogeneous, incompressible and viscous fluid. The NS equations can be simplified to the conservation of mass equation and the conservation of momentum equation:

$$\frac{\partial \rho}{\partial t} + \nabla(\rho \vec{u}) = 0 \tag{4.1}$$

$$\frac{\partial(\rho \vec{u})}{\partial t} + \nabla \cdot (\rho \vec{u}\vec{u}) = -\nabla p + \nabla \cdot (\mu \nabla \vec{u}) + \vec{F} = 0 \tag{4.2}$$

In these equations $\vec{u}$ is the velocity vector with the velocities in all 3 directions (u, v, w), ρ is the density of the fluid, p is pressure, μ is dynamic viscosity and $\vec{F}$ are all the external forces acting on the fluid. The mass conservation equation states that for a closed domain (in this case the simulated domain) the mass must remain constant at all times, since no mass can be lost or generated.

At solid boundaries or the boundary of objects no fluid can go through the boundary. This is prescribed by $\vec{u} = 0$. For the liquid-gas interface ComFlow uses cell-weighted averaging. More details on this can be found in the ComFlow documentation [43].

In ComFlow the force on a structure consists only of the normal tension, since the shear force is neglected [43]. The force on the object surface (called S here) is therefore calculated as the integrated pressure over the boundary of the object. This is given by:

$$\vec{F}_p = \int_S p\, \vec{n}\, dS \tag{4.3}$$

This equation is used to compute the pressure and force on the model as a result of the breaking wave impact.

Discretization of the NS equations is done in time and space. The time discretization is done using the Adams-Bashforth (AB) method, which is second-order accurate. Spatial discretization is done using a

finite volume method. The time steps are adjusted using the CFL-condition, which is given by:

$$CFL = \frac{|u|\Delta t}{\Delta x} \leq 0.25 \tag{4.4}$$

This condition will make sure that when the velocities increase, the timestep will decrease. Additionally, for smaller cell sizes (finer grid) a smaller timestep is required. The following sections will discuss how the simulations performed in this thesis were set up.

4.2 ComFlow simulations used for experimental design

ComFlow simulations were performed to determine the expected outputs from the experiment. Especially important were the expected pressures (for pressure sensor selection and location) and forces (magnitude and frequency distribution). The simulations performed before the experiment are discussed in this section. During the experiment the wave was changed and some additional simulations were ran. These are explained in Sections 4.3 and 4.4.

4.2.1 Simulation domain, boundary conditions and discretization

The structure in the experiment will be loaded using a breaking wave. This wave is created using wave focusing which is explained in Section 4.2.3 and Appendix E. In the experiment the wave is generated 29.8 m away from the structure, with the focus point at 28.3 m (when taking the paddle at $x = 0$ m). Doing a CFD study of a propagating wave over this distance is too costly since this would require a significant amount of cells. Therefore, in the ComFlow study, only the last 7 meters of wave propagation is simulated. The experiment has been designed to be as two-dimensional as possible so the numerical study is performed in 2D. This gives a domain of 7 meters long, 1.25 m high (allowing for up to 0.5m of waveheight above the still water line) and 0 m wide. This can be seen in Figure 4.1.

Using a rectangular domain, 6 boundary conditions have to be defined, one for each end surface. The boundary condition at the interface with the structure is as explained in Section 4.1. Taking the x-direction as the wave propagation direction (travelling from $x = 0$ upwards) this requires an inlet boundary condition at $x = 0$ m and an outflow boundary condition at $x = 7$ m. At the inlet this is a Dirichlet boundary condition for the velocities and surface elevation, which are taken from an input generated from linear analytical components (Section 4.2.3). The outflow boundary condition is a generating and absorbing boundary condition, which is tuned following the ComFlow documentation to limit the amount of reflection at this boundary [43]. At the other boundaries a no-slip condition is used.

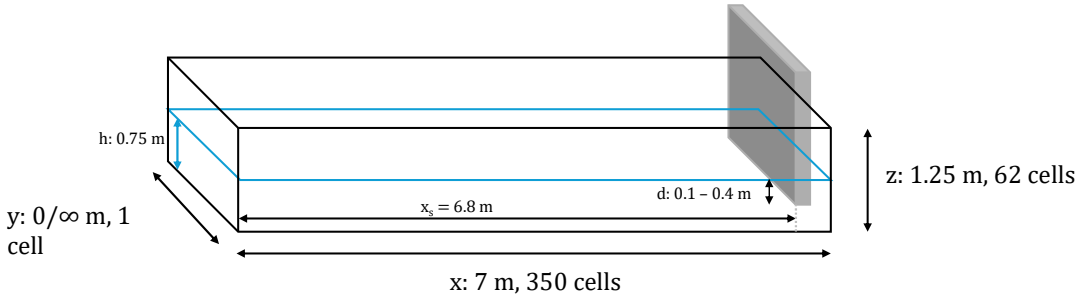

Fig. 4.1 *Domain used in the CFD simulations including dimensions. The position of the structure (grey block) is also shown.*

The CFD study is performed two-dimensionally. To achieve this, the domain is made 1 cell wide (in y-direction). The grid is divided into 350 cells in x-direction and 62 cells in z-direction. This means the cells have length of 0.02 m in both directions.

4.2.2 Geometry definition

The structure in the experiment is modeled as a rectangular structure filling the entire width of the domain (which is 1 cell wide due to the two-dimensional representation). In the experiment the submersion depth is varied between 0.1 and 0.4 m, so simulations were performed with the bottom of the structure at 0.1 to 0.4 m below the waterline. Since ComFlow does not work with deformable structures and there is no flow around the side of the structure, the influence of the thickness of the plate was assumed small. During these simulations the thickness was taken as 0.05 meters. The structure is placed at $x = 6.8$ m (x_s) and thus extends to $x = 6.85$ m. Placing the structure at this location was found to yield the largest impact force when the wave was focused at $x = 5$ m. The location of the structure is also shown in Figure 4.1.

4.2.3 Focused breaking wave

The concept of wave focusing is explained in more detail in Appendix E. In short: waves with longer wavelengths travel faster than waves with a shorter wavelength. The group speed (c_g) of a packet of waves is related to the wavenumber (k), angular frequency (ω) and waterdepth (h) according to:

$$c_g = \frac{\omega}{2k}\left(1 + \frac{2kh}{sinh(2kh)}\right) \tag{4.5}$$

By first generating shorter waves and then generating longer waves after a delay, the components can be "focused" to all be in phase at the same point in space and time and create a wave that is much larger than the maximum wave component the wavemaker could generate. Additionally, in this way it is possible to generate an unstable wave that breaks at a desired location. Table 4.1 shows the components used for the focused wave with which the simulations prior to the experiment were performed. The amplitude for each wave component in the experiment is limited by a certain steepness limit. This steepness can be expressed as H/λ, where H is the wave height, so twice the wave amplitude (A). For wave components with a steepness lower than 1/50 linear theory is a good approximation. Additionally, wave components with a steepness higher than 1/50 are generated with too much variability in the used tank due to nonlinear interactions. The same goes for wavelengths shorter than $\lambda = 1$ m. Wavelengths longer than $\lambda = 5$ m are limited in amplitude due to the stroke of the wave board [7]. All components in the focused wave thus have a wavelength between 1 to 5 meters and the steepest component has a steepness of 1/64.

Table 4.1 *Wave properties of the components used in the focused breaking wave.*

Component	1	2	3	4	5	6	7	8	9	10	11	12	13
λ [m]	1	1.1	1.2	1.3	1.4	1.7	1.8	2	2.5	3	3.5	4	5
Amplitude [m]	0.0125	0.0138	0.0150	0.0163	0.0175	0.0213	0.0225	0.0250	0.0313	0.0375	0.0438	0.0500	0.0625
k [1/m]	6.283	5.712	5.236	4.833	4.488	3.696	3.491	3.142	2.513	2.094	1.795	1.571	1.257
ω [rad/s]	7.850	7.484	7.164	6.881	6.627	5.998	5.821	5.502	4.852	4.341	3.921	3.570	3.013
T [s]	0.80	0.84	0.88	0.91	0.95	1.05	1.08	1.14	1.29	1.45	1.60	1.76	2.09

4.2.4 Simulation results used for design

The following results were used for the design of the experiment. The most important outputs of the ComFlow simulations are the resultant force over time, the corresponding frequency distribution and the pressure distributions on the structure over time. These were used for sensor and model selection for the experiment. The output of force and pressure for the four different submersion depths in the experiment are discussed in this section.

Force

The force output was used to obtain an estimate of the force during the experiment, which was used for the force sensor selection. The time series of the force on the structure can be seen in Figure 4.2. The first sinusoidal peaks are from the waves that are propagating ahead of the focused wave. These peaks are low enough in amplitude to not excite the structure, which will therefore remain close to its equilibrium position when the impact happens. The impact from the breaking wave can be seen in the peak at around $t = 11.7$ seconds. The force is larger for the deeper submersion tests, this is expected since a larger area of the plate is loaded. The single time step force spikes in the signal after the impact are common for ComFlow and can be seen in other studies as well [42]. Since the spikes mainly occur after the impact it is expected that the computed force values during the impact are not affected too much.

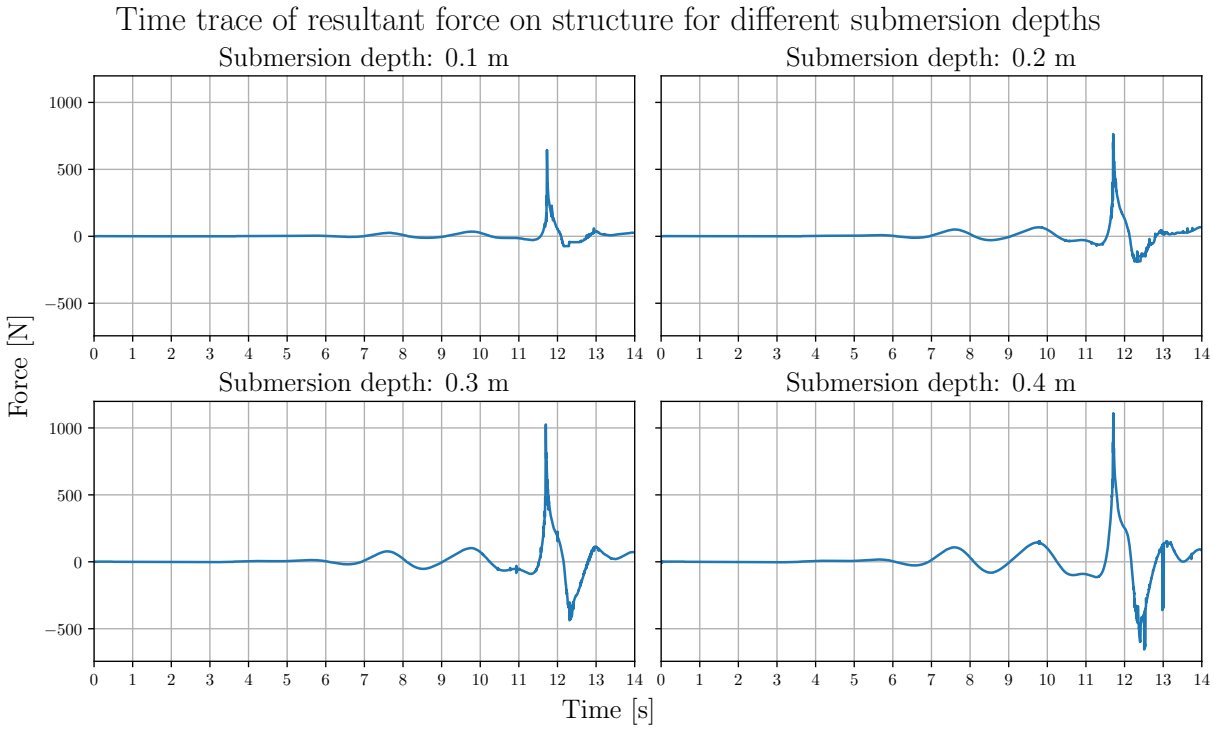

Fig. 4.2 *Time trace of the resultant force on the structure as a result of the breaking wave impact for the different submersion depths used during the experiment. The force resulting from the impact can be seen as the peak around $t = 11.7$ s.*

Since hydroelasticity depends on the match between first structural mode and loading duration, another relevant output from the simulations was the power spectrum of the force. The spectrum shows at which frequencies most power of the impact is located. A power spectrum from a simulated force can be seen in Figure 4.3a. As seen in the figure, the majority of the power is concentrated in frequencies

below 2.5 Hz. This information was used to determine the desired structural frequencies of the models used in the experiment as explained in Section 5.

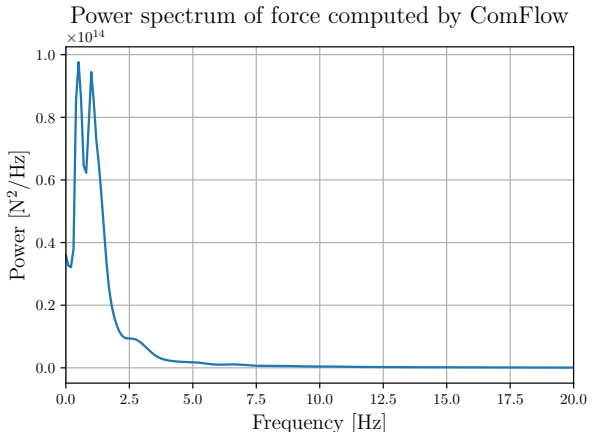

(a) *Power spectrum of force computed in ComFlow simulations. It can be seen that most energy is contained in frequency components below 2.5 Hz.*

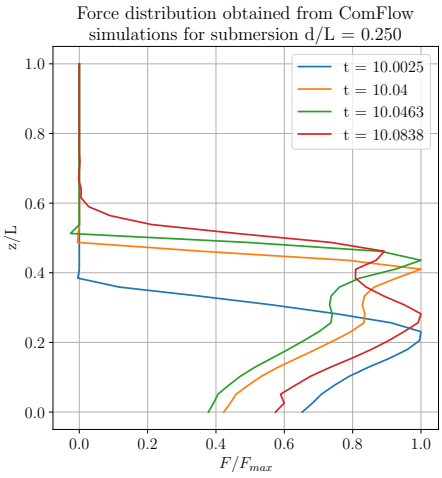

(b) *Force distribution obtained from ComFlow simulation for multiple timesteps in simulation for submersion ratio 0.25.*

Fig. 4.3 *ComFlow simulation outputs: power spectrum of impact force and force distribution along the plate.*

The force output from the preliminary simulations was also used to obtain the expected model response. Besides the total force on the plate, the force was also recorded for each section of 0.02 m along the height of the plate. The time traces of the forces obtained in this way are used as input in the finite element method model (further discussed in Section 5). This model was then used to get an estimate of the expected deflections and accelerations during the experiment. In turn, that information was then used for the selection of the laser sensors (for position) and the accelerometer for the experiment. An example of such a force distribution is given in Figure 4.3b. The force is given as function of position along the length of the plate and has been normalized using the maximum force at each timestep.

Pressure

Similar to the force output, the main purpose of the pressure output was to get an estimate of the required pressure range of the sensors in the experiment. Additionally, the simulations were used to determine the location of maximum pressure, which is the best location to place the pressure sensors. During the ComFlow simulations the pressures were recorded at intervals of 0.02 m along the height. From the simulations it was found that the maximum pressures occur in the area between 0.1 and 0.14 m above the still water line. In the experiment the pressures sensors are placed at 0.6, 0.1 and 0.14 m above the still waterline (this is further discussed in Section 6). Figure 4.4 shows the resulting pressure plots for a submersion depth of 0.2 m. Since the pressure sensors are above the water level for most of the simulation their output is 0 for most of the time. It can be seen that the risetime of the pressure is brief, about 0.03 seconds.

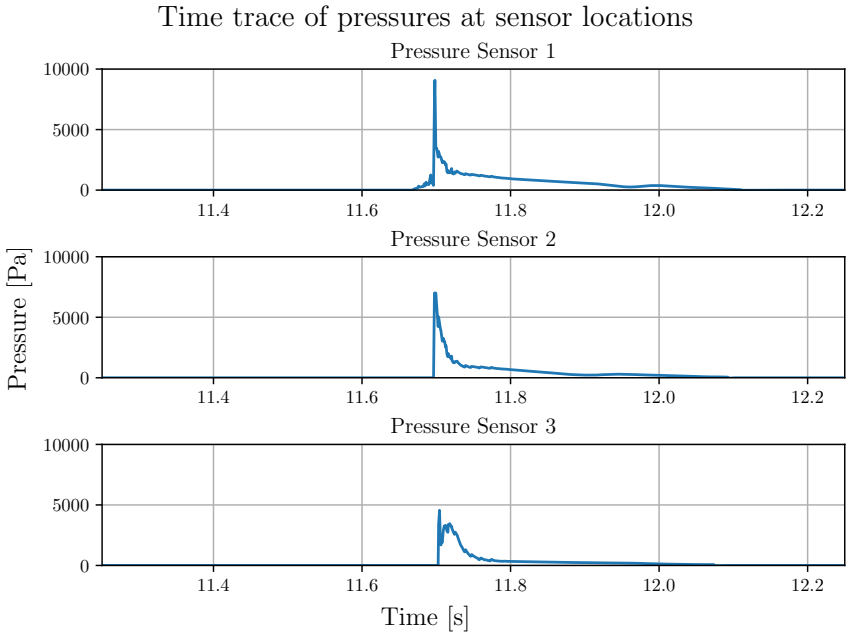

Fig. 4.4 *Time trace of the pressure measurements during the ComFlow simulation. Submersion is 0.25 of length, measured at 0.06, 0.1 and 0.16 m above waterline.*

4.3 Simulations of performed experiment

The simulations discussed before were done prior to the experiment. These used an expected wave profile as input. The wave used during the experiment was different due to poor focusing performance of the previously described wave. This section discusses the wave used for the experiment and the changes that were made to the simulation setup to simulate the updated experiment.

4.3.1 Changes to simulation setup

The wave eventually used in the experiment consists of the components shown in Table 4.2. These are the same components as used in [7] except the steepness is increased to H/λ = 1/40. The wavelengths are still between 1 and 5 m.

Table 4.2 *Wave properties of the components actually used to generate the focused breaking wave in the experiment.*

Component	1	2	3	4	5	6	7	8	9	10
λ [m]	1	1.1	1.25	1.45	1.7	2	2.4	2.9	3.6	5
Amplitude [m]	0.0125	0.0138	0.0156	0.0181	0.0213	0.0250	0.0300	0.0363	0.0450	0.0625
k [1/m]	6.283	5.712	5.027	4.333	3.696	3.142	2.618	2.167	1.745	1.257
ω [rad/s]	7.850	7.484	7.018	6.510	5.998	5.502	4.969	4.435	3.846	3.013
T [s]	0.80	0.84	0.90	0.97	1.05	1.14	1.26	1.42	1.63	2.09

During the experiment this wave was generated and then measured using a wave gauge located 4.8 meters in front of the model (this is discussed in more detail in Section 6). This wave gauge measurement was then used as an input for the ComFlow simulations. Since the input is closer to the model than in the preliminary simulations, the domain is shortened to 5 meters. For the simulations a discretization

of 500 cells in x-direction and 150 cells in z-direction was used, this corresponds to square cells with a side length of 0.01 m. A schematic overview of the setup can be seen in Figure 4.5.

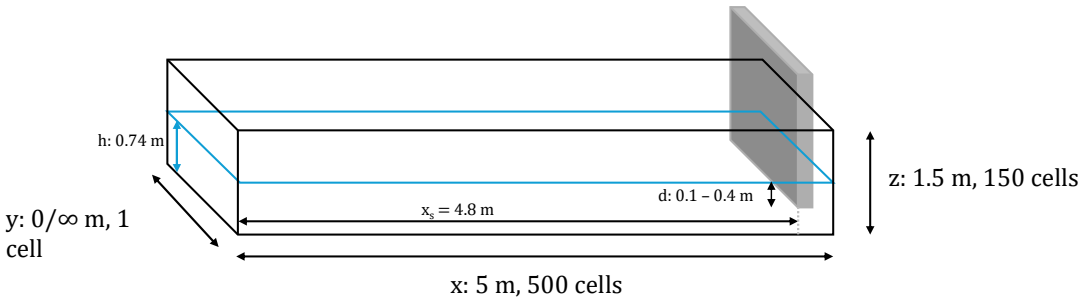

Fig. 4.5 *Domain used in the final two-dimensional CFD simulations including dimensions. The position of the structure (grey block) is also shown.*

4.3.2 Simulation results

Using the ComFlow simulations of the new wave, a new ideal distance between focus location and model was determined. It was found that this distance should be 1.5 meters. Additionally, the results showed that the force and pressures were expected to be slightly lower and therefore this wave could be used without changing the model and support structure. More detailed outputs from these simulations are shown in the results section (Section 7).

The pressure distribution from these ComFlow simulations (and the 3D simulations) was compared with the pressure distribution in the experiment, to assess the accuracy of the force distribution obtained from the ComFlow simulation. This force distribution was used for the FEM model described in Section 5 to obtain the final results of the one-way coupled model presented in Section 7.

4.4 3D simulations

After the experiments, it was found that the two-dimensional simulations did not capture the phenomena in all tests accurately. Three-dimensional simulations were ran to see if this improved the match between the results. A more detailed analysis of this is shown in the results section (Section 7). This section discusses the simulation setup for these 3D simulations.

In x- and z-direction the domain remains the same compared to the 2D simulations. The y-direction is extended to have a length of 1 m. It is assumed that the experiment is symmetric, so by making the domain wall at $y = 0$ m a symmetry plane, only half the actual domain has to be solved for. The plate extends from $y = 0$ m to $y = 0.5$ m. This leaves an open gap of 0.5 m next to the plate. This matches with the distance between the plate and the tank wall in the experiment. A schematic of the test setup can be seen in Figure 4.6.

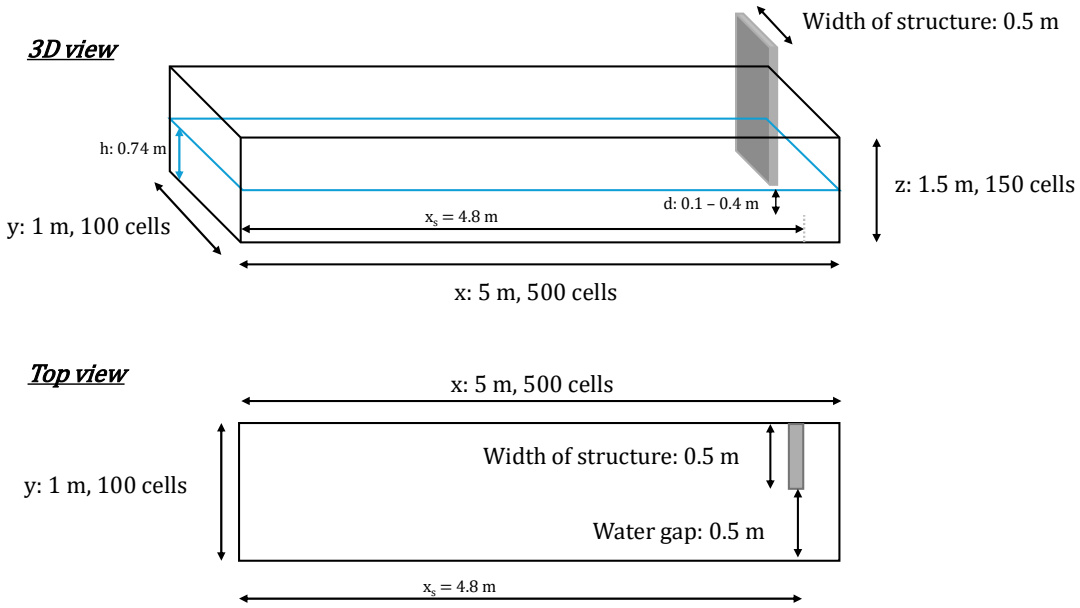

Fig. 4.6 *Domain used in the final three-dimensional CFD simulations including dimensions. The position of the structure (grey block) is also shown.*

5 Finite Element Method Model

The structural model used in this thesis is based on the Finite Element Method (FEM). This section explains the methodology behind the FEM model. First, a short explanation on FEM will be given. Next, it is explained how the FEM model was set up for this thesis. Lastly, the relevant results are presented.

5.1 Finite Element Method

FEM has a couple of strengths that make it suitable for the problem at hand, such as implementing specific boundary conditions at the bottom of the plate and the mass at the end. The load on the structure can be varied in space (along the plate) and in time. FEM can capture rapid changes in time accurately, which is relevant for an impact event such as in this problem. Only the parts of FEM specific to the problem are explained. For a more detailed explanation of FEM other sources are available such as [44]. For brevity, some details have been described in Appendix D, reference will be made to this appendix when relevant.

5.1.1 Domain Discretization

In a FEM model the domain, in this case the plate, is discretized into elements. The plate is clamped at the bottom and has a discrete mass along the top. It is expected that all (major) deformation will happen in the x-z-plane (so along the wave propagation direction). Since the plate and load are uniform along the y-axis, the response is assumed independent of width (which is the idea behind the two-dimensional approach). Plate effects such as bending in y-z-plane are assumed to be negligible and the plate can thus be modeled as a beam. For an Euler-Bernoulli (EB) beam the discretization is straightforward; the beam is split up along its length into many smaller beam elements. The discretization is schematized in Figure 5.1. For the results in this thesis the beam is discretized using 40 elements. This value has followed from a convergence study on the number of elements. This is further elaborated on in Appendix D.

5.1.2 Governing equations

The system modeled is an EB beam clamped at the bottom and with a mass at the free end. The characteristic equation of an Euler-Bernoulli beam is given by:

$$\rho A\ddot{u}(z) + EIu''''(z) = q(z) \qquad \text{for} \quad u(z,t) \;\; \forall \;\; z \;\in\; (0, L) \tag{5.1}$$

Deflection is represented using u, z denotes the length along the beam starting at the bottom (clamped) edge, ρ and E are the density and E-modulus of the material and I and A are the area moment of inertia and cross-sectional area of the beam. $q(z)$ represents a load distribution along the length of the beam. Using a finite element approach, the equation of motion of an individual element (k) is given by:

$$\mathbf{M}^k\ddot{\vec{u}}(t) + \mathbf{B}^k\dot{\vec{u}}(t) + \mathbf{K}^k\vec{u}(t) = \vec{q}^k(t) + \vec{s}^k(t) \tag{5.2}$$

$$\text{with:} \;\; \mathbf{M} = \mathbf{M}_{struc} + \mathbf{M}_a(\omega) \;\; \text{and} \;\; \mathbf{B} = \mathbf{B}_{struc} + \mathbf{B}_{hydro}(\omega)$$

$\mathbf{M}$ is the mass matrix, which depends on ρA and the length of an element, $\mathbf{M}_a$ is the added mass matrix (explained in Section 5.2.2). $\mathbf{B}_{struc}$ is the damping matrix as a result of structural damping, and $\mathbf{B}_{hydro}$ is the damping matrix resulting from hydro-dynamic damping (explained in Section 5.2.3). Both $\mathbf{M}_a$ and $\mathbf{B}_{hydro}$ are zero for all non-submerged elements. $\mathbf{K}$ represents the stiffness matrix which depends on the structural properties E and I. $\vec{q}$ is the loading vector on the element, which will contain the hydro-dynamic force as explained in section 5.2.1. $\vec{s}$ contains the internal forces between elements

which will cancel in global assembly and are therefore not discussed further here. Each element has 4 degrees of freedom: deflection (u) at both ends, and rotation (u', derivative of u in space) at both ends, so the $\vec{u}$ vectors have dimension 4x1, each matrix in this equation has dimensions 4x4 and the $\vec{q}$ vector has dimension 4x1.

For each element in the discretized domain these matrices have to be computed and then assembled together to create the global equation of motion as seen in Equation 5.3. Each element shares a node with the previous element on one side and the next element on the other side, so the first two DOFs are shared with the previous element and the last two DOFs are shared with the next element (this is visualized in Appendix D). As a result, the sizes of the matrices are equal to $2n$x$2n$ (n = number of elements). The $\vec{u}$ vectors are $2n$x1, since there are $2n$ degrees of freedom (u and u'). After global assembly this results in the global equation of motion:

$$\Big(\mathbf{M}_{struc} + \mathbf{M}_a(\omega)\Big)\ddot{\vec{u}}(t) + \Big(\mathbf{B}_{struc} + \mathbf{B}_{hydro}(\omega)\Big)\dot{\vec{u}}(t) + \mathbf{K}\vec{u}(t) = \vec{q}(t) \tag{5.3}$$

Increasing the number of elements will further increase accuracy, but will also increase computational times due to the increased number of DOF, which means more equations have to be solved at each timestep. Convergence studies on the number of elements for this model have shown that using 40 elements gives errors smaller than 0.1% on the first 3 natural frequencies (see Appendix D). As a result, all matrices are 80x80 and all vectors 80x1, and the system has to be solved for 80 DOFs. Section 5.2 will explain how the values used to fill the matrices in Equation 5.3 have been obtained.

5.1.3 Boundary conditions

The plate in the model is clamped at the bottom and has a discrete mass along the top. The clamped bottom node cannot move, which means its deflection (u) and rotation (u') are equal to 0 at all times. The boundary conditions for the first node can thus be defined as:

$$u(t) = 0 \qquad \text{and} \qquad u'(t) = 0 \tag{5.4}$$

In the finite element model, this means that the first two entries in $\vec{u}$ and its derivatives are known to be zero at all times: $\ddot{u}_{1,2} = \dot{u}_{1,2} = u_{1,2} = 0$. This reduces the number of DOFs to 78.

The top of the plate is free to move so the number of DOFs cannot be reduced here. To deal with the mass along the top edge the last entries of the mass matrix need to be changed. The mass is added to the part of the mass matrix corresponding to the translation of the last node (end of the plate). Figure 5.1 shows the structure as it is discretized in the FEM model, including the boundary conditions.

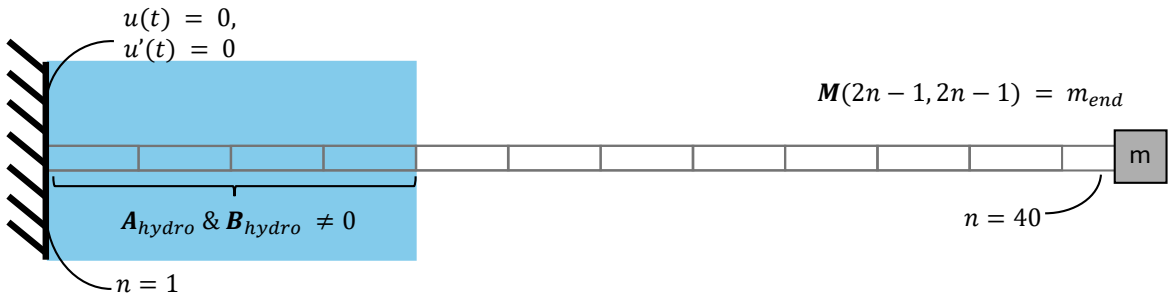

Fig. 5.1 *Schematic of the analysed system in FEM including the discretization of the system and the boundary conditions. The model is shown in a horizontal instead of vertical orientation.*

5.2 Inputs for model

5.2.1 Force model from CFD ($\vec{q}$)

The force in the model is obtained from CFD in a one-way coupled manner. This means the model is not hydroelastic since no coupling between the structural response and the load exist. The pressure gives a distributed force and this distribution is used to fill the force vector $\vec{q}(t)$. The FEM model can also take moments as input, but these are kept at 0, as it is assumed the horizontal force and translation are the dominating loading and response.

5.2.2 Added mass model ($\mathbf{M}_a$)

$\mathbf{M}_a$ represents the added mass matrix. The added mass of the plate used in the experiment was computed using OrcaWave. OrcaWave is a diffraction analysis program that can be used to compute the added mass and damping coefficients of structures [45]. The plate was meshed using GMSH, which is an open source 3D finite element mesh generator [46]. The plate was discretized into smaller horizontal strips to determine the added mass separately for each of these strips. OrcaWave can only do analysis on rigidly moving structures so this introduces an error in the computation of the added mass and damping values. The added mass and damping values were determined for all submersion depths with the water depth in the tank to represent the situation in the experiment as closely as possible. With this analysis the frequency dependent added mass was computed for each strip. This was then used to determine the added mass of each element in the FEM model. Each strip had the same size as the elements in the FEM model, so the added mass for each strip is considered representative of the added mass at the corresponding element. This frequency dependent added mass was used directly in FEM to determine the natural frequencies and mode shapes of the models used in the experiment. This is explained in more detail in Section 5.3. The added mass of an example element following from this analysis can be found in Figure 5.2. The added mass is given for various depths z, normalized by submersion depth d.

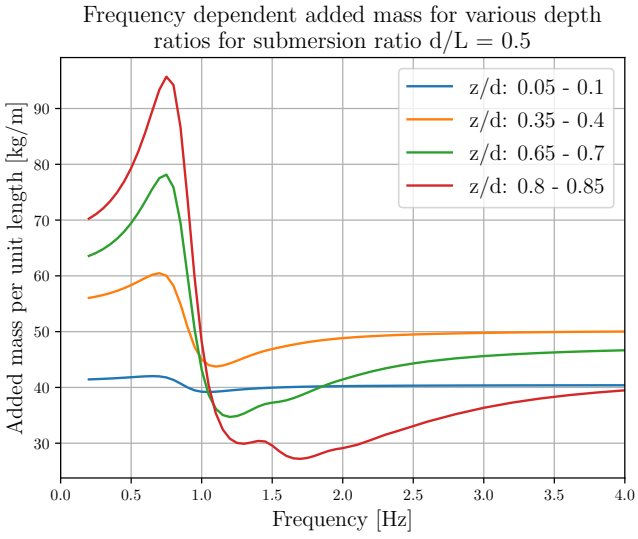

Fig. 5.2 *Example output of frequency dependent added mass from OrcaWave. It is clearly visible that the added mass only varies significantly over a small section of the frequency range.*

A caveat of this method is that it implicitly assumes constant water height. The elements below the still waterline are assumed to always be affected by added mass (and damping), even when there is a wave

trough. Similarly, the elements above the still waterline are not affected by added mass or damping even when the water crest is above the still water line. Depending on the water height at a certain time instant, this will lead to over- or underestimation of the added mass and damping.

5.2.3 Damping models ($\mathbf{B}_{struc}$ and $\mathbf{B}_{hydro}$)

Structural damping matrix

Structural damping is the result of the dissipation of energy within a structure when it vibrates caused by internal friction [47]. Different values have been reported in literature for an accurate estimate. In this thesis the structural damping is determined experimentally using dry decay tests. The method behind these is explained in more detail in Section 6.4. Tuning the structural damping in the model to match the decay tests improves the accuracy of the structural model. This minimizes errors in the resulting arising from structural behaviour. This is important because the focus of this thesis is on hydroelasticity not on structural modeling. The structural damping matrix will be tuned in such a way that the FEM model will accurately predict the response of the structures in these decay tests.

Hydrodynamic damping matrix

The entries for the damping ($\mathbf{B}$) matrix were computed in the same OrcaWave analysis used for the added mass matrices (Section 5.2.2). The damping for an example element in the FEM model following from this analysis can be seen in Figure 5.3. The damping is given for various depths z, normalized by submersion depth d.

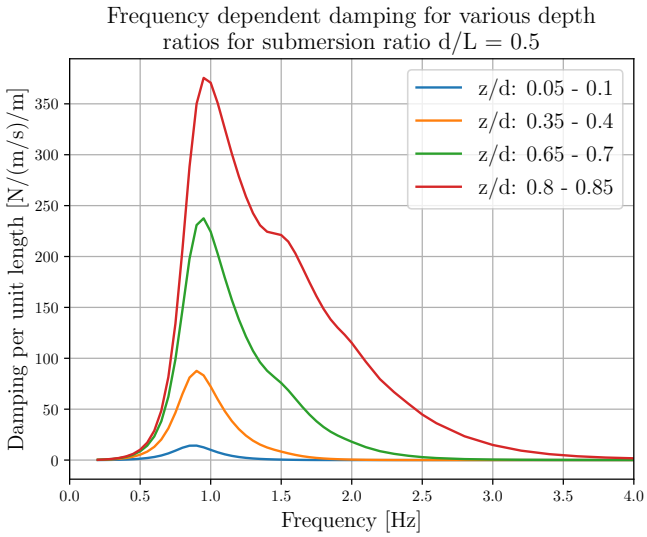

Fig. 5.3 *Example output of frequency dependent damping from OrcaWave.*

Neglected damping effects

In reality an OWT is also subjected to aerodynamic damping. However, during a parked condition (which is assumed in this thesis) this damping is almost negligible [47]. In this thesis the damping due to air friction is ignored. It is assumed that in the experiment the air effect is small enough to make this assumption reasonable. Additionally, since the structural matrix is tuned to the decay tests (which includes air damping) some of these air damping effects will be captured already when tuning the structural matrix.

5.3 FEM model results

5.3.1 Natural frequencies

The FEM modal was used to estimate the natural frequencies and mode shapes of the models used in the experiment. This way, the models could be chosen in such a way that hydroelastic effects were to be expected. The method to determine these frequencies is described below.

The natural frequencies and mode shapes of the structure depend on the mass matrix ($\mathbf{M} + \mathbf{M}_a(f)$) and stiffness matrix ($\mathbf{K}$). Since $\mathbf{M}_a$ also depends on frequency an iterative approach is required. This iterative approach is defined as:

$$\text{Start at } f_{old} = 0 \quad \text{then: } f_{new} = \frac{1}{2\pi}\sqrt{\frac{\mathbf{K}}{\mathbf{M} + \mathbf{M}_a(f_{old})}} \qquad \text{repeat until: } f_{new} = f_{old} \tag{5.5}$$

This iteration was done for the first two natural frequencies separately. Modes above the second are determined using the $\mathbf{M}_a$ value corresponding to f_2, since for these modes the high frequency limit of the added mass has been reached and further iteration does not change the value of $\mathbf{M}_a$, since these are all equal to $\mathbf{M}_a(\infty)$. For example, the third natural frequency is around 60 Hz. This high frequency limit can also be seen in Figure 5.2.

From the ComFlow studies (Section 4) it was found that the impact has a risetime of approximately 0.4 seconds. Using the Bereznitski ratio [4], this leads to a desired natural frequency of the model around 2.5 Hz. Additionally, the power spectrum showed that most of the energy is located at frequencies below 2.5 Hz. Using the method above it was found that a 4 mm aluminium plate with different end-masses gives a set of models with frequencies in this range. The mass ratio of the system is defined as the ratio of the end-mass over the plate mass. According to the FEM model, taking mass ratio's between 0 and 1.5 and submersion ratios between 0.125 and 0.5, the plate length gives natural frequencies between 5.33 and 1.90 Hz. Using this information the varations in the experiment were chosen to be:

- Mass ratios, end mass over plate mass: 0.0, 0.2, 0.5, 1.0, 1.5
- Submersion ratios, depth (d) over plate length (L): 0.125, 0.250, 0.375, 0.500

5.3.2 Structural response

Maximum deflection and acceleration

The FEM model was created to model the quasi-static response of the structures to compare against the experimental outcome. It was also used to determine the expected order of magnitude of the response in the experiment. This way the FEM model was used in the design of the experimental setup and for sensor selection (as further described in Section 6.3). The important outputs are the expected deflection (for the laser sensors) and the expected accelerations (for the accelerometer). These outputs were also used for more practical design choices such as the space needed in the setup to accommodate for the expected deflections. The most critical case for these two variables is the test case with submersion ratio 0.5, since the force on this structure is largest (as seen in Section 4.2.4) and acts furthest away from the base of the plate. The timetrace of this response can be seen in Figure 5.4. This response is calculated using the force outputs from the CFD simulations that were ran prior to the experiment. According to the model, the maximum deflection will be around 136 mm and the maximum acceleration around 44 m/s^2.

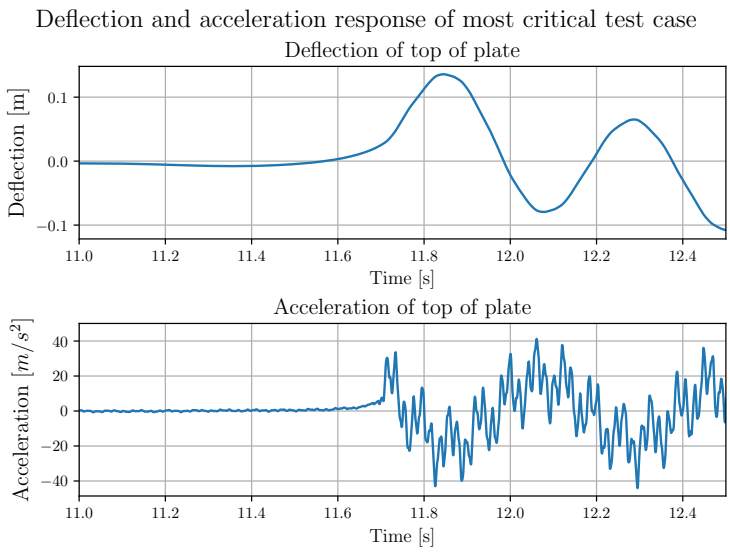

Fig. 5.4 *Output of the model for the testcase with the most critical (expected) response. As seen in the graphs the maximum deflection is expected to be around 136 mm and the maximum acceleration is expected to be around 44 m/s^2.*

Since the structural damping coefficient was determined using the decay tests in the experiment, it is still absent in these simulations. Therefore, the actual response is expected to be lower and the estimates were assumed conservative. Especially the high accelerations are expected to be lower with more structural damping.

Bending stress check

Another important check was to determine whether the plate would undergo plastic deformation. Using the computed responses it is quite straightforward to determine the maximum occuring bending stress in the plate using Equation 5.6 and Equation 5.7. Equation 5.6 is used to determine the bending moment in the beam using the fourth derivative of the deflection, the E-modulus and area moment of inertia (I). Equation 5.7 uses this bending moment to determine the bending stress at the outer fibre of the beam using the distance from the centerline (x).

$$M(z) = EI_y \frac{d^4u(z)}{dz^4} \tag{5.6}$$

$$\sigma_z = \frac{M_y x}{I_y} \tag{5.7}$$

The most critical case is again the plate with submersion ratio 0.5 since this plate has the largest deflections. The stress distribution in the plate at the moment in time corresponding to the highest stress can be seen in Figure 5.5. As seen in this figure, the maximum stress is 120 MPa, close to the yield stress of aluminium, which is 145 MPa . As explained before, the response is expected to be conservative, so this was deemed to conform to the ambitions of the experiment. However, to anticipate the potential failure of the plate, this test was done last so that plate failure would not be a problem for the rest of the experiment.

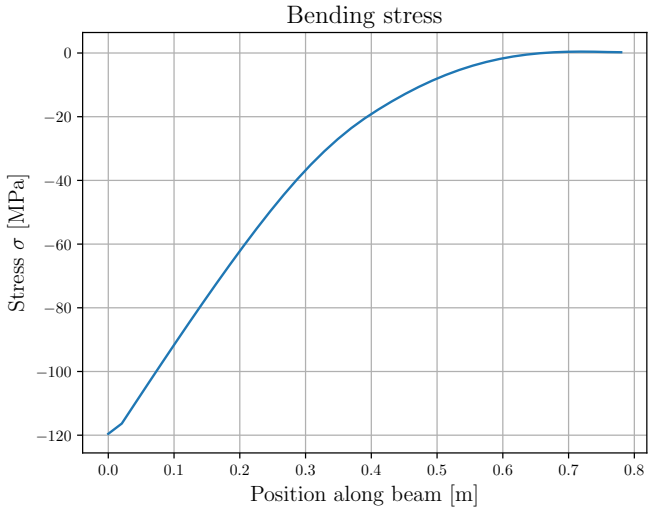

Fig. 5.5 *Output of the model for the testcase with the most critical (expected) stress. As seen in the graphs the maximum stress is expected to be 120 MPa.*

6 Experiments

To answer the research questions, an experiment was conducted which is described in this section. The section starts with a general description of the experiment. Next, the design of the experiment and the recorded data will be explained. The section ends by explaining and motivating the test matrix.

6.1 Description of the experiment

The model used in the experiment is a plate with a variable mass along its top edge. The plate is clamped at the bottom edge and free along the two side edges. During the experiment, the end-mass and submersion depth at the base of the plate were varied to study the effect of these structural properties on hydroelasticity. The structures are loaded by a breaking wave impact created by focusing multiple wave components. The wave was generated using the wave maker in the towing tank in the Ship Hydromechanics lab at TU Delft.

For each submersion depth, a rigid plate (which has minimal hydroelastic effects) is loaded to determine a reference force. The forces measured on the flexible (hydroelastic) models, for which the end-mass and submersion depth is varied, are compared against this force to determine the extent to which hydroelasticity played a role in the event. Since all structures are loaded by the same wave on the same surface area, the force should be the same when no hydroelastic effects occur. The response of the structure is recorded using multiple lasers (measuring the position) and an accelerometer located at the top of the plate. The sensors are explained in more detail in Section 6.3. The data from these sensors is used to compare against the one-way coupled FEM model, to make a comparison between the quasi-static response and the hydroelastic response in the experiment.

An experiment is the most effective way of capturing the highly non-linear effects present in a breaking wave impact event in which hydroelasticity plays a role. Numerical models would require complex fully coupled models. For these models validation would be needed, still leading to an experiment to obtain validation case. As a result, for this study, an experiment is a more effective method to answer the research questions in this thesis. The dataset created in the experiment will be compared with the FEM model explained in Section 5. Additionally, the dataset can be used to validate other (future) numerical models so that numerical studies of these events will be more accurate in the future.

6.2 Test setup

This section explains the test setup used in the experiments. It starts by explaining the main design considerations and the general experimental setup. Next, it explains the separate parts of the experimental setup in detail.

6.2.1 Overview of design

The wave tank in which the experiment was conducted is 2.75 m wide, 85 m long and has a water depth that can be varied between 0.5 and 1.25 meters. In reality a bottom-fixed wind turbine is connected to the seafloor and usually has about 1/3 to 1/4 of its total height (monopile + transition piece + turbine tower) submerged in the water. With the available water depths in the tank, such ratios would require test models too large to be feasible for this study. Additionally, placing sensors underwater adds extra complexity to the setup. To solve these challenges, a setup was designed in which the model is clamped to a support structure hanging from the towing carriage (the substructure). This allows for a smaller model since the structure can be submerged for less than the actual tank water depth. This substructure

is connected to the fixed world (towing carriage and base structure) through the force sensors measuring the total force on the model. The setup can be seen schematically in Figure 6.1. The following sections will explain the parts of this setup in more detail.

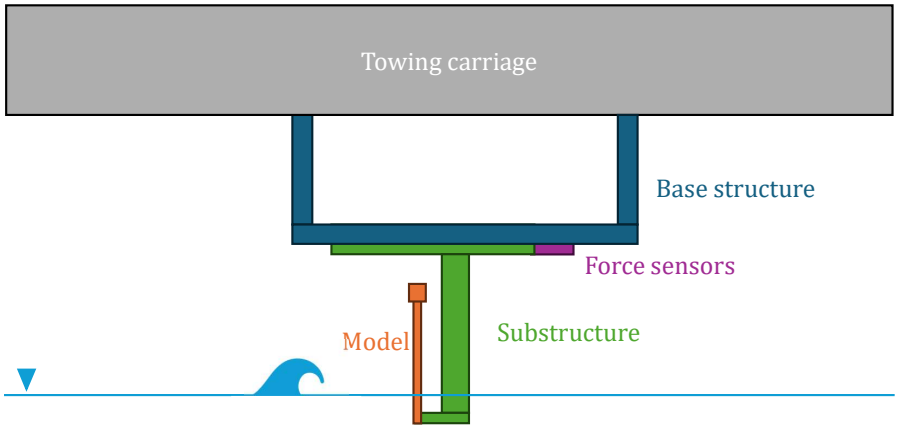

Fig. 6.1 *Schematic overview of experimental test setup. The green and orange sections are connected to the base structure (blue) through the force sensors (purple).*

The model is located 29.8±0.1 meters away from the wavemaker. Wave gauges are located at 25.0±0.1 and 28±0.1 meters from the wave maker, with the wave focused at 28.3 meters. The tank setup is shown schematically in Figure 6.2.

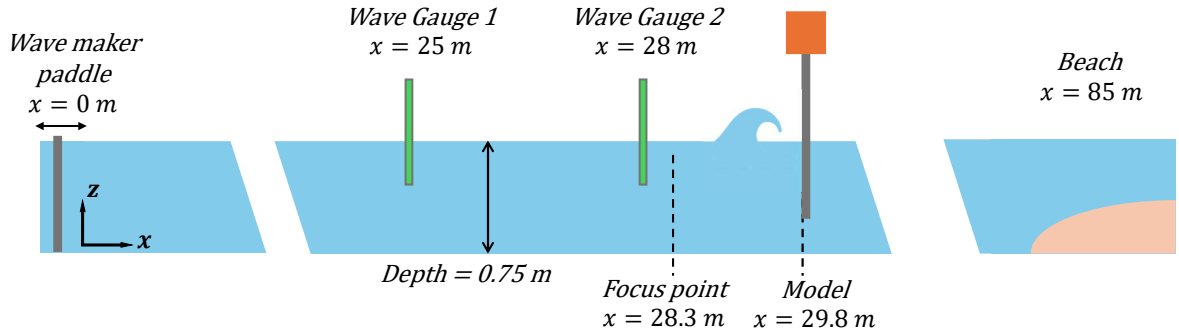

Fig. 6.2 *Schematic overview of wave gauges placement in the experiment.*

6.2.2 OWT models

Two different OWT models are used. The first is designed to be rigid in order to obtain a reference force for a situation without hydroelasticity. The second model is a flexible structure to study the effect of end mass and added mass on hydroelasticity. Both models are explained in this section.

Flexible OWT model

The flexible model consists of a 1 m wide, 4 mm thick, 0.8 m (0.5 mm tolerance) high aluminum plate with a changeable end-mass along the free top edge. The bottom of the plate is clamped to represent the bottom-fixed nature of the OWT. Since the plate mass, end mass and moment of inertia of the plate all depend linearly on the width of the plate, the width does not influence the natural frequencies of the plate. As explained in Section 3, the experiment is designed to be as two-dimensional as possible

which means that the plate is uniform and wide in y-direction, so end-of-plate effects on the load are negligible. From restrictions due to the width of the towing carriage and weight considerations, the final width chosen for the plate was 1 meter. This yields a plate mass of 8.64 kilograms.

The end-masses used in the experiment are 0, 1.8, 4.3, 8.4 and 12.8 kg (measured with a tolerance of $\pm$ 1 gram), corresponding to mass ratios of approximately 0, 0.2, 0.5, 1 and 1.5. These masses are obtained by using steel blocks of 1 meter long (width of the plate) and 0.02 m high with various thicknesses to achieve the different masses. Half of the mass is located at the front, and half at the back of the plate, to prevent an asymmetric dynamic response. The masses connected to the plate can be seen in Figure 6.3.

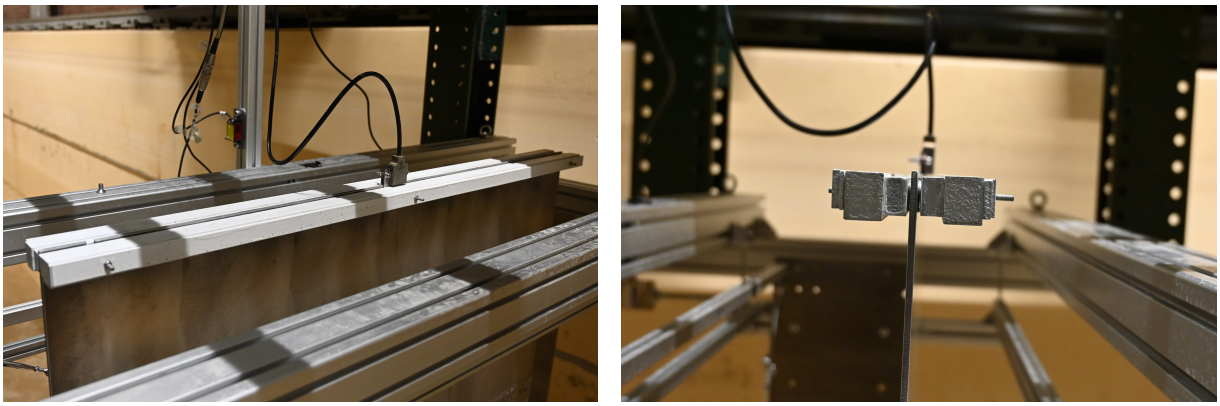

(a) *Full view of masses connected to the plate.* **(b)** *Side view of the masses connected to the plate.*

Fig. 6.3 *Pictures of the masses used in the experiment.*

Rigid OWT model

The rigid OWT model is used to obtain a non-hydroelastic reference force. Its impact area should be equal to that of the flexible plate. The rigid plate has to be stiff with a high natural frequency to minimize hydroelastic effects. This plate is also 4 mm thick, 1 m wide and 0.65 m high. The plate is clamped at the bottom like the flexible plate. To achieve the required high stiffness and natural frequency, the plate is also clamped at the top and has stiffeners in the vertical direction (as seen in Figure 6.4b). The result is a stiffened fixed-fixed structure which has a much higher natural frequency than the flexible systems. This plate does not have an end-mass along its top. Another difference with respect to the flexible plate is the presence of pressure sensors. Details on the pressure sensors are given in Section 6.3.

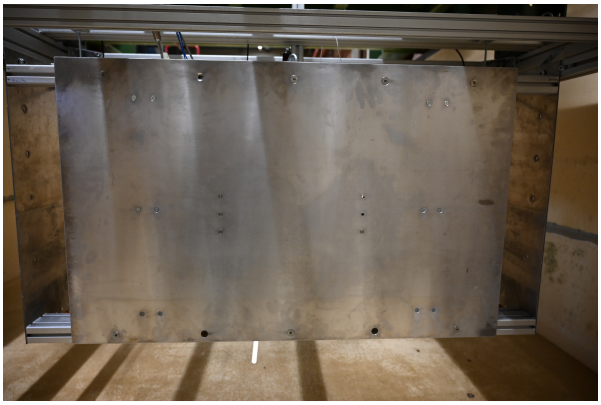

(a) *Front view of rigid plate.*

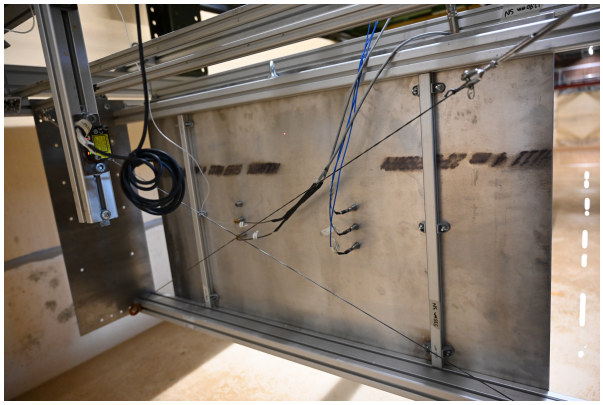

(b) *Rear view of rigid plate, with the stiffeners and two rows of pressure sensors visible.*

Fig. 6.4 *Pictures of the rigid plate used in the experiment.*

6.2.3 Substructure

The main purpose of the substructure is to create an artificial seafloor onto which the OWT model can be attached. The plate is clamped to a crossbeam which hangs from two thin surface-piercing plates (3 mm thick steel). These surface piercing plates are attached to a frame, which is attached to two force sensors. These force sensors measure the total resultant force on the plate. The submersion depth can be varied by changing the point at which the side plates are connected to the top frame. Cross-wires between the top frame and the crossbeam make sure the structure is stiff in sway direction to keep the whole hanging frame square. Since the side plates and crossbeam are also in contact with the impact wave, the force measured will be slightly higher than the force on the model alone. During the experiment it was found that this error was below 5% as shown in Appendix A.

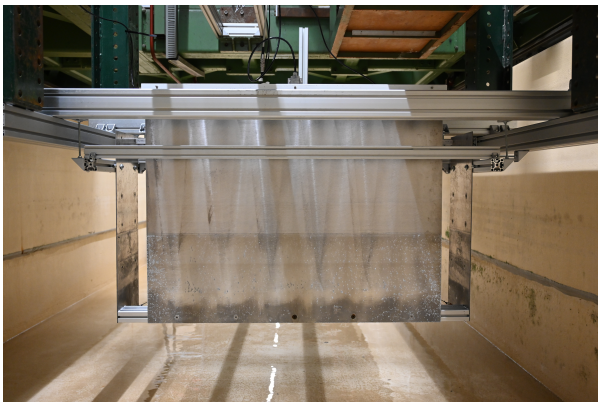

(a) *Front view of the substructure with flexible plate attached.*

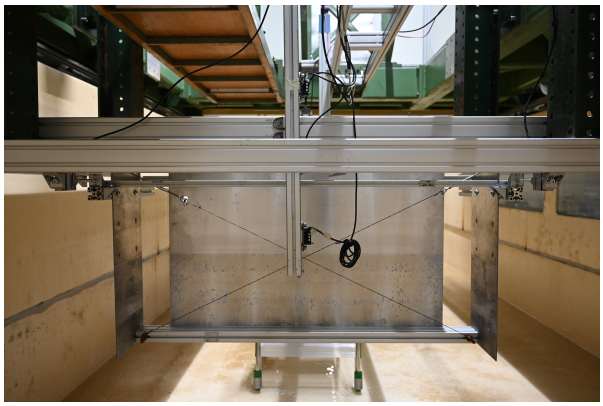

(b) *Back view of the substructure.*

Fig. 6.5 *Pictures of the substructure in the experiment.*

The substructure is connected to the base structure using four vertical 6 mm diameter steel bending rods, one horizontal 6 mm diameter steel bending rods constraining the horizontal direction perpendicular to the wave direction and finally the two force sensors, which measure the force in wave direction. These bending rods constrain the substructure in all degrees-of-freedom except surge, which is the direction in which the force is measured. In surge, the bending rods do not constrain the motion but they

do add a small amount of stiffness to the system. Since the force sensors use the measured deflection and the known sensor stiffness to compute the force on the structure, adding too much stiffness will lead to a large error on the measured force. This error is equal to the ratio of the (total) sensor stiffness over the (total) bending rod stiffness. The two force sensors used (see Section 6.3) have a combined stiffness of 1.1E7 N/m. Using these dimensions for the bending rods this ratio is roughly 100 which means the bending rods cause a 1% error in the force measurements, which is acceptable.

The measuring system itself has a natural frequency in surge. To prevent this frequency from interfering with the measurements, the setup is designed in such a way that its natural frequency is much higher than the frequencies of the measured physics. The surge natural frequency of the measuring system has been designed to be above 90 Hz, which is much higher than the natural frequencies of the models and the frequencies present in the wave impact. Unfortunately, during the measurements a disturbance frequency was seen, this is discussed in more detail in the results (Section 7).

6.2.4 Base structure

The main purpose of the base structure is to extend the towing carriage to serve as a connection point for the substructure. This component is in effect part of the fixed world and should therefore be as stiff as possible. Since the mass of this part of the structure does not matter (within installation limits) stiff profiles were used for this part of the setup. The connection between the base structure and the substructure is formed using the bending rods and force sensors. The laser sensors are also connected to this base structure.

6.3 Collected data and sensors

6.3.1 Force

During each impact event the total force on the structure is measured. All tests are done using the same wave, resulting in the same loading condition (when neglecting hydroelasticity). Since all structures (at a specific submersion depth) have the same impact area, the measured total force is expected to be the same unless there is hydroelasticity present. Comparing the force on the flexible and rigid structures can thus be used as an indication of the extent to which hydroelasticity is present in an impact event. This approach is similar to the approach in other studies [4][28]. Two Zemic H3 100kg force sensors are used to measure the force exerted on the structure. The performed calibration showed an average normalized residual of 0.1% and 0.15% (normalized to calibration range). The force sensors were calibrated in tension and compression (Appendix C).

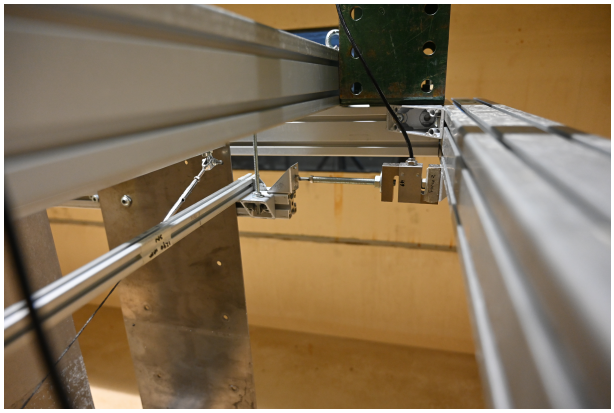

Fig. 6.6 *Force sensor placement in experiment.*

6.3.2 Position and acceleration

Since hydroelasticity is strongly coupled to structural response, this response is measured in detail. The deflection of the plate is measured at three locations; at the height of the impact, at the height of the end mass and at a location between these two points. The positions are given in Table 6.1 Assuming that the deformation is dominated by the first two modes the structure's deflection can be accurately measured this way. The used laser sensors are of the type Panasonic HG-C1400. From the calibration it was found that these have normalized residuals of 0.07, 0.08 and 0.08% (Appendix C).

The accelerometer is attached to the end-mass, which is the point where the largest accelerations occur. The acceleration sensor used is a Murata sensor with a normalized residual of 0.3% (Appendix C).
The top laser is aimed at the accelerometer. By measuring the position and acceleration at the same location, the velocity can also be determined by integration of the acceleration and/or by differentiating the position over time. The position, velocity and acceleration of the structure will be compared to the quasi-static response computed using the FEM model. The placement of the lasers and accelerometers can be seen in Figure 6.7 and Table 6.1.

(a) *Laser sensors placement in the experiment.*

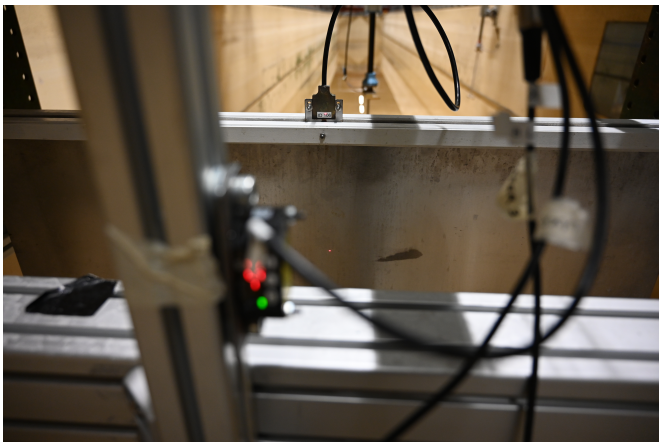

(b) *Accelerometer placement in the experiment, in the front the top laser is visible, which measures the position of the accelerometer.*

Fig. 6.7 *Placement of lasers and accelerometer in the experiment.*

Table 6.1 *Location of laser sensors during experiments. Positive means above top of plate, negative below top of plate.*

	Distance from top of plate [mm]			
d/L	**0.125**	**0.250**	**0.375**	**0.500**
Laser 1	+2	+3	+2	+2
Laser 2	-193	-106	-174	-
Laser 3	-446	-279	-251	-

6.3.3 Pressure

For the tests on the rigid plate, the pressure is also recorded. This is not possible in the flexible plates since the presence of the pressure sensors would likely affect the structural properties of the plate. The

measurements of these pressure sensors are compared with the ComFlow simulations to determine the accuracy of the force distribution from the simulations. The pressure sensors are added to the plate at 3 different heights. These heights correspond to the height above the waterline at which the pressures were highest according to the ComFlow simulations in the 200 mm submersion test scenario. From the bottom of the plate, the laser sensors are positioned at 260 mm (P1), 300 mm (P2) and 340 mm (P3) height. The sensors are mounted using connection pieces that are flush with the plate to make sure the plate surface is as flat as possible.

Two rows of pressure sensors have been used. One row contains Druck PDCR 42 pressure sensors with a range of 350 mbar and 175 mbar. These have a normalized residual of 0.22 and 0.1% respectively. The other row contains PCB 113B24 pressure sensors with a range of 3.5 bar and normalized residuals of 0.55%. The calibrations are shown in Appendix C. The pressure sensors and installation method can be seen in Figure 6.4.

6.3.4 Wave height

The wave height is measured at two locations using wave gauges. The wave gauges are fabricated by the technicians at the lab. They were calibrated each morning of testing. These calibrations are shown in Appendix C. The front wave gauge was located 4.8 m in front of the structure. The second wave gauge was located 1.8 m in front of the structure and 0.3 m before the focus point of the wave. These locations are also shown in Figure 6.2.

The signal from the front wave gauge is used as input for the CFD simulations of the experiment. The measurements from the second wave gauge can than be used to compare the wave propagation in the experiment with the wave propagation computed by ComFlow (see Section 7). Additionally, they can be used to compare the runs to check the repeatability between the generated waves during runs. Lastly, they can be used to assess the signal for any reflection occurring on the front side of the model.

6.4 Test matrix

The test matrix consists of four sections. First, the support structure without plate attached is loaded at all four submersion depths (d); 100, 200, 300 and 400 mm, corresponding to submersion ratios (d/L) of: 0.125, 0.250, 0.375, 0.500. This is done to determine the magnitude of the force that is measured on the support structure instead of on the plate. Next, the rigid plate is tested at the four submersion depths. This is done to determine the reference force for a situation without hydroelasticity. This reference test is done for all depths since the loading changes slightly with wetted area, which is larger for larger submersion depths, and therefore a separate reference force is needed for each depth.

The flexible plate is loaded for all five mass ratios (0, 0.2, 0.5, 1.0, 1.5) at d/L 0.125 and 0.250. At d/L 0.375 and 0.500 the plate is only loaded with mass ratios 0 and 1.0. The test matrix can be seen in Table 6.2. Each test in the test matrix was repeated 5 times.

Table 6.2 *Test matrix for the experiment.*

Test goal	Mass ratio	Submersion ratio (d/L)	Plate	Wet first nat. freq. [Hz]	Wet second nat. freq. [Hz]
End-mass effect	0	0.125 / 0.250	Flexible	5.066 / 5.049	31.634 / 29.340
	0.2	0.125 / 0.250		3.711 / 3.708	26.026 / 24.670
	0.5	0.125 / 0.250		2.901 / 2.899	24.294 / 23.142
	1	0.125 / 0.250		2.268 / 2.267	23.396 / 22.338
	1.5	0.125 / 0.250		1.907 / 1.906	23.016 / 21.995
Added mass effect	1	0.375 / 0.500	Flexible	4.940 / 4.612	23.552 / 19.567
	1	0.375 / 0.500		2.262 / 2.240	18.704 / 14.888
Reference force	-	All ratios	Rigid		
Support structure effect	-	All ratios	No plate		

Decay tests

Besides the test matrix explained above, free vibration decay tests were conducted. During these tests the plate is given an initial displacement and then released. The response of the plate is measured using the lasers and accelerometers. Taking an FFT of this response shows the natural frequencies of the model. The performed type of decay tests are:

- Dry decay tests: structure out of the water. Performed for all mass ratios. Goal: validate FEM model and determine structural damping. Repeated three times.
- Wet decay tests: structure in water. Performed for all flexible tests in Table 6.2. Goal: determine effect added mass and validate added mass computation FEM model. Repeated three times.
- Impact tests rigid plate. Structure is hit to excite response in experimental setup. Goal: determine natural frequencies of measuring system and to test whether there are interfering modes in test setup. Eight impact tests were done.

Using the dry decay test, the structural damping can be determined, which is needed to tune the FEM model (see Section 5.2.3). This can be done by measuring the decay during the free vibration phase and translating this to a structural damping coefficient. The dry decay tests can be used to validate the purely structural part of the FEM model. The wet decay tests include added mass and damping and can be used to validate the added mass computation of the FEM model.

7 Results

In this section, the results from the experiment and numerical models are presented. First, the natural frequencies of the models in the experiment are analyzed. Next, the experiment and CFD simulations are compared. Following this, the effect of end mass and added mass and the influence of the structural modes is discussed. The section ends with a comparison between quasi-static response and the experimental, hydroelastic response.

7.1 Natural Frequencies

Before the plate was installed in the experimental setup, a separate setup was constructed to perform dry decay tests on the plate using various end masses. The purpose of this test was to assess the performance of the FEM model. The results from this test can be seen in Table 7.1. The measured results are given as an average of the three decay tests per configuration including the standard deviation between these three tests. For comparison, the first natural frequencies calculated using the analytical expression (Equation 1.5) are also given.

Mass ratio	0.0	0.5	1.0	1.5
f_1 measured [Hz]	5.04 $\pm$ 0.044	2.89 $\pm$ 0.018	2.23 $\pm$ 0.015	1.87 $\pm$ 0.001
f_1 FEM [Hz]	5.067	2.901	2.268	1.907
Error [%]	-0.54	-0.38	-1.70	-1.98
f_1 analytical [Hz]	5.066	2.892	2.263	1.903
Error (w.r.t. experiment) [%]	-0.53	-0.06	-1.47	-1.79

Table 7.1 *Results from decay tests performed using the OWT models in a different setup prior to experiment. The results are compared with the results from the FEM model.*

As seen in the table, the FEM model performs well and only slightly overestimates the natural frequencies. This could be caused by a small differences between the assumed and actual structural values of the plate, such as the E-modulus. Additionally, the test setup is not perfectly stiff, which can also slightly lower the natural frequencies of the plate.

Next, with the model installed in the experimental setup, the natural frequencies were determined for each configuration (added mass and end mass) of the test matrix. The results of these tests are presented in Table 7.2. The results are given as an average of the three decay tests per configuration including the standard deviation between these three tests.

	Mass ratio end mass/plate mass									
	0		0.2		0.5		1		1.50	
Depth	Exp.	FEM	Exp.	FEM	Exp.	FEM	Exp.	FEM	Exp.	FEM
100	4.37 ±0.019	4.36	3.25 ± 0.023	3.244	2.58 ± 0.033	2.555	2 ± 0.00	2.006	1.67 ± 0.035	1.69
200	4.17 ± 0.00	4.32	3.31 ± 0.018	3.23	2.5 ± 0.00	2.548	2.02 ± 0.004	2.002	1.61 ±0.013	1.688
300	4.07 ± 0.05	4.19	-		-		2 ± 0.00	1.986	-	
400	3.44 ± 0.045	3.65	-		-		-		-	
Dry	4.45 ± 0.033	4.365	3.28 ± 0.039	3.245	2.65 ± 0.017	2.555	2.00 ± 0.00	2.006	1.65 ± 0.019	1.69

Table 7.2 *Results from decay tests performed during experiments compared against results from FEM model with the unwanted mode in test setup included.*

Comparing the results of the dry decay tests against those in Table 7.1 shows that there is a significant decrease in natural frequencies when the model is placed in the experimental setup. This was probably caused by the test setup being more flexible than the test setup used outside the tank, which causes the natural frequencies to drop. The flexibility is thought to be caused by an unexpected mode in the test setup, discussed in more detail in Section 7.3. This mode was included in the FEM model by adding a spring connection to the bottom of the plate instead of a fully fixed connection. The stiffness of this spring was found by using the frequency of the unexpected mode (Figure 7.4) and the mass of the test setup. This method computes the dry natural frequencies better than the FEM model with the clamped base. It can also be seen that the effect of the end mass and added mass on the natural frequencies is approximated well by the FEM model as the reduction in frequencies for different depths is similar for the FEM model and the experiment.

Table 7.2 shows that the frequencies are significantly influenced by the end mass, and to a lesser extent by the submersion depth. An increase in submersion depth leads to an increase in added mass, which in turn leads to a decrease in natural frequency. This will be discussed further in Section 7.4.2.

To check whether the length of the side plates influenced the measured natural frequencies, after draining the tank, dry tests were done for all positions of the side plates. Since there was no added mass present, the natural frequencies should be the same in all positions. The results from these tests are shown in Appendix A. The standard deviation between the results for different depths were in the same range as the standard deviations between the three measurements used for the decay tests at each depth. This means that the side plate length did not have a significant influence on the natural frequencies at each depth.

7.2 Comparison experiment and ComFlow

In this section the results from the experiment are compared with the results from ComFlow. First, a comparison of the wave propagation is made. Next, the computed forces from the two-dimensional and three-dimensional simulations are compared. Lastly, the computed pressures are compared with the pressures from the experiment, to get an impression on the accuracy of the force distribution from the ComFlow studies.

7.2.1 Wave propagation

In the experiment the plates are loaded by an impact from a focused wave. During the experiment the wave is measured at two points; 4.8 and 1.8 meters in front of the structure. The signal measured at 4.8

meters is used as input in ComFlow to numerically simulate the rest of the experiment. This wave signal is taken from an unobstructed run, so without the experimental setup present. Figure 7.1a shows the wave height measured by the front wave gauge, and the resulting wave height computed by ComFlow when using the front wave gauge input.

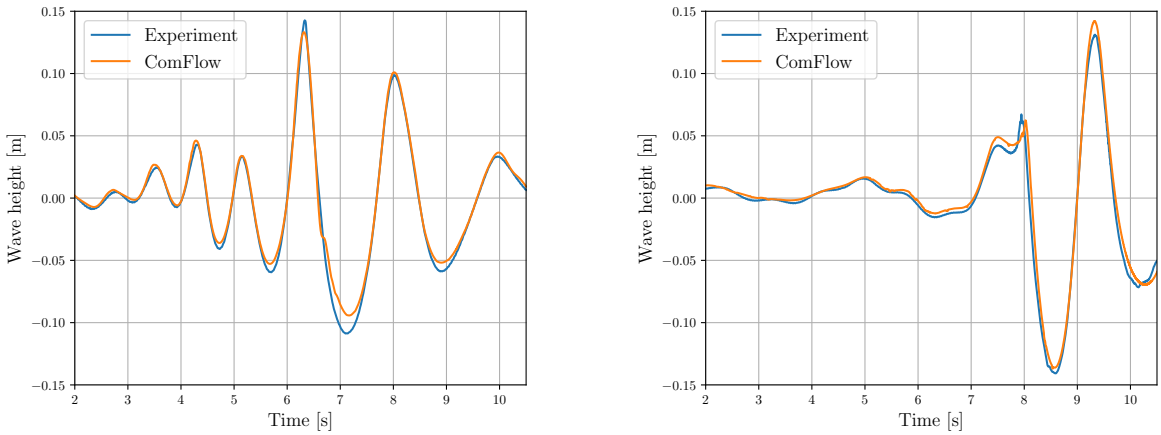

(a) *Front wave gauge* **(b)** *Rear wave gauge*

Fig. 7.1 *Comparison of wave propagation between experiment and numerical ComFlow simulations for the undisturbed propagating wave.*

It can be seen that the signal is not perfectly represented by ComFlow. This has multiple reasons. Firstly, the signal measured is turned into an FFT of which the components are then turned back into a signal by ComFlow. Since the FFT assumes linear waves, some information is lost in this transformation. Then as ComFlow translates these linear components back into a nonlinear wave signal another error is introduced. Additionally, it was found that the ComFlow simulation became unstable for wave components with frequencies above 2.5 Hz, which put a limit to the number of components that could be used as input to ComFlow. This mainly influences the peaks of the waveheight. Figure 7.1b shows the comparison between the signal at the rear wave gauge (at 3 m distance of the front wave gauge). It can be seen that there is a good match between the wave height computed by ComFlow and the wave height in the experiment. Since this wave gauge is close to the plate, a good match here is more relevant than a good match at the input.

7.2.2 Comparison force on rigid structures

For all plate submersion ratios ComFlow simulations were done using the input described above. The computed force on the plate from these simulations are compared with the results of the rigid plate experiments. Figure 7.2 shows the force measured in the experiments in blue and the force as computed by ComFlow in orange (2D) and black (3D).

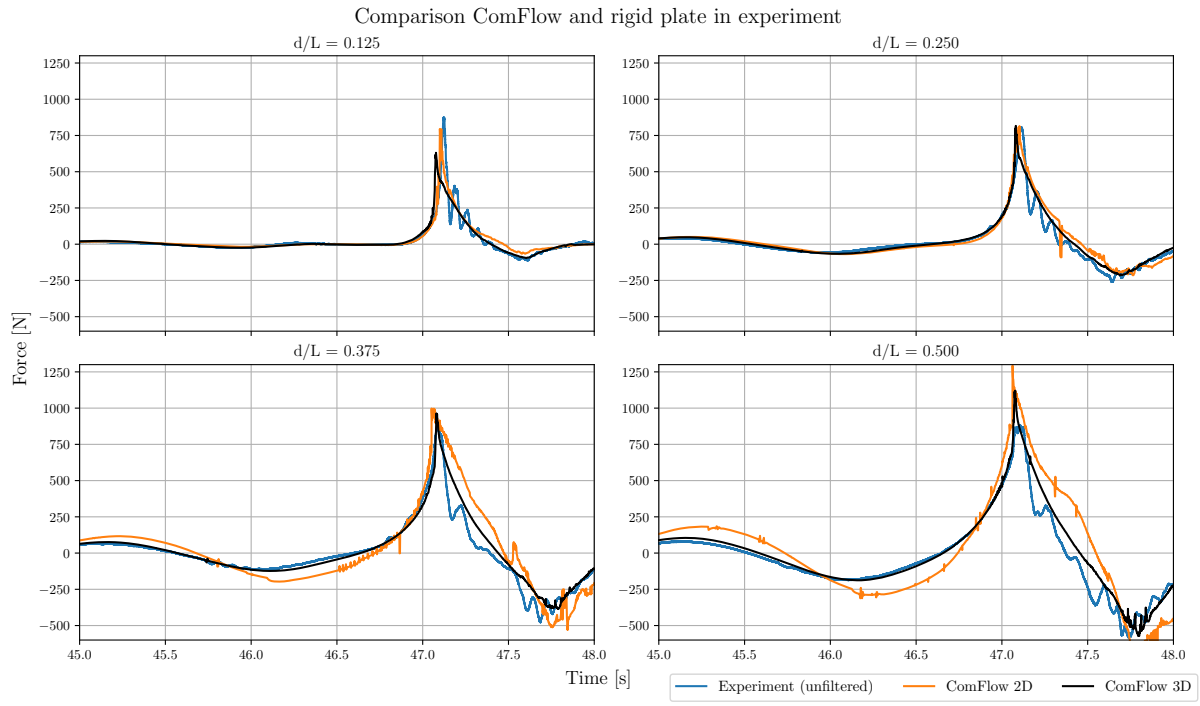

Fig. 7.2 *Comparison between the force measured on the rigid plates in the experiment and the force as computed by ComFlow.*

As seen in Figure 7.2, how well the simulations and experiments agree varies a lot between the different depths. These errors are due to an inaccurate computation of the wave action behind the structure. In the experiment there is wave flow around the sides of the plate, which will then also flow sideways to fill the space behind the plate. This water at the back of the plate creates a counter-force, affecting the force measured on the plate. Since the simulation is two-dimensional, with the plate covering the full width, the only possible flow around the structure is underneath. For deeper plate submersion this flow is obstructed more which causes the error to increase. The black line in Figure 7.2 shows that the 3D simulations are a great improvement to the 2D simulations, which confirms the error is (partly) caused by an incorrect flow at the back of the plate.

7.2.3 Comparison pressure on rigid structures

Figure 7.3 shows the comparison between pressures measured in the experiment and the pressures computed by ComFlow. The measurements and simulations show good agreement at all locations. The largest error with the experiments was 0.3 kPa, for the other 2 locations it was less than 0.1 kPa. The force distribution from ComFlow is used to compute the numerical results in Section 7.5. The deviation in the PCB measurements at location P1 is likely due to a misplacement of the sensor, since this sensor gave large differences compared to the PDCR in all runs, while at the other locations the sensors give the same output.

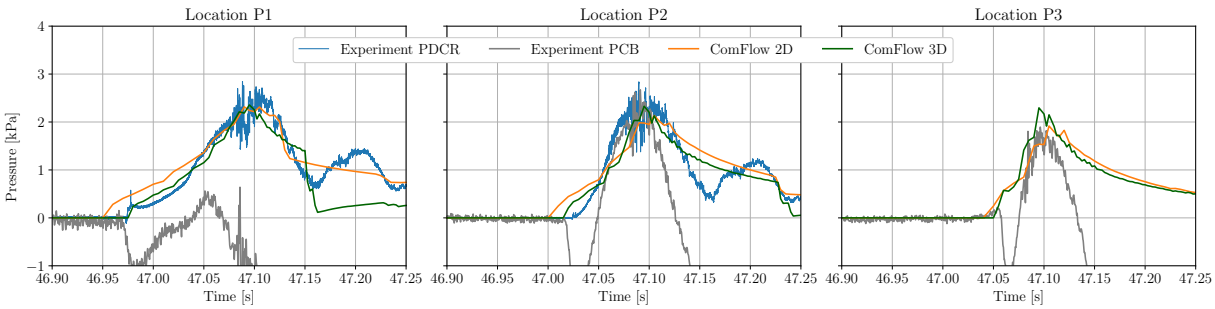

Fig. 7.3 *Pressure comparison between ComFlow and experiment.*

7.3 Filtering of results

As seen in Figure 7.2 in the previous section, there is an oscillation in the force signal from the experiment. These results are for the rigid plate, which means that the natural frequencies of the plate are too high to explain this oscillation. For a fixed-fixed plate with these dimensions the natural frequency is expected around 82 Hz [26], when ignoring the vertical stiffeners which raise the natural frequency further. Impact tests were performed on the rigid plate setup (without water) to determine the frequency of this interfering mode. The frequencies of this mode can be seen around 22-23 Hz and at double this frequency in Figure 7.4.

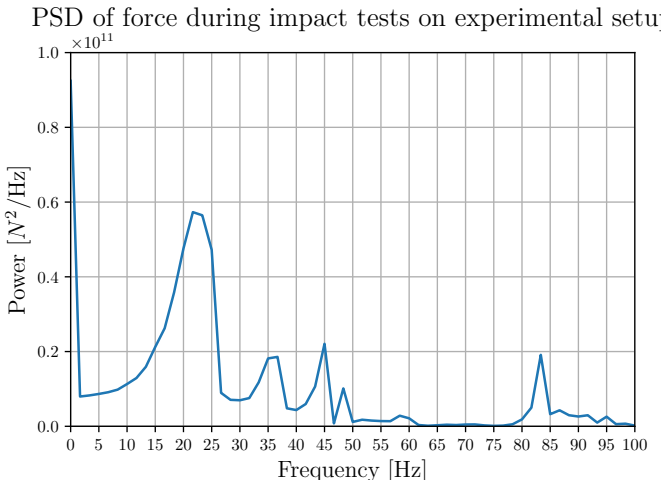

Fig. 7.4 *FFT of the dry impact test on rigid plate setup. The interfering mode can be seen around 22-23 Hz, as well as at double this frequency around 45 Hz.*

Figure 7.5 show FFTs of the rigid plate impact at all submersion ratios. The frequencies related to the interfering mode are shown using the grey mask. As seen in this figure, the frequencies decrease with an increase in submersion ratio, this is the result of the increase in added mass. As a larger part of the test setup is submerged, more water surrounds the test setup, increasing the added mass and decreasing the natural frequencies of all modes, including this interfering mode. It is also visible that the contribution of this mode decreases as the amplitude relative to the amplitudes of the peak frequencies is lower. It is expected that this is the result of the mode being damped more strongly by the water surrounding the test setup at larger submersion ratios.

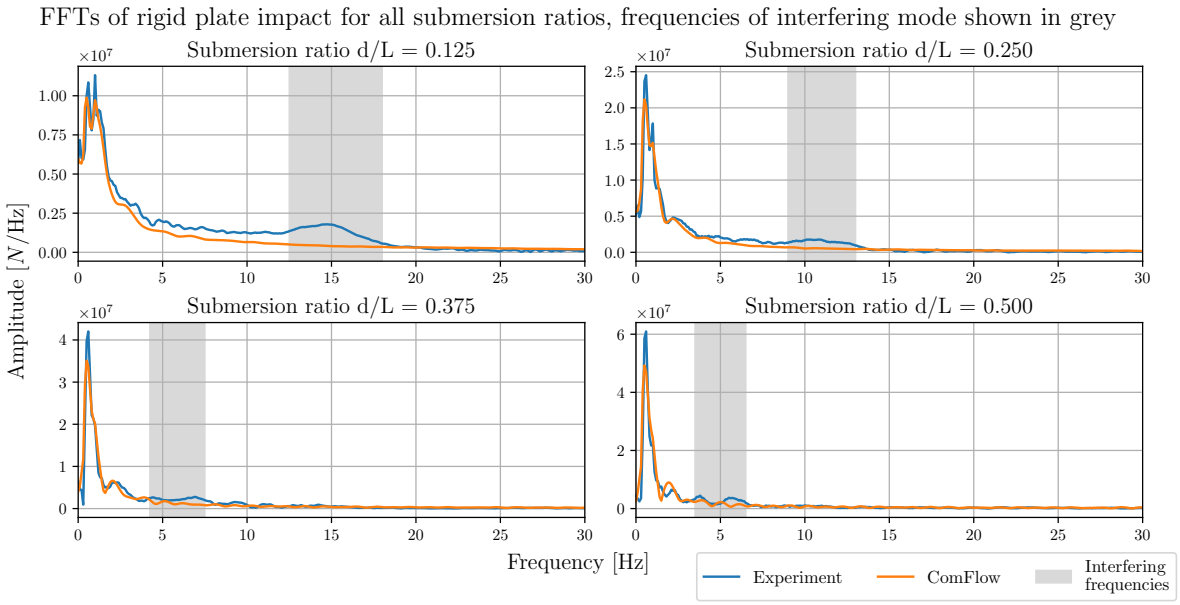

Fig. 7.5 *FFTs showing the frequencies of the disrupting mode in the rigid plate tests. This frequency is lower for the more submerged plates due to the increased added mass around the structure.*

To minimize the effect of this interfering mode several filtering techniques were tried. The best results were achieved by setting the magnitudes of all components in the FFT above 5 Hz to 0 and then reconstructing the signal. As seen in Table 7.3, the total impulse changes by only about 1% as a result of this filtering. This impulse value has been computed by integrating the force over time between the zero-crossing at the start of the impact and the first zero-crossing after the peak force. From here on the results will be presented as resulting from both the unfiltered dataset and the results which have been filtered using this method.

Table 7.3 *The influence of filtering on total impulse for different tests at 0.250 submersion ratio.*

Mass ratio	Impulse unfiltered [Ns]	Impulse filtered [Ns]	Difference [%]
0	142.01	142.30	-0.20
0.2	142.31	140.78	1.08
0.5	143.89	142.75	0.79
1	146.43	145.22	0.83
1.5	147.55	146.12	0.97

In Figure 7.6 an example of an unfiltered and filtered signal is given. The corresponding FFTs of both signals is also shown. As seen in the FFT of the filtered signal, all components above 5 Hz have been set to 0 which removes influence of the interfering mode.

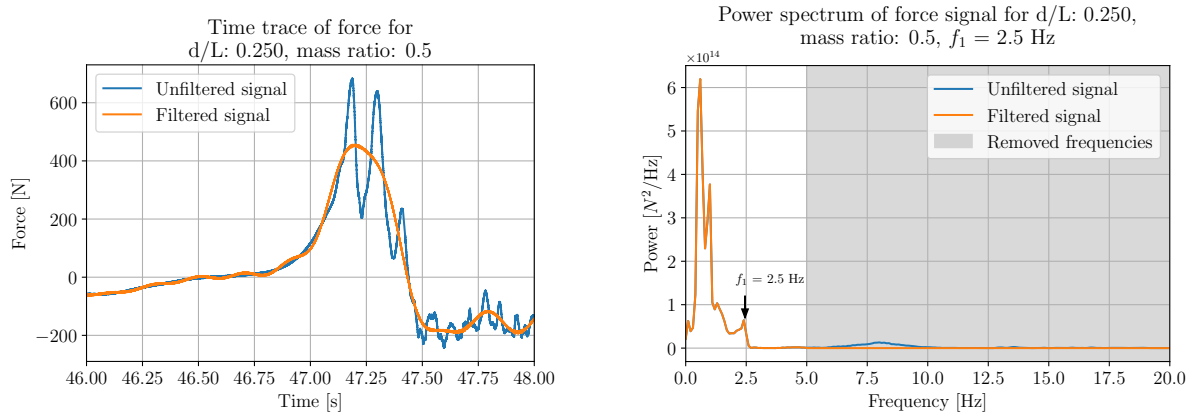

(a) *Force time series of the unfiltered and filtered signal.*

(b) *FFT of unfiltered and filtered signal.*

Fig. 7.6 *The effect of the filtering. The removal of the disrupting frequencies can clearly be seen in both the force time series and the FFTs.*

7.4 Effect structural properties on hydroelasticity

In this section, the experimental results for the tests with the flexible plate are presented. First, the influence of the end mass is analysed, followed by the effect of the added mass. Lastly, the influence of the first and higher modes on hydroelasticity is discussed. This section shows the results filtered using the explained strategy, the unfiltered results can be found in Appendix A.

7.4.1 Effect of end mass

Increasing the end mass reduces the natural frequency of the system and increases the inertia of the end of the plate. Hydroelasticity is expressed as the ratio between the peak force measured on the flexible plate and the peak force measured on the rigid plate. The effect of the end mass is shown in Figure 7.7. The coloured lines show different submersion depths, which are given as the submersion depth (d) divided by the length of the plate (L).

The data shows a decrease of the force ratio for an increase in mass ratio, which corresponds to a decrease in natural frequency. The results for the systems with the heaviest end-masses (lowest frequency) do not follow this trend. It is possible that for lower frequencies the effect of hydroelasticity decreases again. However, it is also likely that this deviation from the trend is caused by the filtering. For these systems, the frequency of the interfering mode is close to the cutoff frequency of 5 Hz, which means some disruption might still be left in the signal which increases the maximum force values. A lower cutoff would interfere with the first natural frequencies of the flexible plates without end-mass and could therefore not be used.

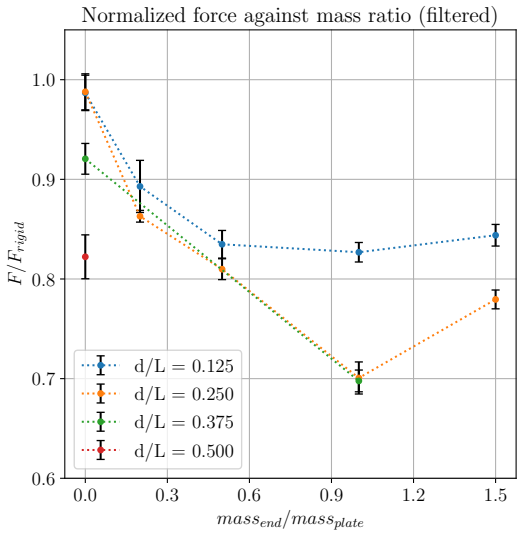

(a) *End mass effect as function of mass ratio.*

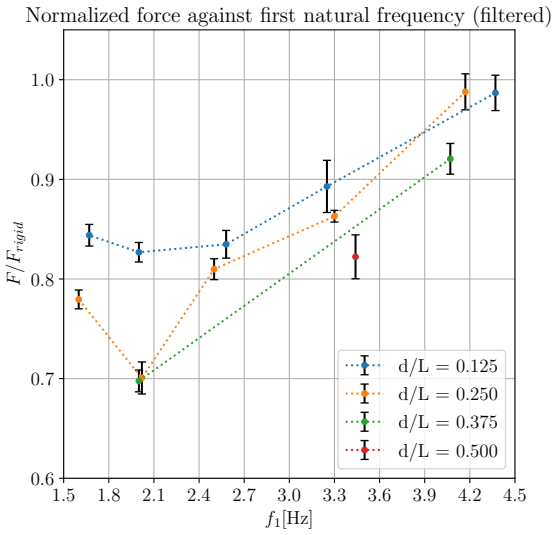

(b) *End mass effect as function of frequency.*

Fig. 7.7 *The effect of end mass on hydroelasticity from the filtered results for different submersion depths.*

As seen in Figure 7.5, the main information of the impact is concentrated between 0 and 2.5 Hz. As the natural frequency of the structure gets closer to these frequencies the first mode is activated more strongly, and the role of hydroelasticity increases, which is visible in the reduction of the force ratio. The trends seen in the data corresponds to previous studies on hydroelasticity of uniform structures such as studies by Bereznitski [4] and Faltinsen [28], which also found an increase in hydroelasticity for situations where the loading period and first natural period are closer.

Figure 7.8 shows the results plotted against the normalized first natural period of each structure. The period is normalized by dividing the impact duration (zero-crossing to zero-crossing of the force) on the rigid plate by the first natural frequency of the flexible model. This is the same approach as used by Bereznitski [4]. A clear difference can be seen between the smallest submersion ratio and the rest. As seen in Figure 7.2 the impact for this case is much shorter which shifts all the points to the left in this graph. It was also observed in the experiment that the front of the plate is almost completely dry just before impact opposed to the other depths for which a part of the plate always remains in the water. It is expected that these differences in loading conditions cause the shift to the left for the data points corresponding to d/L = 0.125.

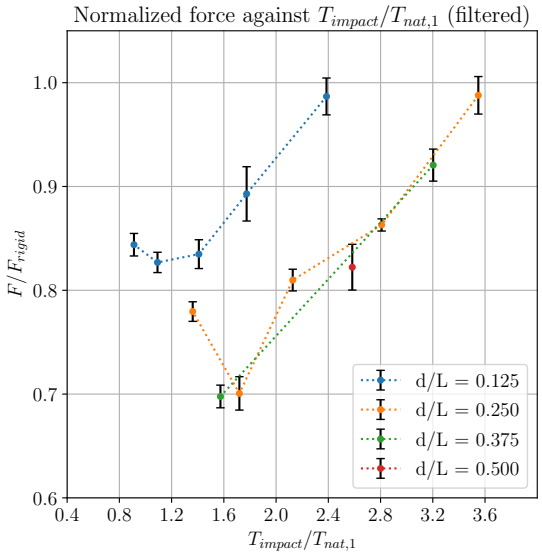

Fig. 7.8 *End mass effect expressed as normalized force against normalized period for different submersion depths.*

As seen in Table 7.3, the total impulse in this period is almost the same for all structures. When analyzing the loading period, it is found that the period of loading increases for the structures with lower natural frequencies. This means that the load gets distributed over a larger loading period, which reduces the peak force.

7.4.2 Effect of added mass

Increasing the submersion depth increases the added mass acting on the system, which brings the natural period closer to the loading period. The load also slightly changes, this is corrected for by measuring the rigid force for each submersion depth. The effect of the increase in added mass is seen in Figure 7.9. When plotted against the submersion depth, as shown in Figure 7.9a, an increase in hydroelasticity for larger submersion depths can be seen. However, when plotted against the first natural frequency (Figure 7.9b) no clear trend is visible for most data points.

The results show that, except for the smallest submersion depth, the variation in depth does not lead to a significant change in natural frequency (which is also seen in the computations of the natural frequencies by the FEM model in Section 7.1). This indicates that there is only a small increase in added mass for larger submersion depths. For the smallest submersion, the data shows that an increase in added mass leads to a decrease in natural period in turn resulting in an increase in hydroelastic effects, visible in the reduction of the force ratio.

The data shows that although the submersion depth has a significant influence on hydroelasticity, it is not caused by added mass. It is possible that it is caused by the point of application of the force. For larger depths, the force acts higher on the plate, which causes a larger response. Since hydroelasticity is strongly coupled to structural response, it is expected that a stronger structural response leads to larger hydroelastic effects.

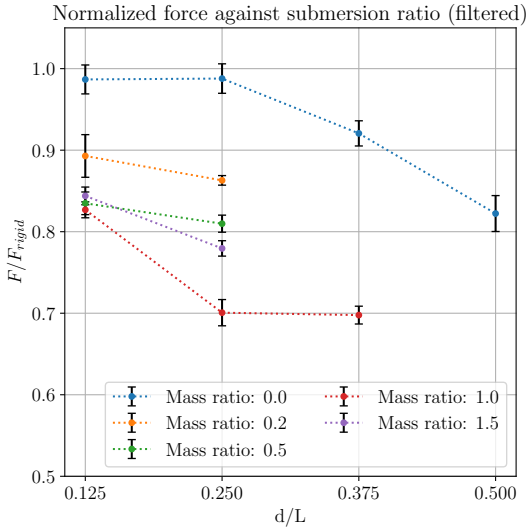

(a) *The effect of added mass plotted as function of depth.*

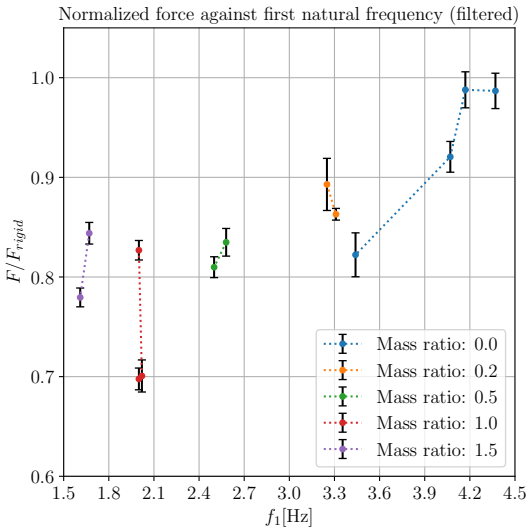

(b) *The effect of added mass plotted as function of frequency.*

Fig. 7.9 *The effect of added mass on hydroelasticity.*

For larger submersion depths, a larger part of the plate is in the water, which leads to more reflection. Part of this is accounted for by the reference force on the rigid plate, which has been determined for each depth separately. Additionally, the mean wave profiles for the rigid tests show that except for d/L = 0.5, the wave profile is not affected significantly by this reflection. This can be seen in Appendix A.

7.4.3 Effect of structural modes

First natural frequency

Most research on the effect of structural properties on hydroelasticity focuses on the first natural frequency, such as Bereznitski [4] and Faltinsen [28]. As illustrated in Section 1, it was expected that for non-uniform systems this trend could be different. Figure 7.7 shows that based on the results from the experiments in this thesis, the first natural frequency is still a clear indicator for the occurrence of hydroelasticity in non-uniform systems if the loading conditions are the same.

Nevertheless, the added mass results show that when the loading conditions change, for example a higher point of contact of the force on the plate, systems with almost the same natural frequencies can have a different force ratio, for example at the points around $f_1 = 2$ Hz in Figure 7.9b. This shows that for more complex systems, solely relying on first natural frequency to express the importance of hydroelasticity will be inaccurate.

Effect of higher modes

A structural response in the second mode was only seen for a limited number of test configurations. Third modes or higher were not seen for any test. Figure 7.10 shows the power spectra taken for all mass ratios at d/L 0.25 with the range of first and second natural frequencies highlighted.

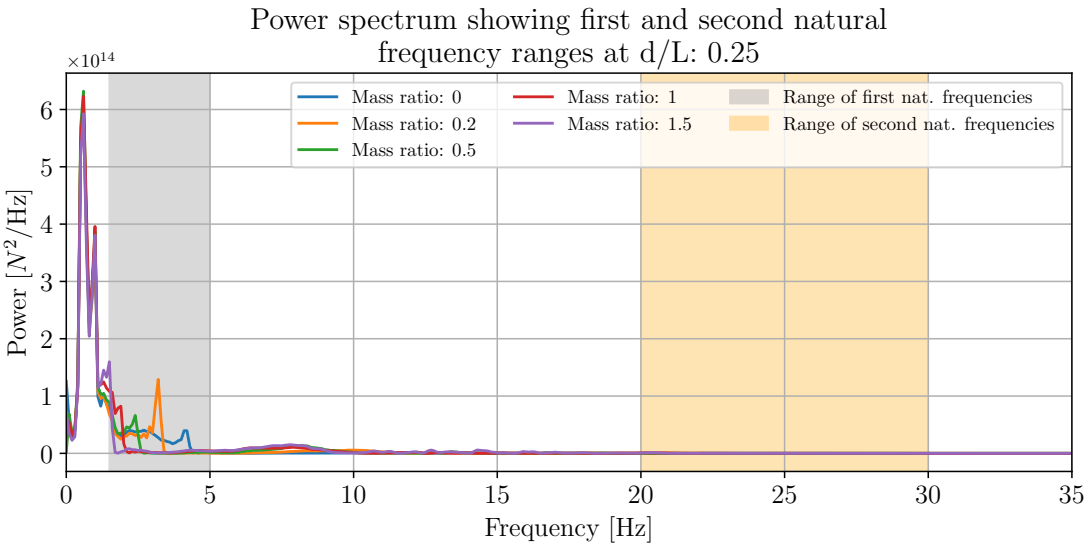

Fig. 7.10 *Power spectra of force measurements for all models at d/L = 0.25. No peaks in the expected range of second natural frequencies are visible.*

As visible in Figure 7.10, for none of these configurations a peak is visible in the range where the second natural frequency is expected, indicating that the contribution of the second mode to the response was small.

For some configurations, a second mode response was seen, such as for d/L 0.125, mass ratio 0.5. Using the FEM model, the second mode was computed to be at 24.3 Hz. In the FFT of the force measurement, a peak is seen around 22 Hz. Since all frequencies in the experiment were lower than those computed by FEM (as seen in Table 7.2), this was assumed to be the second mode. This area is highlighted in yellow in Figure 7.11a.

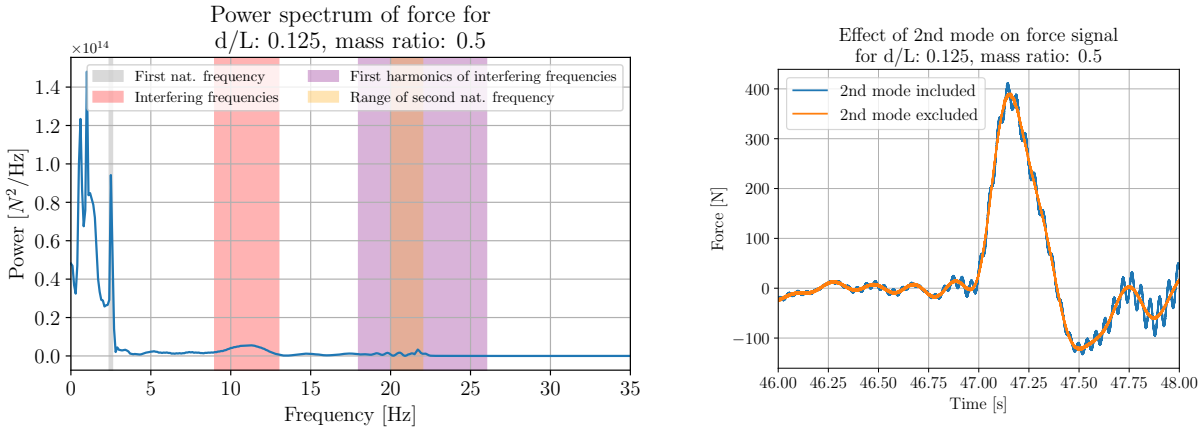

(a) *Power spectrum indicating first and second frequency and interfering mode.*

(b) *Force with and without frequencies around second mode.*

Fig. 7.11 *Effect of frequency around second mode on force as seen in experimental results. It is uncertain whether these frequencies are indeed the second mode or harmonics of the interfering mode.*

To study the influence of higher modes, the filtering approach explained before was followed, but the

frequencies around the expected second mode are not set to 0. Next, the effect on the force time trace is assessed, to get an estimate of the contribution of the second mode. As seen in Figure 7.11b, the effect of these frequencies is small.

Additionally, a downside of this method is that the harmonics of the interfering mode in the test setup (which acts between 9 and 13 Hz in this configuration) also have an effect in this area. This makes it impossible to determine whether any effect is caused by the second mode or by the interfering mode in the test setup. This overlap in frequencies is illustrated with the highlighted area in Figure 7.11a.

7.5 Comparison quasi-static predictions and experiment

So far, hydroelasticity has been expressed as the reduction of the peak forces. It is also possible to express hydroelasticity as the reduction in response compared to a quasi-static approach. In the absence of hydroelasticity, a quasi-static approach should give accurate results for the response. An example of previous research addressing hydroelasticity in this way is the study by Bereznitski [4]. The same approach will be followed here.

The quasi-static response has been computed by using the force distribution from the ComFlow simulations (this is the force on a rigid plate) as input for the FEM model. The FEM model includes the spring boundary condition at the bottom as explained in Section 7.1. The values from the experiments and the values calculated using the FEM model are shown in Figure 7.12.

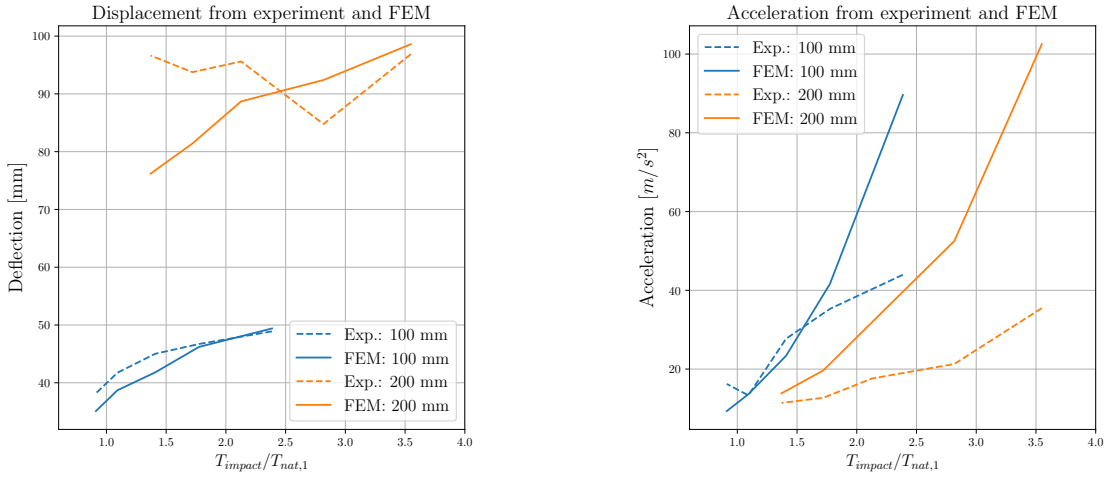

(a) *Maximum deflection from experiment and FEM.* **(b)** *Maximum acceleration from experiment and FEM.*

Fig. 7.12 *Experimental values compared with results from FEM model.*

The difference between the quasi-static solution (w for deflection, a for acceleration) and the experiment is expressed by:

$$\Delta_{w,exp/FEM} = 100\% \cdot \frac{w_{FEM} - w_{experiment}}{w_{FEM}} \qquad \Delta_{a,exp/FEM} = 100\% \cdot \frac{a_{FEM} - a_{experiment}}{a_{FEM}} \tag{7.1}$$

These errors are plotted against $T_{impact}/T_{nat,1}$, which is the ratio of the impact duration for the rigid plate over the first natural period of each structure. This is shown in Figure 7.13.

The results show that the response of systems with a natural period closer to the loading period of the wave, is predicted less accurately than the response of structures with a larger ratio between the periods. This matches the findings in a previous study by Bereznitski [4]. However, while Bereznitski found that the quasi-static method overestimated the results, the results presented here show an underestimation of response.

In the experiment, at d/L = 0.25, there was no clear trend between maximum deflection and mass ratio. In the FEM model, the heavier models have lower deflection than the lighter models. This results in an increase in error towards lower period ratios (these are the models with heavier end mass). At d/L = 0.125 in the experiment, there was a downward trend for maximum deflection as the mass increased. As seen in the results, the error with FEM is much smaller for this situation. For acceleration, at both submersion ratios, the experiment and FEM show a downward trend in maximum acceleration with increased end mass. Here, the absolute error decreases with heavier end mass, as FEM overestimates the maximum acceleration at low mass ratios, possibly due to an underestimation of damping. The relative error increases for d/L = 0.125 and decreases for 0.25.

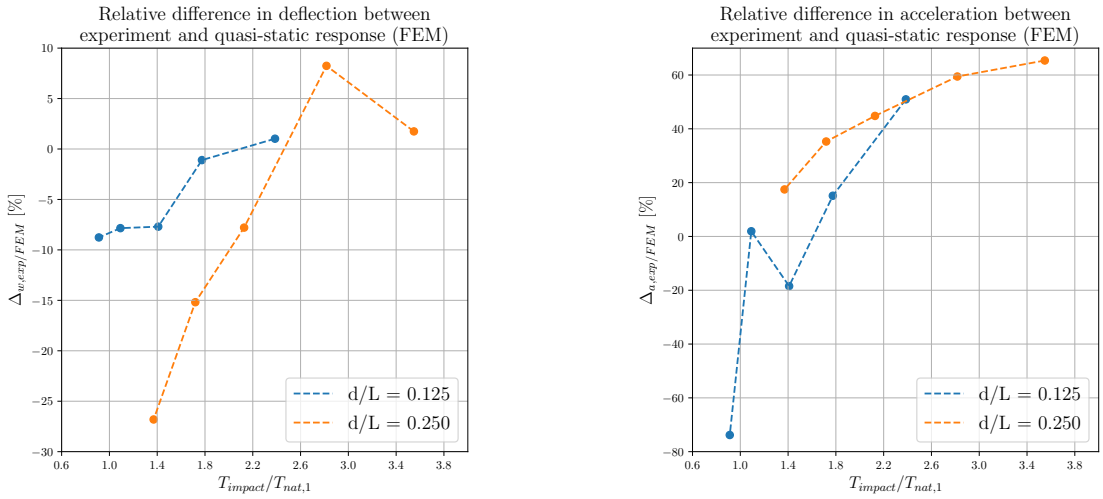

(a) *Deflection comparison.*

(b) *Acceleration comparison.*

Fig. 7.13 *Comparison between quasi-static one-way coupled results and experimental results.*

The difference with the results from Bereznitski could be explained by the difference in testing conditions. Firstly, Berenznitski looked at uniform beams which made impact with still water, where as in this thesis non-uniform plates were impacted by a breaking wave. Additionally, in the results presented here the deflection and acceleration are measured at the top of the beam (where no impact takes place) whereas in Bereznitski's study the deformation is measured at the point of impact.

It is important to note that the FEM model only has limited validation, which means the differences could also be caused by other effects. Since the FEM model is not validated for non-hydroelastic situations, it is not possible to be sure what fraction of these errors is caused by hydroelasticity. For example, it could be possible that the model underestimates the response for heavier systems (lower frequencies) in general, and that this causes the difference. To be more certain about the accuracy of the FEM model, more validation tests without hydroelasticity present should be performed. These tests would determine whether the found differences are caused by hydroelasticity or by errors in the FEM model.

8 Conclusions

This section summarizes the most important conclusions formed in this thesis. The section starts with answers to the sub-research questions and ends with the main conclusion of the research in this thesis.

RQ 1: What is the effect of the end-mass on hydroelasticity?
Peak impact forces on models with varying end masses were compared against the peak impact force on a rigid model under the same loading condition. This variation was done at multiple submersion ratios for the base of the model. An increase in end mass lowers the natural frequency of the model, which brings the natural period closer to the duration of the impact.

As the ratio between the periods approaches 1.0, the peak force on these models was reduced. At submersion ratio 0.25, a decrease in the ratio between periods from 3.6 to 1.7, resulted in the ratio between the force measured on the flexible and rigid plates dropping by nearly 30%, with a similar drop seen for submersion ratio d/L = 0.375. This effect was smaller at submersion ratio 0.125, with a drop of 15% with a decrease from a ratio of 2.4 to 1.1.

RQ 2: What is the effect of added mass on hydroelasticity?
To study the effect of added mass on hydroelasticity, the model was submerged for ratios of its length between 0.125 and 0.5. An increase in submersion depth leads to an increase in added mass. This additional added mass leads to a reduction in the natural frequency, although this effect was small for most models in this experiment. Since the submersion depth also influences the load, a reference force using the rigid model was determined at each depth.

It was found that for most models, the effect of the increase in added mass was small relative to the mass of the model. As a result, the effect of added mass on the natural frequency was insignificant for these models.

For the models with an end mass ratio of 0, a clear change in natural frequencies for different submersion depths was seen. As the first natural period approached the loading period, the peak impact forces were reduced. Between submersion ratio 0.125 and 0.5, the ratio between the force on the flexible and rigid plate reduced by 16%. It was found that the effect of added mass is the same as the effect of end mass; as the natural period gets closer to the loading period the reduction in peak forces relative to a rigid system increases.

Additionally, although the natural frequency of the other configurations did not vary considerably for different submersion depths, there was still a significant difference in peak force ratios. For all mass ratios, a reduction in peak force ratio was seen between submersion ratio 0.125 and 0.25. Differences in reduction ranged from 3% for mass ratio 0.2 to 12% for mass ratio 1.5. It is expected that this difference was due to the higher point of application of the force, which results in a stronger response from the model and therefore a larger reduction of peak forces.

RQ 3: How do the first and higher natural frequencies of non-uniform systems influence hydroelasticity?
All test configurations were characterized by the ratio of the first natural period and loading duration. Then the ratio between the peak force on the rigid and flexible plate was compared, and analyzed against this period ratio. It was seen that there is a strong correlation between the match of the periods, and

the reduction in peak forces, with the peak force lowest for models where the ratio between the periods was close to 1.0.

However, for models with almost the same ratio of periods, a large difference in peak force reduction could be seen, especially in the added mass variations. This shows that for more complex systems, expressing the role of hydroelasticity in an impact event only as a function of the first natural frequency is inaccurate.

In the experiment conducted in this thesis, the response of the models was dominated by the first mode. A response around the second frequency was only seen for a limited number of configurations. For these configurations, it was not possible to determine whether this was a second mode response or harmonics from an interfering mode in the test setup. It was therefore not possible to determine the effect of higher structural modes on hydroelasticity in this study.

RQ 4: How does the response in a hydroelastic impact event differ from the response computed using a one-way coupled model?
The force on the rigid structure was computed using computational fluid dynamics simulations in ComFlow. This simulated force had an error in peak force of 17% for 0.125 submersion ratio, and 1.12% for submersion ratio of 0.25. The impact durations had errors of 0.73% and 2.8%. The force distribution was used in a one-way coupled finite element method model to compute the expected quasi-static response. This response was then compared against the response measured in the experiment to determine the differences between the quasi-static approach and the hydroelastic impact situation.

The comparison showed that the FEM model underestimated the maximum deflection at the top of the plate for most test cases. The error between the FEM model and the experiment was larger for models with a period ratio closer to 1.0. For submersion ratio 0.125, the error increased from 1% to -9%, while for ratio 0.25, the error increased from +2% to -27%. The FEM model overestimated the maximum acceleration at the top of the plate for the models at submersion ratio d/L = 0.25, ranging from +65% to +19%. At d/L = 0.125, the model error ranged from +50% for high period ratios to -75% for period ratios below 1.0.

Main conclusion
The main research question in this thesis was: *What is the effect of added mass and end-mass on the hydroelastic behaviour of non-uniform systems, such as Offshore Wind Turbines, under breaking wave impact?* This study found that both increasing non-uniformity by an increase in end mass and added mass increase hydroelasticity by bringing the ratio between the first natural period and the loading period closer to 1.0. In this study, this effect was much larger for the end mass than for the added mass.

A reduction of 30% was seen in the peak force during impact for models with higher end mass. For the models without end-mass, an increase in submersion ratio from 0.125 to 0.5 led to a relative reduction of peak forces of approximately 16%. Additionally, it was found that for models where the natural frequencies did not change significantly, an increase in submersion ratio from 0.125 to 0.5 led to a further reduction of peak forces of 12%.

The results in this thesis show that the characteristic non-uniformities of offshore wind turbines, namely the end-mass and submersion depth, significantly influence the hydroelastic behavior of such structures during breaking wave impacts.

9 Future Work

Based on the obtained conclusions and experiences gained during this thesis, some recommendations for future work can be made. The most important ones are listed and explained below.

Firstly, it would be interesting to design a similar experiment with larger variations in added mass to obtain a more definitive answer on the influence of this property on hydroelasticity. In the current experiment, the variation of added mass was small, which meant limited data was available to draw conclusions from. It was also seen that submersion depth influenced hydroelasticity without affecting the first natural frequency much. This is an interesting effect to investigate further, as it can lead to more insight into the influence of non-uniform loading on hydroelasticity.

The results from this thesis agree with hydroelastic theories for uniform systems when looking at peak forces, but disagree when looking at structural response. It would be interesting to further look into the effect of hydroelasticity on structural response. A start was made during this thesis, but the model used to compute the quasi-static response lacks validation to be entirely certain of the conclusions. This would require better validation using a loading situation without hydroelasticity. Knowing the accuracy of the model in such a situation makes it possible to get a better estimate of the influence of hydroelasticity on structural response.

The research in this thesis was focused on two-dimensional models. One of the steps to bring the research closer to reality is through three-dimensional modeling and experiments. It is important to study whether the conclusions for (uniform) hydroelastic theories also hold for three-dimensional situations. Like the variation of added mass and end mass in this thesis, adding extra degrees of freedom will introduce complexities that might not be captured properly in the current uniform hydroelastic theories.

The results in this thesis could not give a conclusive answer on the effect of higher modes on hydroelasticity. It is possible that for situations in which the higher modes are excited more, the differences between uniform and non-uniform systems are larger, since some non-uniformities have a large influence on these higher modes. Conducting experiments with systems for which these higher modes are more relevant could create new insights into the coupling between structural response and loading, which is central to hydroelasticity.

For future experimental setups used to investigate hydroelasticity in impact events, even more attention should be given to preventing a response of the experimental setup at undesired frequencies. Doing impact tests or similar studies on the experimental setup beforehand could help identify such undesired modes and prevent them before testing starts.

During this thesis, extensive use was made of CFD and FEM models. Finding more efficient ways to couple these two types of models can play a large role in the improved modeling of hydroelasticity. Both methods have shown to be successful at their respective goals, so combining them allows studying hydroelasticity with less dependency on experimental setups.

Besides fully-coupled CFD-FEM models, it is also interesting to further study lower fidelity models. For example, a FEM model as used in this thesis with a lower-fidelity method to compute the slamming force which takes structural response into account. A model such as this would be much faster than a fully coupled CFD-FEM model, and can therefore be useful in a preliminary design phase.

References

[1] Walter Musial et al. *Offshore Wind Market Report: 2023 Edition.* Tech. rep. U.S Department of Energy, 2023.

[2] Xiaoni Wu et al. "Foundations of offshore wind turbines: A review". In: *Renewable and Sustainable Energy Reviews* 104 (Apr. 2019), pp. 379–393. ISSN: 18790690. DOI: 10.1016/j.rser.2019.01.012.

[3] Tyler Stehly, Patrick Duffy, and Daniel Mulas Hernando. *2022 Cost of Wind Energy Review.* 2023.

[4] A Bereznitski. "Slamming: the role of hydroelasticity". In: *Int. Shipbuild. Progr* 48 (4 2001), pp. 333–351.

[5] Bryson Robertson et al. "Breaking waves". In: *Coastal Engineering Journal* 55 (1 2013). ISSN: 17936292. DOI: 10.1142/S0578563413500022.

[6] J. Wienke and H. Oumeraci. "Breaking wave impact force on a vertical and inclined slender pile - Theoretical and large-scale model investigations". In: *Coastal Engineering* 52 (5 May 2005), pp. 435–462. ISSN: 03783839. DOI: 10.1016/j.coastaleng.2004.12.008.

[7] R. W. Bos and P. R. Wellens. "Fluid structure interaction between a pendulum and focused breaking waves". In: *Physics of Fluids* 33 (6 June 2021). ISSN: 10897666. DOI: 10.1063/5.0054426.

[8] Bas Hofland, Miroslaw Lech Kaminski, and Guido Wolters. *Large scale wave impacts on a vertical wall.* 2010.

[9] Ying Tu, Zhengshun Cheng, and Michael Muskulus. "A review of slamming load application to offshore wind turbines from an integrated perspective". In: *Energy Procedia.* Vol. 137. Elsevier Ltd, 2017, pp. 346–357. DOI: 10.1016/j.egypro.2017.10.359.

[10] Bo Terp Paulsen et al. "Probability of wave slamming and the magnitude of slamming loads on offshore wind turbine foundations". In: *Coastal Engineering* 143 (Jan. 2019), pp. 76–95. ISSN: 03783839. DOI: 10.1016/j.coastaleng.2018.10.002.

[11] Erik Jan de Ridder et al. *The dynamic response of an offshore wind turbine with realistic flexibility to breaking wave impact.* 2011. DOI: https://doi.org/10.1115/OMAE2011-49563.

[12] Qian Wang, Yongliu Fang, and Hua Liu. "An experimental study of run-up and loads on a vertical truncated cylinder in a solitary wave". In: *Ocean Engineering* 219 (Jan. 2021). ISSN: 00298018. DOI: 10.1016/j.oceaneng.2020.108346.

[13] Ankit Aggarwal et al. "Characteristics of breaking irregular wave forces on a monopile". In: *Applied Ocean Research* 90 (Sept. 2019). ISSN: 01411187. DOI: 10.1016/j.apor.2019.06.003.

[14] Paul Renaud et al. "Semi-analytical load models describing the progressive immersion of a fixed vertical cylinder in a breaking wave". In: *Ocean Engineering* 276 (May 2023). ISSN: 00298018. DOI: 10.1016/j.oceaneng.2023.114116.

[15] Y Goda, S Haranaka, and M Kitahata. "Study of impulsive breaking wave forces on piles." In: *Rep. Port Harbor Res. Inst.* (1966), pp. 1–30.

[16] H Wagner. "Über Stoss- und Gleitvorgange an der Oberfläche von Flüssigkeiten". In: *Z. Angew. Math. Mech.* (1932), pp. 193–215.

[17] M A Lackner, D P Schmidt, and S R Arwade. *Simulating breaking waves and estimating loads on offshore wind turbines using computational fluid dynamic models*. 2018.

[18] T Von Karman. *The Impact of Seaplane Floats during Landing*. 1929.

[19] Xinmeng Zeng et al. "Nonlinear hydrodynamics of floating offshore wind turbines: A review". In: *Renewable and Sustainable Energy Reviews* 191 (Mar. 2024). ISSN: 18790690. DOI: 10.1016/j.rser.2023.114092.

[20] Pandeli Temarel. "hydroelasticity of Ships: Taking stock and moving forward". In: *22nd Asian-Pacific Technical Exchange and Advisory Meeting on Marine Structures (TEAM 2008) (06/10/08 - 09/10/08)*. 2008. URL: https://eprints.soton.ac.uk/64777/.

[21] T. Mai et al. "hydroelasticity effects on water-structure impacts". In: *Experiments in Fluids* 61 (9 Sept. 2020). ISSN: 14321114. DOI: 10.1007/s00348-020-03024-3.

[22] Jan Tore H. Horn, Jorgen R. Krokstad, and Jorgen Amdahl. "hydroelastic Contributions to Fatigue Damage on a Large Monopile". In: *Energy Procedia*. Vol. 94. Elsevier Ltd, 2016, pp. 102–114. DOI: 10.1016/j.egypro.2016.09.203.

[23] Hemant Sagar et al. *Hydroelasticity Effects of Wave Induced Loads on Offshore Monopile Structure*. 2015. URL: https://www.researchgate.net/publication/281965126.

[24] Michael Thome, Ould el Moctar, and Thomas E. Schellin. "Assessment of Hydrodynamic Loads on an Offshore Monopile Structure Considering hydroelasticity Effects". In: *Journal of Marine Science and Engineering* 11 (2 Feb. 2023). ISSN: 20771312. DOI: 10.3390/jmse11020350.

[25] Zilong Ti, Yanfeng Wang, and Yubing Song. "Frequency-domain approach of hydroelastic response for offshore bottom-mounted slender structure". In: *Ships and Offshore Structures* 18 (8 2023), pp. 1159–1170. ISSN: 17445302. DOI: 10.1080/17445302.2022.2109351.

[26] Robert D. Blevins. *Formulas for Dynamics, Acoustics and Vibration*. John Wiley & Sons, Ltd, Nov. 2015. ISBN: 9781119038122. DOI: 10.1002/9781119038122.

[27] B. Yang. "THEORY OF VIBRATION | Fundamentals". In: *Encyclopedia of Vibration*. Ed. by S. Braun. Oxford: Elsevier, 2001, pp. 1290–1299. ISBN: 978-0-12-227085-7. DOI: https://doi.org/10.1006/rwvb.2001.0112.

[28] Odd M Faltinsen. "Water Entry of a Wedge by Hydroelastic Orthotropic Plate Theory". In: *Journal of Ship Research* 43 (3 1999), pp. 180–193. DOI: https://doi.org/10.5957/jsr.1999.43.3.180.

[29] I Stenius et al. *Hydroelastic Effects in Slamming Loaded Panels*. 2011. URL: https://www.researchgate.net/publication/267556342.

[30] Miroslaw Lech Kaminski, Hannes Bogaert, and Mirek Kaminski. *hydroelastic Criterion for Practical Design*. 2007. URL: https://www.researchgate.net/publication/266606022.

[31] R. W. Bos et al. "A reduced order model for FSI of tank walls subject to wave impacts during sloshing". In: *International Shipbuilding Progress* 69 (2 Dec. 2022), pp. 119–138. ISSN: 15662829. DOI: 10.3233/ISP-220003.

[32] T. Allen and M. Battley. "Quantification of hydroelasticity in water impacts of flexible composite hull panels". In: *Ocean Engineering* 100 (May 2015), pp. 117–125. ISSN: 00298018. DOI: 10.1016/j.oceaneng.2015.04.012.

[33] Odd M Faltinsen. "Slamming". In: *Encyclopedia of Maritime and Offshore Engineering* (2017), pp. 1–12. DOI: 10.1002/9781118476406.emoe041.

[34] Tim Bunnik, Joop Helder, and Erik-Jan De Ridder. *Deterministic simulation of breaking wave impact and flexible response of a fixed offshore wind turbine*. 2015. DOI: https://doi.org/10.1115/OMAE2015-41989.

[35] Erik Jan de Ridder et al. *Summary of the joint industry project wave impact on fixed foundations (wifi jip)*. 2017. DOI: https://doi.org/10.1115/OMAE2017-62040.

[36] Loup Suja-Thauvin et al. "Experimental results of a multimode monopile offshore wind turbine support structure subjected to steep and breaking irregular waves". In: *Ocean Engineering* 146 (Dec. 2017), pp. 339–351. ISSN: 00298018. DOI: 10.1016/j.oceaneng.2017.09.024.

[37] A. Korobkin, R. Guéret, and Š Malenica. "Hydroelastic coupling of beam finite element model with Wagner theory of water impact". In: *Journal of Fluids and Structures* 22 (4 May 2006), pp. 493–504. ISSN: 08899746. DOI: 10.1016/j.jfluidstructs.2006.01.001.

[38] Hang Xie et al. "Numerical and experimental study on hydroelasticity in water-entry problem of a composite ship-hull structure". In: *Composite Structures* 201 (Oct. 2018), pp. 942–957. ISSN: 02638223. DOI: 10.1016/j.compstruct.2018.06.030.

[39] R. Panciroli et al. "hydroelasticity in water-entry problems: Comparison between experimental and SPH results". In: *Composite Structures* 94 (2 Jan. 2012), pp. 532–539. ISSN: 02638223. DOI: 10.1016/j.compstruct.2011.08.016.

[40] Odd M Faltinsen, Jan Kvalsvold, and Jan V Aarsnes. "Wave impact on a horizontal elastic plate". In: *Journal of Marine Science and Technology* 2 (1997), pp. 87–100.

[41] Marin. *ComFlow User Group*. URL: https://www.marin.nl/en/jips/networks/comflow-user-group (visited on 02/11/2025).

[42] K.M.T Kleefsman et al. "A Volume-of-Fluid based simulation method for wave impact problems". In: *Journal of Computational Physics* (2005). DOI: https://doi:10.1016/j.jcp.2004.12.007.

[43] P. van der Plas. *ComFlow Program documentation*. 2018. URL: https://poseidon.housing.rug.nl/sphinx/index_documentation.html (visited on 02/06/2025).

[44] Klaus-Jurgen Bathe. *Finite Element Procedures*. Prentice-Hall, 1996. ISBN: 0133014584.

[45] Orcina. *OrcaWave Documentation*. 2024. URL: https://www.orcina.com/webhelp/OrcaWave/ (visited on 12/19/2024).

[46] Christophe Geuzaine and Jean-Francois Remacle. "Gmsh: a three-dimensional finite element mesh generator with built-in pre- and post-processing facilities". In: *International Journal for numerical methods in engineering* (2009). DOI: https://doi.org/10.1002/nme.2579.

[47] Abdollah Malekjafarian et al. "Foundation damping for monopile supported offshore wind turbines: A review". In: *Marine Structures* 77 (2021). ISSN: 0951-8339. DOI: https://doi.org/10.1016/j.marstruc.2021.102937.

[48] W. E. Cummins. *The Impulse Response Function and Ship Motions*. Tech. rep. Department of the Navy, David Taylor Model Basin, 1962.

[49] Orcina. *Vessel theory: impulse response and convolution.* 2025. URL: https://www.orcina.com/webhelp/OrcaFlex/Content/html/Vesseltheory,Impulseresponseandconvolution.html (visited on 02/12/2025).

[50] Ernst Hairer and Gerhard Wanner. "Radau Methods". In: *Encyclopedia of Applied and Computational Mathematics* (2015), pp. 1213–1216. DOI: https://doi.org/10.1007/978-3-540-70529-1_139.

A Additional results

Influence reflection on wave profile

Figure A.1 shows the mean wave profile measured for different submersion depths. This mean is taken from all runs performed with the rigid plate at this depth. As seen in the figures, the wave is not affected by the plate submersion depth, except for submersion ratio d/L = 0.500, where a reduction in the wave height can be seen in Figure A.1b.

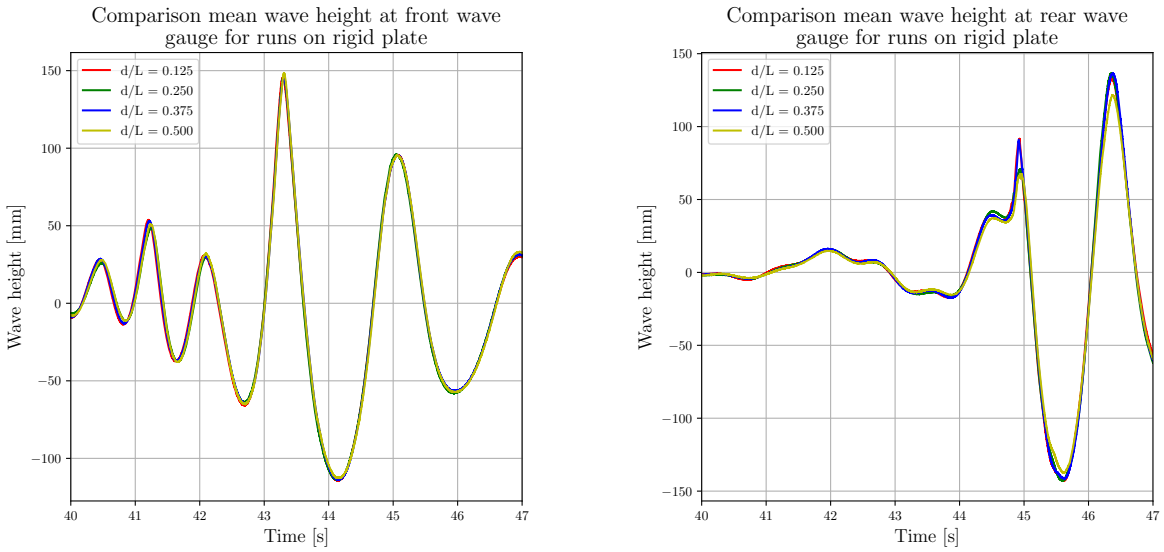

(a) *Comparison mean wave profiles at rear wave gauge.* **(b)** *Comparison mean wave profiles at rear wave gauge.*

Fig. A.1 *Effect of reflection on wave profiles*

Decay tests side plate influence

To determine the influence of the side plate length in the experimental setup, dry decay tests were performed using all configurations from the experiment. As seen in Table A.1, changing the length of the side plates does not significantly influence the natural frequencies measured.

Table A.1 *Results from decay tests performed to assess influence of sideplates.*

	End mass / plate mass				
d/L	0	0.2	0.5	1	1.5
0.125	4.19	3.16	2.44	1.94	1.65
0.250	4.2	3.15	2.46	1.93	1.6
0.375	4.22			1.93	
0.500	4.2			1.89	
Mean	4.2	3.16	2.45	1.92	1.63
STD	0.011	0.005	0.01	0.02	0.025

Force on support structure

As seen in Figure A.2, the force on the support structure is only around 30 N. This is 5% of the total force measured during the experiments.

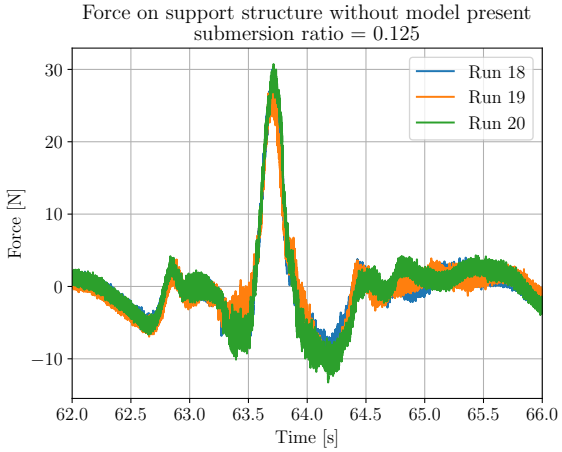

Fig. A.2 *Example time series of force on support structure without model connected.*

Unfiltered Results

End mass effect

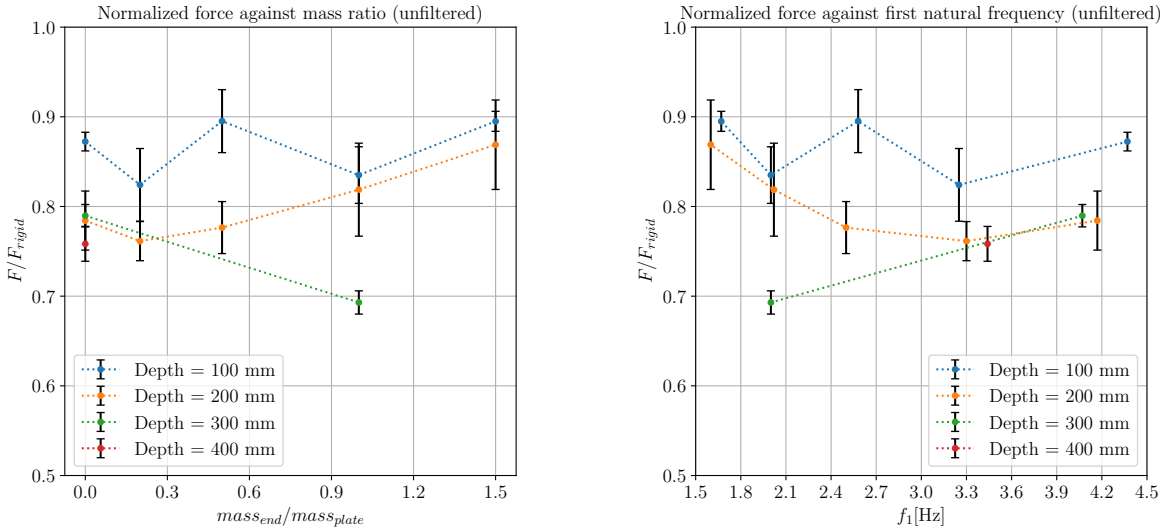

(a) *End mass effect as function of mass ratio.*

(b) *End mass effect as function of frequency.*

Fig. A.3 *The effect of end mass on hydroelasticity from the unfiltered results.*

Added mass effect

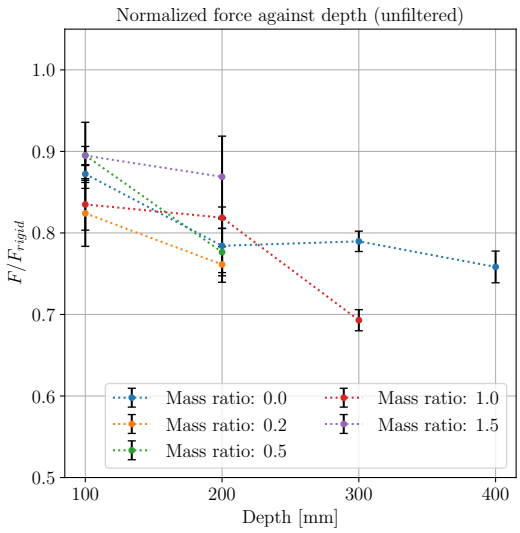

(a) *The effect of added mass plotted as function of depth.*

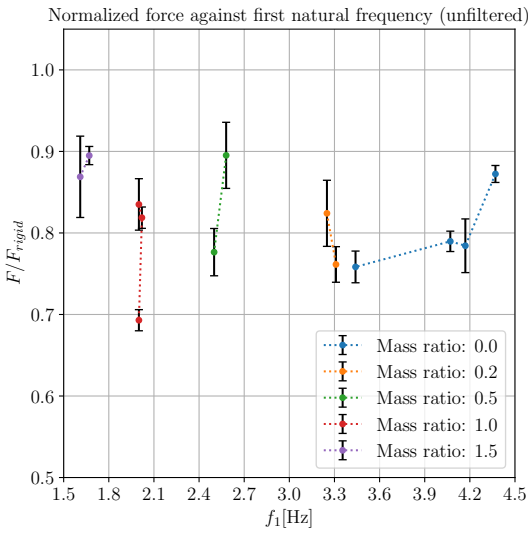

(b) *The effect of added mass plotted as function of frequency.*

Fig. A.4 *The effect of added mass on hydroelasticity from unfiltered results.*

B Convergence ComFlow simulations

Figure B.1 shows the time series of the 2D impact at submersion ratio 0.250, for different number of cells used in the domain discretization. As seen in the figure, the results do not converge to a solution for an increased number of cells. Figure B.1b shows that the peak force does not converge to a final value.

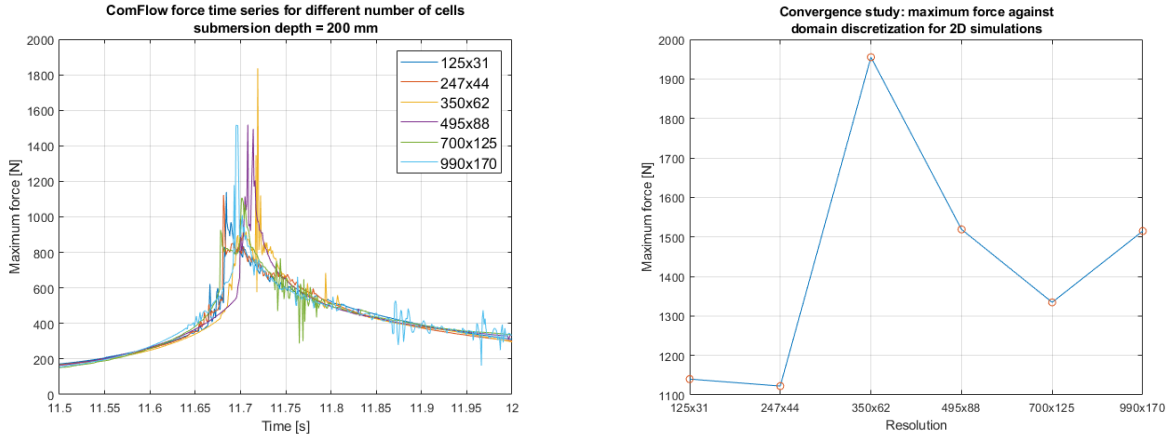

(a) *Force time series for different domain discretizations.* **(b)** *Convergence of maximum force for 2D simulations.*

Fig. B.1 *Convergence study on 2D ComFlow simulations.*

Figure B.2 shows the time series of the force for different domain discretizations in the 3D simulations. Although these results show better convergence than the 2D simulations, Figure B.2b shows that the maximum value does not show clear convergence yet.

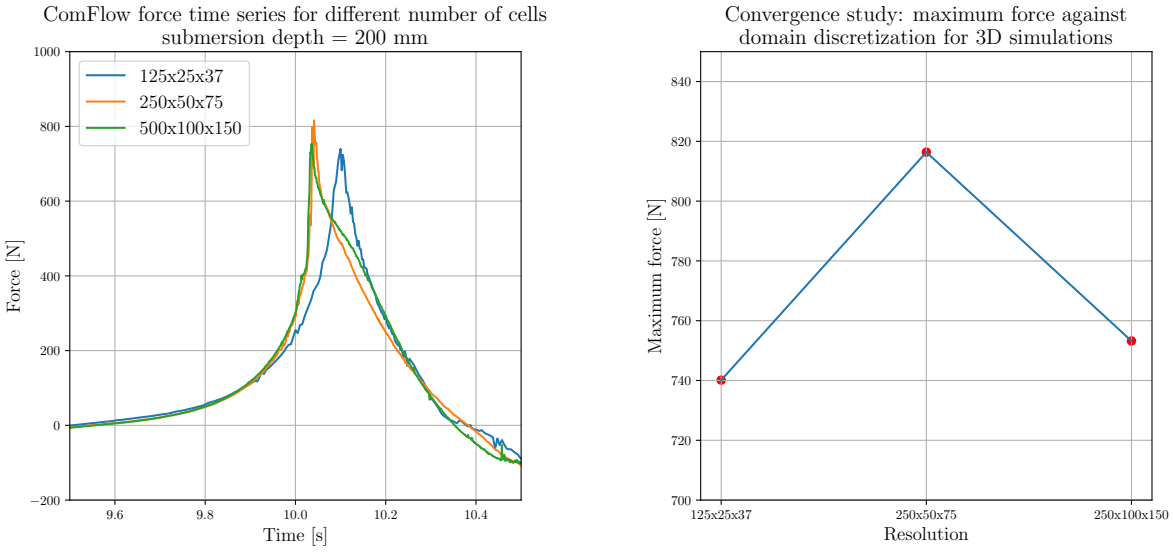

(a) *Comparison force time trace for different number of cells used to discretize the domain.* **(b)** *Convergence of maximum force for 3D simulations.*

Fig. B.2 *Convergence study on 3D ComFlow simulations.*

C Sensor calibration

Force sensors

F1

The residuals from the calibration were normalized by the voltage range in the calibration. The found calibration factor was: -494.43 N/V. The average normalized residual for force sensor 2 was: 0.18%.

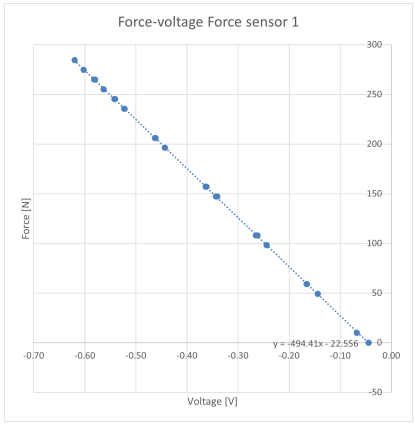

(a) *Force against voltage plot from calibration.*

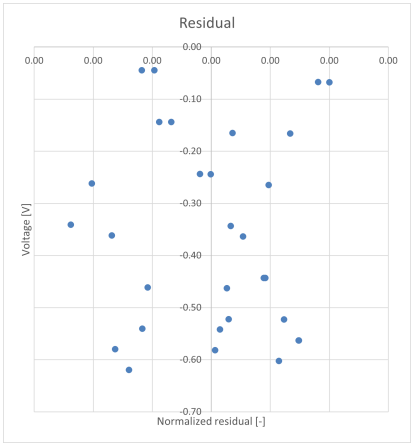

(b) *Normalized residual against voltage from calibration.*

Fig. C.1 *Calibration results of force sensor 1.*

F2

The residuals from the calibration were normalized by the voltage range in the calibration. The found calibration factor was: 492.44 N/V. The average normalized residual for force sensor 2 was: 0.101%

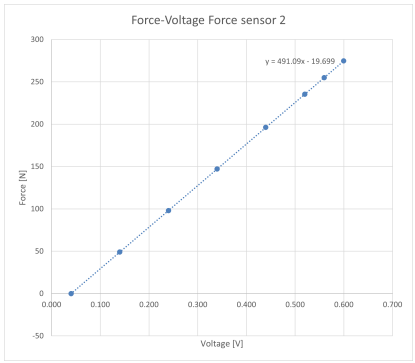

(a) *Force against voltage plot from calibration.*

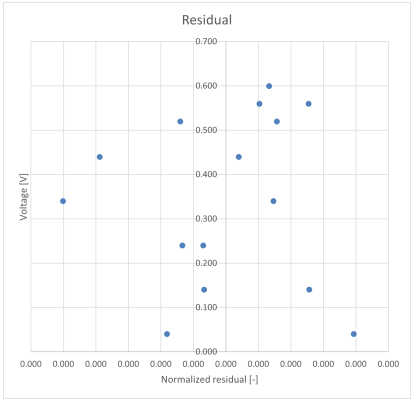

(b) *Normalized residual against voltage from calibration.*

Fig. C.2 *Calibration results of force sensor 2.*

Pressure

PDCR 1, ID204

The residuals from the calibration were normalized by the mV/V range in the calibration. The calibration factor was: 5.16 kPa/(mV/V). The average normalized residual for pressure sensor 1 was: 0.10%

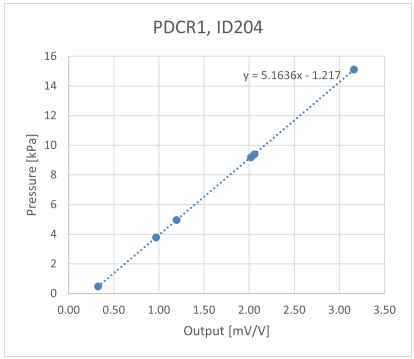

(a) *Pressure against mV/V plot from calibration.*

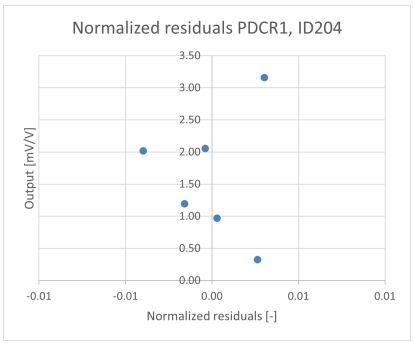

(b) *Normalized residual against mV/V from calibration.*

Fig. C.3 *Calibration results of PDCR 1.*

PDCR 2, ID208

The residuals from the calibration were normalized by the mV/V range in the calibration. The calibration factor was: 10.13 kPa/(mV/V). The average normalized residual for pressure sensor 2 was: 0.22%

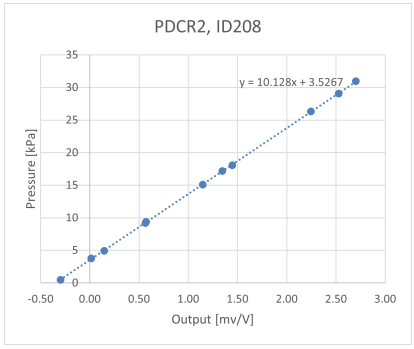

(a) *Pressure against mV/V plot from calibration.*

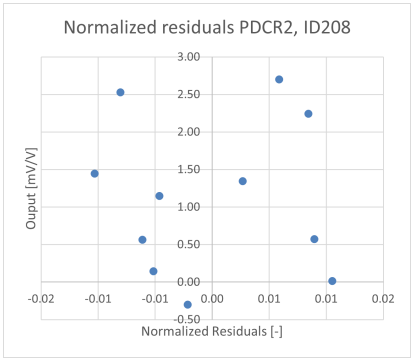

(b) *Normalized residual against mV/V from calibration.*

Fig. C.4 *Calibration results of PDCR 2.*

PCB sensors

The calibration of the PCB pressure sensors was performed by a fellow student who used the sensors in experiments the weeks before the experiments in this thesis. The found calibration factors and normalized residuals were:

- PCB1: 1.418 kPa/mV, normalized residuals: 0.025%
- PCB2: 1.386 kPa/mV, normalized residuals: 0.052%
- PCB3: 1.384 kPa/mV, normalized residuals: 0.055%

Laser sensors

Laser 1

The residuals from the calibration were normalized by the voltage range in the calibration. The found calibration factor was: -79.03 mm/V. The average normalized residual for laser sensor 1 was: 0.07%

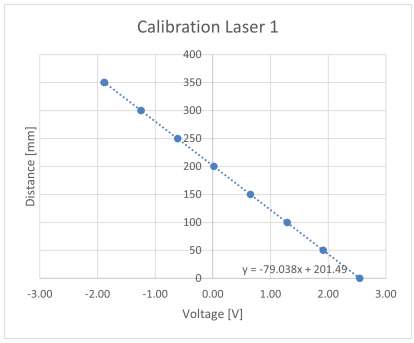

(a) *Distance against voltage plot from calibration.*

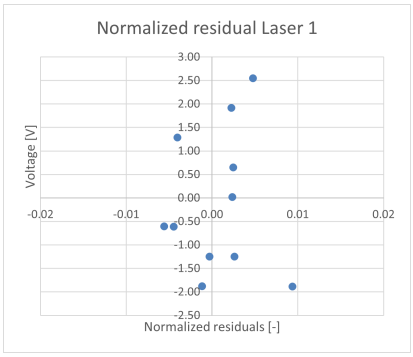

(b) *Normalized residual against voltage from calibration.*

Fig. C.5 *Calibration results of laser sensor 1.*

Laser 2

The residuals from the calibration were normalized by the voltage range in the calibration. The found calibration factor was: -79.14 mm/V. The average normalized residual for laser sensor 2 was: 0.08%

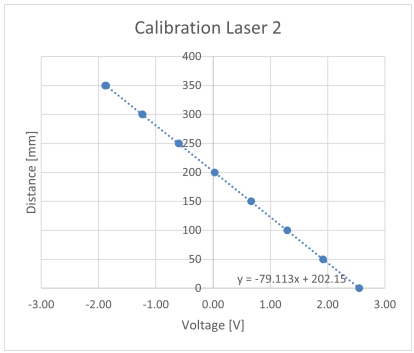

(a) *Distance against voltage plot from calibration.*

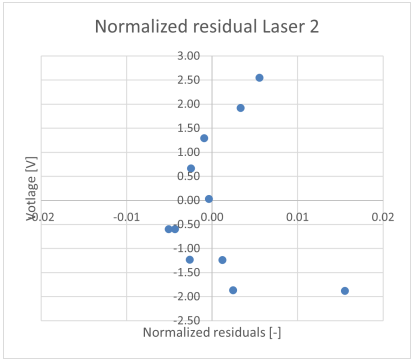

(b) *Normalized residual against voltage from calibration.*

Fig. C.6 *Calibration results of laser sensor 2.*

Laser 3

The residuals from the calibration were normalized by the voltage range in the calibration. The found calibration factor was: -80.97 mm/V. The average normalized residual for laser sensor 3 was: 0.08%

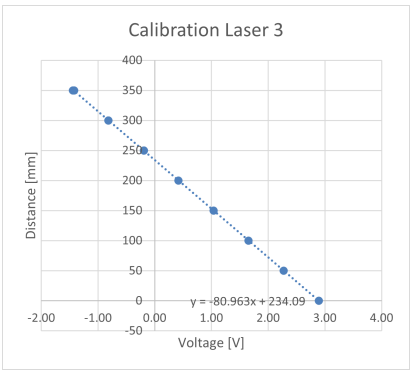

(a) *Distance against voltage plot from calibration.*

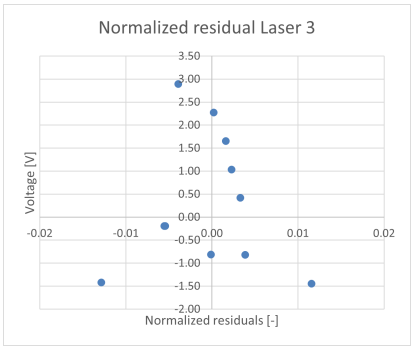

(b) *Normalized residual against voltage from calibration.*

Fig. C.7 *Calibration results of laser sensor 3.*

Wave gauges

The wave gauges were calibrated each morning of testing. Calibration consisted of changing the height electronically over a range of 400 mm with steps of 40 mm and then recording the voltage. This lead to slightly different calibration factors each day. The table below shows the calibration factor and normalized residual found for both wave gauges during each calibration. At 21/3 and 24/3 the rear wave gauge was broken, at 25/3 it was repaired but did not perform well, the important wave measurements were already done before these days.

Table C.1 *Performed calibrations for the wave gauges. At 21/3 and 21/4 the rear wave gauge was broken, it was repaired on 25/3 but did not perform well.*

	Front wave gauge		Rear wave gauge	
Date	Factor [mm/V]	Normalized residual [%]	Factor [mm/V]	Normalized residual [%]
14/3/25	33.56	0.24	20.38	1.47
17/3/25	33.61	0.25	19.94	1.06
18/3/25	33.56	0.24	20.10	1.74
19/3/25	33.44	0.23	20.28	1.70
20/3/25	33.45	0.26	20.05	1.44
21/3/25	33.10	0.35	-	-
24/3/25	32.92	0.25	-	-
25/3/25	32.90	0.25	23.84	9.36

Accelerometer

Calibration of the accelerometer was done by a student who used the accelerometer in the weeks before the experiments described in this thesis. This resulted in a calibration factor of 0.0246 $(m/s^2)/mV$ with a normalized residual of 0.3 %.

D Finite Element Model

This appendix expands on the information about the Finite Element Model already given in Section 5. It will explain the method used to assemble the added mass and damping matrix in the time domain analysis of the FEM model. Next, it will shortly explain the modal analysis method. This method was used to compute the end results in Section 7. Then it explains the numerical integration method used in the FEM model. Finally, it will show convergence studies done to assess the accuracy of choices made in the FEM model.

Convolution method for time domain analysis

To use the computed frequency depended added mass and damping in a time domain simulation a translation to the time domain should be made. This done using a method proposed by Cummins [48] and implemented following the method in [49]. The frequency dependent added mass and damping are included in the time domain using Equation D.1. This term is a force that accounts for the memory effects from the structure's previous motion in the water. In Equation D.1 the force is given as how it should be included in the right hand side of the global equation of motion, since the force opposes the motion of the structure.

$$\vec{f_h}(t) = -\mathbf{M}_a(\infty)\ddot{\vec{u}}(t) - \int_{\tau=0}^{\infty} \mathbf{IRF}(\tau)\dot{\vec{u}}(t-\tau)\,d\tau \tag{D.1}$$

Substitution of this term into the global EOM would lead to a global equation of motion as given in Equation D.2.

$$\mathbf{M}_{struc}\ddot{\vec{u}}(t) + \mathbf{B}_{struc}\dot{\vec{u}}(t) + \mathbf{K}\vec{u}(t) = \vec{q}(t) + \vec{f_h}(t) \tag{D.2}$$

In Equation D.1 $\mathbf{IRF}$ represents an impulse response function. This function can be determined using the frequency dependent damping matrix using Equation D.3. τ is a time lag variable. This variables denotes the difference in time between the current timestep and the timestep corresponding to a previous solution. Figure D.1 shows the relation between the IRF and the time lag variable for a specific element in the FEM model. Since each element has a specific frequency-dependent damping value, each element has its own IRF and therefore the dimensions of $\mathbf{IRF}$ are also 80x80. $\dot{\vec{u}}(t-\tau)$ is the velocity vector that corresponds to the solution at the previous timesteps.

$$\mathbf{IRF}(\tau) = c(\tau)\int_{f=0}^{\infty} 4\mathbf{B}(f)cos(2\pi f\tau)\,df \tag{D.3}$$

The term $c(\tau)$ is a cut-off scaling function used for numerical purposes and is given by Equation D.4. The integral in Equation D.7 needs to be evaluated for all previous values, which leads to slow computation times for long simulations. Impulse response functions decay to zero (as seen in Figure D.1) so larger values for τ can be discarded (when $\tau > T_c$). The cut-off scaling function prevents a sharp cut-off at T_c to prevent negative damping (which would lead to extra energy being added to the system) [49]. In this thesis a value of 7 seconds was used for T_c.

$$c(\tau) = exp\Big[-\Big(\frac{3\tau}{T_c}\Big)^2\Big] \tag{D.4}$$

The $\mathbf{IRF}$ function for a specific element for the case of a submersion of 0.4m can be found in Figure D.1. The decay to zero can clearly be seen.

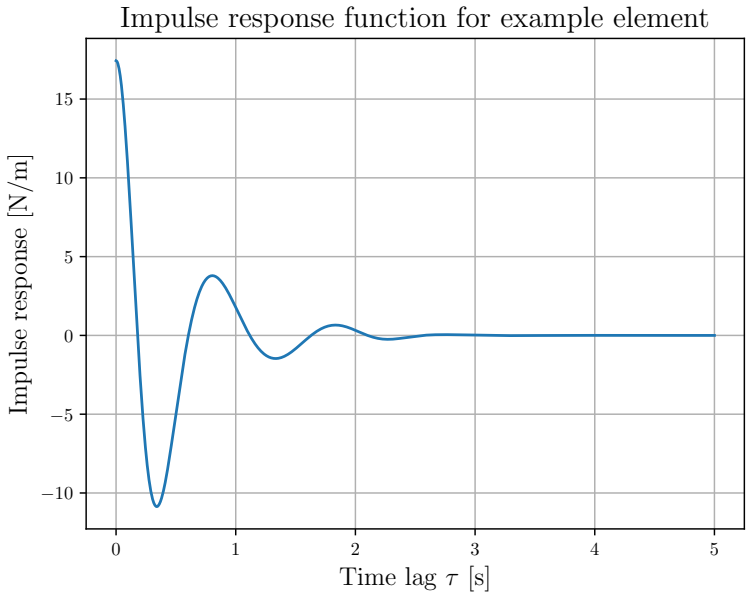

Fig. D.1 *The IRF function for the 5th element in the FEM model for a submersion depth of 0.2 m.*

The integral in Equation D.3 needs to be solved up to infinite frequency. In practice this is not possible, and also not necessary. Since the frequency dependent damping decays to zero for higher frequencies (this can be seen in Section 5.3) only a limited number of frequencies is needed. In this thesis 50 frequencies between 0 and 9 Hz are used, with smaller frequency steps in the region where there is more variation in damping and added mass.

The other part of Equation D.1 is the added mass value at $f = \infty$. This value can be approached using the assessed frequencies and Equation D.5.

$$\mathbf{M}_{a,i}(\infty) = \mathbf{M}_a(f_i) + \frac{1}{2\pi f_i} \int_{\tau=0}^{\infty} \mathbf{IRF}(\tau) sin(2\pi f_i \tau) d\tau \tag{D.5}$$

In this equation $M_{a,i}(\infty)$ denotes the estimate for the infinite frequency added mass made using each computed frequency f_i. This value should theoretically be the same whichever used frequency, but due to numerical errors this is often not true. The final estimate for $\mathbf{M}_a(\infty)$ is thus made by averaging over all these values. This follows the approach in [49].

$$\mathbf{M}_a(\infty) = \frac{1}{n} \sum_{i=1}^{n} \mathbf{M}_{a,i}(\infty) \tag{D.6}$$

Both the computed impulse response functions and the computed infinite frequency added mass have been verified by comparing with values computed using OrcaFlex.

Substituting the correction force from Equation D.1 in the equation of motion (Equation 5.3) and moving it to the left hand side gives the final equation of motion to be solved for in the time domain as seen in

Equation D.7.

$$\Big(\mathbf{M}_{struc} + \mathbf{M}_a(\infty)\Big)\ddot{\vec{u}}(t) + \mathbf{B}_{struc}\dot{\vec{u}}(t) + \int_{\tau=0}^{\infty} \mathbf{IRF}(\tau)\dot{\vec{u}}(t-\tau)\,d\tau + \mathbf{K}\vec{u}(t) = \vec{q}(t) \tag{D.7}$$

The integral in this equation should be solved for all values of τ up to infinity. However, since the impulse response functions tend to zero, this is not necessary. In this thesis integration was performed up to $\tau = T_c$ seconds. This improves computational performance while keeping enough accuracy.

Modal analysis

Another method to deal with the frequency dependent added mass and damping is to use modal analysis. As shortly explained in Section 1.3.1 modal analysis computes the response using a superposition of a chosen number of mode shapes (corresponding to the natural frequencies (modes) of the system). For each mode the values for the damping and added mass matrix are the values corresponding to the frequency of this mode. As a result, the equation of motion for modal analysis simplifies to Equation D.8.

$$\Big(\boldsymbol{M_{struc}} + \boldsymbol{M_a}\Big)\ddot{\boldsymbol{u}}(\boldsymbol{t}) + \Big(\boldsymbol{B_{struc}} + \boldsymbol{B_{hydro}}\Big)\dot{\boldsymbol{u}}(\boldsymbol{t}) + \boldsymbol{K}\boldsymbol{u}(\boldsymbol{t}) = \boldsymbol{Q}(\boldsymbol{t}) \tag{D.8}$$

$\mathbf{M}_a$ and $\mathbf{B}_{hydro}$ now are constant matrices containing the values at the used modes. This means the convolution integral in Equation D.7 does not need to be computed at each timestep, which makes modal analysis much faster. Additionally, each mode is represented by 1 value for the stiffness, mass and damping "matrix". As shown in the Section D using only a couple modes is enough to get accurate results. In this thesis results are computed using the first 5 modes. This greatly reduces the DOFs to solve since the number of DOFs is now equal to the number of modes.

Integration method

The EOM in Equation D.7 is solved by numerical integration. The procedure for this numerical integration is explain in this section.

First a vector q containing the values for u and $\dot{u}$ at the current timestep n is defined:

$$q_n = \begin{bmatrix} u_n \\ \dot{u}_n \end{bmatrix} \tag{D.9}$$

In the model a Radau integration scheme is followed. This is an implicit fifth order Runge-Kutta method [50]. The Radau method is suitable for stiff problems that have quickly varying values in the solution (for example high accelerations). The Radau scheme defines the solution for the following timestep as given in Equation D.10. This function is explained in more detail in Hairer and Wanner [50].

$$q_{n+1} = q_n + h\sum_{i=1}^{s} b_i f(t_n + c_i h, Y_{in}) = \begin{bmatrix} u_{n+1} \\ \dot{u}_{n+1} \end{bmatrix} \tag{D.10}$$

Equation 5.3 can be rewritten to a function which defines $\ddot{u}_n$ as a function of $\dot{u}_n$ and u_n. This is shown in Equation D.11. Using the Radau scheme, the solutions for $\dot{u}_{n+1}$ and u_{n+1} can be determined, after which the solution for $\ddot{u}_{n+1}$ can be determined using Equation D.11. The two mass matrices have been

combined in M and the memory term is denoted F_{IRF} for brevity.

$$\ddot{u}_n = \frac{1}{M}\Big(Q_n - F_{IRF,n} - B_{struc}\dot{u}_n - Ku_n\Big) \tag{D.11}$$

For each timestep n, F_{IRF} has to be computed again using the past values for $\dot{u}_n$ and τ.

For modal analysis the equation to be solved is much easier, as seen in Equation D.12. The two mass matrices and damping matrices have been combined in M and B respectively for brevity.

$$\ddot{u}_n = \frac{1}{M}\Big(Q_n - B\dot{u}_n - Ku_n\Big) \tag{D.12}$$

In the model the integrations are performed using the Initial Value Problem (IVP) solver from the Scipy package in Python.

Convergence studies FEM

The results from the FEM model were computed using modal analysis with the first 5 structural modes. Figure D.2 shows the convergence of the results for the number of modes used. It can be seen that when using 5 modes the model has converged.

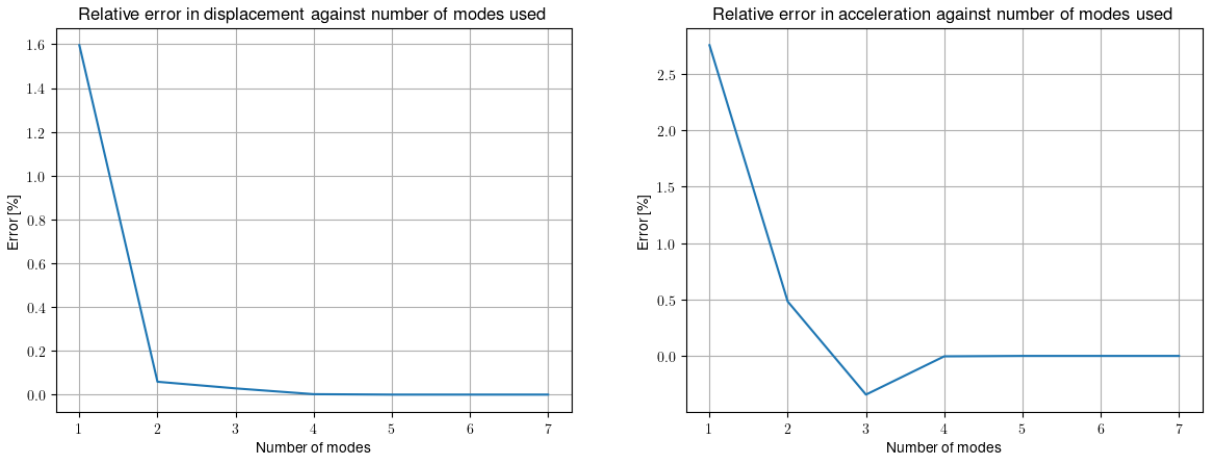

(a) *Displacement* **(b)** *Acceleration*

Fig. D.2 *Convergence of FEM results for number of modes used in modal analysis.*

The number of elements used in the FEM model also influences the results. Figure D.3 shows the convergence of the first 3 natural frequencies for the number of elements used. For the results in this thesis 40 elements were used, it can be seen that the results have converged for this number.

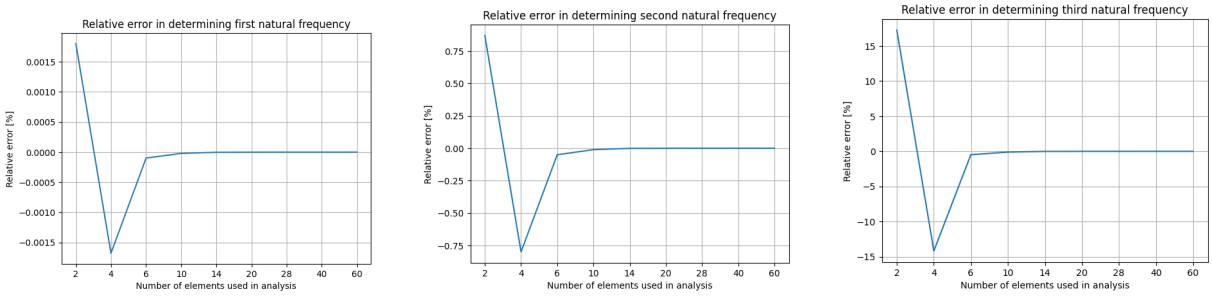

(a) *Convergence* f_1 **(b)** *Convergence* f_2 **(c)** *Convergence* f_3

Fig. D.3 *Convergence of FEM results for number of elements used in modal analysis.*

E Wave Focusing

Wave Focusing

To generate the breaking wave needed in the experiment a technique called wave focusing is used. The method applied in this thesis uses the principle of superposition to generate a wave at the focus location that is much higher and steeper than the individual components generated by the tank paddle. The wave components are focused at a specific location, which in the case of this experiment is just before the OWT model. This section explains the general concept of wave focusing.

A useful property of regular linear waves is that they follow the principle of superposition. This means that when combining multiple linear wave components, the resulting wave will simply be the sum of these components. Figure E.1 shows the principle of wave superposition in time using three components. The resulting superpositioned wave is shown using the black line in the bottom graph.

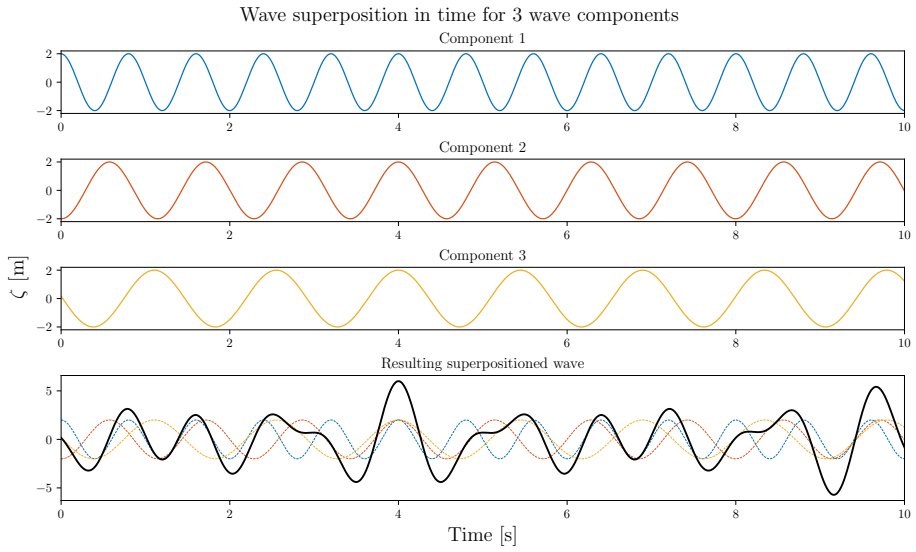

Fig. E.1 *Example of the superposition principle in time domain using three wave components. The bottom graph shows the components and the resulting wave (black) after superposition. A peak equal to the sum of the amplitudes of the components can be seen at $t = 4$ seconds.*

Figure E.1 shows that at certain points in time the peaks of the components align, which creates a peak equal to the sum of the component amplitudes. This can be seen around $t = 4$ seconds. Figure E.1 is a time trace of the waves at a specific point in space, in this case a point where all three components complete a full wavelength and therefore are in phase at certain points in time. The waves can also align in the space domain. Plotting the waves in the space domain at the moment in time where the waves aligned in Figure E.1 gives a figure like Figure E.2. As seen in this figure, at this specific time instant the waves align perfectly at specific intervals in space too.

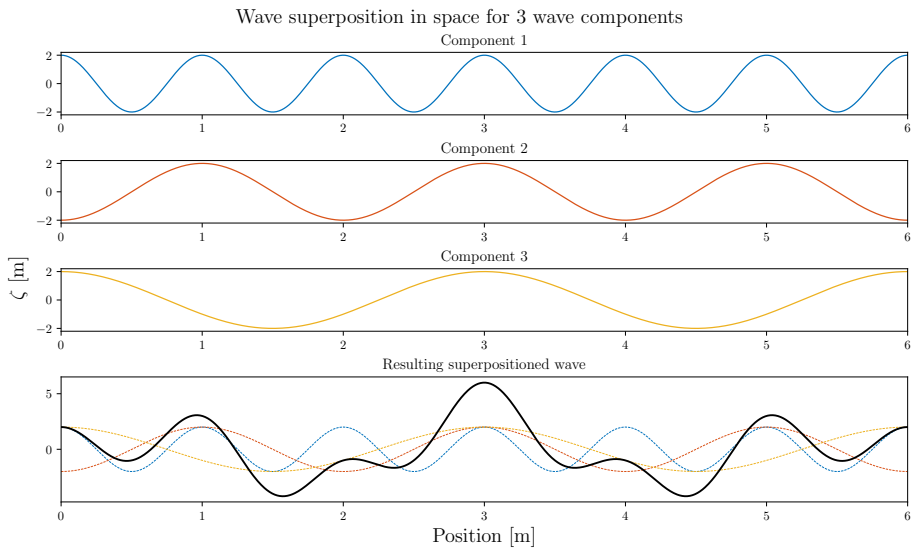

Fig. E.2 *Example of the superposition principle in space domain using three wave components. The bottom graph shows the components and the resulting wave (black) after superposition. It can be seen that the components align at $x = 3$ m for this specific point in time.*

As illustrated above, it is important to make the wave components align in space and time to get the maximum amplitude on the resulting wave. In the experiment the components will be tuned to be in phase in space and time at a specific location, called the focus point. The figures above are for continuous waves which span the full space and time domain. In the experiment the components will be generated using a paddle wave maker. Each component will be generated only for a couple of cycles, and will then start to propagate through the wave tank to the focus point. How the focusing is done in this case is explained next.

The components in the focused wave have different wavelengths. For a linear regular wave the speed (c_p) at which a wave travels is dependent on its wavenumber (k), the water depth (h) and gravitational constant(g). The wavenumber is related to the wavelength through $k = (2\pi)/\lambda$. The wave speed is:

$$c_p = \sqrt{\frac{g}{k} tanh(kh)} \tag{E.1}$$

The components are generated in packets, also known as a wave group. The group speed (c_g) of a wave group is half the velocity of a single component in the wave train, as seen in Equation E.2.

$$c_g = \frac{1}{2} c_p \left(1 + \frac{2kh}{sinh(2kh)}\right) \tag{E.2}$$

As the speed is dependent on the wavelength, the groups containing components with long wavelengths travel faster than the groups containing components with shorter wavelengths. This is a useful property for wave focusing in a wave tank because it can be used to align the wave components in time at the focus point. The group speed is the velocity with which the wave train propagates through a medium after being generated at a certain location. When taking the distance between the focus location and the wavemaker as x_f, the time it takes the wave train to arrive at the focus location is given by Equation E.3.

$$t_f = \frac{x_f}{c_g} \tag{E.3}$$

When two components need to be at the focus point simultaneously, the shorter component should be generated first since this one has a longer travel time. Taking component 1 as the shorter (slower) component and 2 as the longer (faster) component, the required delay for component 2 can be calculated using Equation E.4.

$$t_{delay,2} = t_{f,1} - t_{f,2} = \frac{x_f}{c_{g,1}} - \frac{x_f}{c_{g,2}} \tag{E.4}$$

Using the same method, the delay between the slowest component and all other components can be computed. This wave generation delay is used to make sure that the wave groups of all components arrive at the focus point at the same time. Next, it is explained how to align the wave components at the focus point in the space and time domain. The easiest way to do this is to take the focus location as $x = 0$ m and the focus time as $t = 0$ seconds, and then calculating the phase shift needed at the wave generation point for each component. This will be explained below.

The wave components used in the experiment can be described as linear cosine waves. This means that at $x = 0$ m and $t = 0$ s, the components are always all in phase in space and time. The standard form for these waves is shown in Equation E.5.

$$\zeta(x,t) = A \cdot \cos(kx + \omega t + \theta) \tag{E.5}$$

In this equation A represent the amplitude of the wave component, k is the wavenumber, ω is the angular frequency and θ is a phase shift. The wave number of a wave component is dependent on its wavelength through Equation E.6.

$$k = \frac{2\pi}{\lambda} \tag{E.6}$$

The angular frequency ω is dependent on the wave number through the dispersion relation, as shown in Equation E.7. In this equation h is the water depth.

$$\omega = \sqrt{gktanh(kh)} \tag{E.7}$$

Taking the focus point at $x = 0$ m puts the paddle (wave generation point) at $x = -x_f$. This means that to align the component in space the phase shift at the paddle is equal to $\theta_1 = -kx_f$. Since the wave needs to travel to the focus point, an additional phase shift is needed for the wave component to be in phase in time at the focus point. The second phase shift is caused by the delay in wave generation (due to different travel times), this delay is equal to $\theta_2 = -\omega t_{delay}$. This gives a total phase shift of $\theta = \theta_1 + \theta_2$. The final description for each component at the paddle can thus be described by Equation E.8, in which subscript c denotes the component.

$$\zeta_c(x,t) = A_c \cdot \cos(k_c x + \omega_c t - \omega_c t_{delay} - k_c x_f) \tag{E.8}$$

Figure E.3 gives time traces of a focused wave at various point in the domain. It can be seen that the wave grows in amplitude as it progresses from $x = 0$ m to the focus location (at $x = 5$ m). Additionally, the wave train becomes shorter as the faster waves, which are generated later, are catching up with the slower, earlier generated wavs. According to linear wave theory the wave should have its highest amplitude at the focus location but as seen in the graph the wave continues to grow until $x = 6.8$ m. This is due to non-linear effects not captured by the linear wave theory. The wave breaks just after $x = 6.8$ m when it has become too steep.

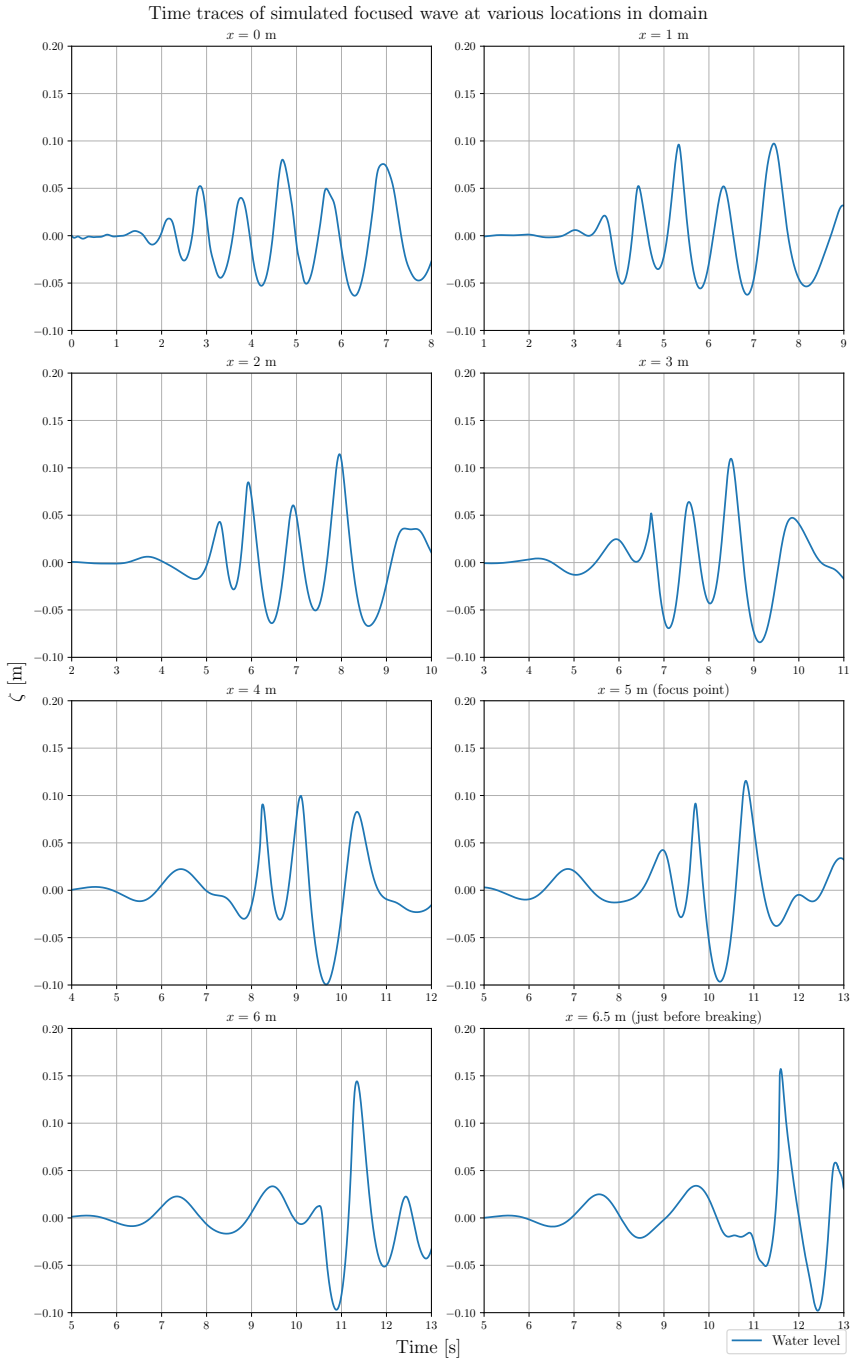

Fig. E.3 *Time trace of resulting wave height at various points in the domain. The focusing of the wave can be seen clearly from the increase in amplitude of the wave and the shortening of the wave train.*